Universidade de Aveiro
Ano 2021

Departamento de Química

Joana Raquel
Mendes Ferreira

Síntese e avaliação biológica de fluoróforos baseados em curcumina

Synthesis and biological evaluation of curcumin-based fluorophores

2021

Universidade de Aveiro **Departamento de Química**
Ano 2021

Joana Raquel Mendes Ferreira

Síntese e avaliação biológica de fluoróforos baseados em curcumina

Synthesis and biological of curcumin-based fluorophores

Dissertação apresentada à Universidade de Aveiro para cumprimento dos requisitos necessários à obtenção do grau de Mestre e realizada sob a orientação científica da Doutora Raquel Nunes da Silva, Investigadora de Pós-Doutoramento, LAQV/REQUIMTE, do Departamento de Química e iBiMED, Instituto de Biomedicina da Universidade de Aveiro, co-orientação da Professora Doutora Maria Ângela Cunha, Professora Auxiliar do Departamento de Biologia da Universidade de Aveiro, e do Doutor Samuel Guieu, Investigador do Departamento de Química da Universidade de Aveiro

o júri

presidente

Prof. Doutor Brian James Goodfellow
Professor Auxiliar do Departamento de Química da Universidade de Aveiro

Doutora Raquel Sofia de Oliveira Nunes da Silva
Investigadora de Pós-Doutoramento, LAQV/REQUIMTE, do Departamento de Química e iBiMED, Instituto de Biomedicina da Universidade de Aveiro

Prof. Doutora Maria Manuel Martinho Sequeira Barata Marques
Professora Auxiliar da Faculdade de Ciências e Tecnologia da Universidade Nova de Lisboa

Agradecimentos

À Raquel, ao Samuel e à professora Ângela pela orientação, ajuda e disponibilidade ao longo desta jornada.

À minha família por me ter proporcionado esta oportunidade e pelo apoio incondicional.

Ao Marcos, o meu porto seguro, aquele que me apoiou incondicionalmente e que esteve sempre do meu lado quando mais precisei.

Aos meus colegas de laboratório pela boa disposição, ajuda e apoio ao longo deste percurso.

Aos meus amigos pela companhia na hora de almoço, na biblioteca e por todos os momentos de descontração. E a todos aqueles que de alguma forma contribuíram para o desenvolvimento desta dissertação.

Thanks are due to the University of Aveiro, FCT/MEC, Centro 2020 and Portugal2020, the COMPETE program, and the European Union (FEDER program) via the financial support to the LAQV-REQUIMTE (UIDB/50006/2020), to the CICECO-Aveiro Institute of Materials (UID/CTM/50011/2019, UIDB/50011/2020, and UIDP/50011/2020) financed by national funds through the FCT/MCTES, to the Instituto de Biomedicina (iBiMED) (UID/BIM/04501/2013; UID/BIM/04501/2019), to the Unidade LiM de microscopia, um nó da Plataforma Portuguesa de Bioimagem (PPBI-POCI-01-0145-FEDER-02212), to the Portuguese NMR Network, and to the PAGE project “Protein aggregation across the lifespan” (CENTRO-01-0145-FEDER-000003).

palavras-chave

Fluorescência; Curcumina; Complexo de Boro; *Fusarium oxysporum*; SH-SY5Y cell line; Marcação celular; Microscopia de Fluorescência

resumo

A curcumina é um composto natural obtido do rizoma de *Curcuma longa*. Esta apresenta diversas propriedades clínicas, como propriedades antitumurais e antimicrobianas, e tem sido sugerida como fotossensibilizador em terapia fotodinâmica como terapia alternativa. Derivados de curcumina têm também sido usados como marcadores fluorescentes de agregados proteicos em doenças neurodegenerativas.

Neste trabalho, uma família de derivados de curcumina foi sintetizada, caracterizada e foram estudadas as suas propriedades fotofísicas. A avaliação biológica destes derivados foi estudada em dois modelos celulares, o fungo fitopatogénico *Fusarium oxysporum* e a linha celular humana SH-SY5Y usada em estudos de doenças neurodegenerativas, recorrendo a testes de citotoxicidade e a microscopia de fluorescência. Os curcuminóides descritos não se mostraram tóxicos no escuro para os modelos celulares em estudo e ainda é sugerida a localização de alguns derivados no interior das células da linha celular SH-SY5Y.

keywords

Fluorescence; fluorophore; curcumin; boron complex; *Fusarium oxysporum*; SH-SY5Y cell line; cell imaging; Fluorescence microscopy

abstract

Curcumin is a natural compound obtained from the rhizome of *Curcuma longa*. It has several properties of clinical interest such as antitumoral and antimicrobial properties and has been suggested as a photosensitizer in photodynamic therapy as an alternative therapy. Curcumin derivatives have also been used as fluorescent markers of protein aggregates in neurodegenerative diseases.

In this work, a family of curcumin derivatives was synthesized, characterized and their photophysical properties were studied. The biological evaluation of these derivatives was studied in two cell models, the phytopathogenic fungus *Fusarium oxysporum* and the human cell line SH-SY5Y used in studies of neurodegenerative diseases, using cytotoxicity tests and fluorescence microscopy. The curcuminoids described were not toxic in the dark to the cell models under study and the location of some derivatives within the cells of the SH-SY5Y cell line is suggested.

Index

List of abbreviations and symbols

λ_{abs} – Maximum absorption wavelength

λ_{emi} – Maximum emission wavelength

σ^* – Excited state

φ_{Δ} – Singlet oxygen quantum yield

φ_f – Emission quantum yield

ACQ – Aggregation-caused quenching

AIE – Aggregation-induced emission

AIEE – Aggregation-induced emission enhancement

DAPI – 4´,6-diamidino-2-phenylindole

EDG – Electron-donating group

EWG – Electron-withdrawing group

HPS – Hexaphenylsilole

HOMO – Highest occupied molecular orbital

IC – Internal conversion

ICT – Intramolecular charge transfer

ISC – Inter-system crossing

LUMO – Lowest unoccupied molecular orbital

MO – Molecular orbital

MW – Microwave

NBD – Nitrobenzoxadiazole

NIR – Near-infrared

NRU – Neutral red uptake

PDA – Potato Dextrose Agar

PDI – Photodynamic inactivation

PDT – Photodynamic therapy

PS – Photosensitizer

RIR – Restriction of intramolecular rotations

ROS – Reactive oxygen species

S_0 – Ground state

S_n – Singlet state

T_n – Triplet state

TPA – Two-photon absorption

TPE – Tetraphenylethylene

List of figures

List of schemes

List of tables

1. CHAPTER I

INTRODUCTION

The knowledge about the subcellular localization and distribution of drugs is an important step in disease diagnosis and treatment. Depending on their structure, drugs will be distributed in different locations in the cell, like organelles or plasmatic membranes, and it is essential to understand which type of structural differences will influence their localization and distribution, leading to a better or worse pharmacological efficiency.

In this work, we will study the toxicity and localization of several curcumin derivatives in two different eukaryotic cell models to understand their preferential localization and distribution for a potential tool to treat several diseases. Curcumin has aroused interest in the scientific research community due to several clinical properties. The organisms that will be approached are the fungus *Fusarium oxysporum*, which is responsible for huge crop losses in the field of agriculture, and the cell line SH usually used in the screening of new drugs.

1.1. Basic concepts of photophysics

1.1.1. Luminescence

In 1888, Eilhardt Wiedemann adopted the term luminescence (from Latin *lumen*, which means light) to describe all the phenomena related to light that do not have the interference of temperature.[1] In this way, luminescence is described as the spontaneous emission of light by a substance from excited electronic states[2] and it is divided into several types depending on the excitation mode of the substance. These include photoluminescence (excitation by photon absorption), sonoluminescence (excitation by ultrasound), chemiluminescence (excitation by a chemical reaction) as some examples.[1] In the present work, only photoluminescence will be approached. This kind of luminescence is characterized by the absorption of light with a certain wavelength by a molecule and, then, light emission, which is recorded at another wavelength. In most cases, the emission wavelength is longer than the absorption wavelength.[3] In photoluminescence, the excitation could be driven by the absorption of one photon or by the simultaneous absorption of two or more photons, and the latter process is also known as multiphoton excitation.[4,5] This process will be briefly described later.

Luminescence is divided into two categories: fluorescence and phosphorescence. Fluorescence is defined as the emission of light from an excited state where the spin multiplicity of electrons is maintained while phosphorescence is also characterized by the emission of light from an excited state but, in contrast to fluorescence, this phenomenon is characterized by a spin inversion.[2] These two phenomena will be discussed in detail in the further sections.

1.1.2. Mechanisms of luminescence and Perrin-Jablonski diagram

To better understand both luminescence forms, in 1935 a polish physician, Aleksander Jablonski, with the important contribution of french physicians Jean and Francis Perrin, designed a diagram that describes the electronic transitions that occur in fluorescence and phosphorescence phenomena.[6] An adaptation of this diagram is represented in figure 1.

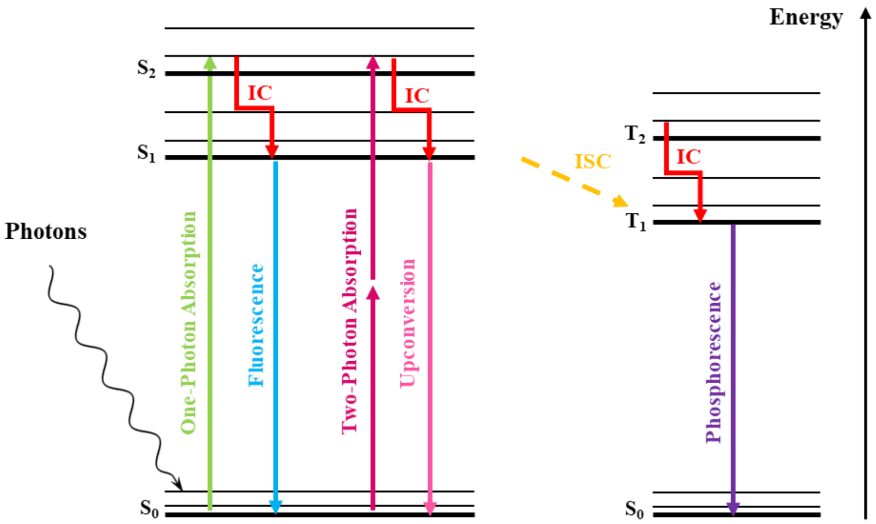

Figure 1: Perrin-Jablonski diagram.

In the Perrin-Jablonski diagram, the radiative and non-radiative transitions between the excited energy levels and the ground state are represented. Upon photon absorption, a molecule rises its energy from the ground state (usually a singlet state, S_0) to an excited state. In an allowed transition, both states should have the same spin multiplicity and transitions between states with different spin multiplicity are forbidden.[1] In other words, being S_0 a singlet state the excited state also should be a singlet state (S_n, n=1, 2, …).[3] In this case, when the molecule returns to the ground state, the molecule emits light in the form of fluorescence and the excited state has a short lifetime inferior to 10^{-6} seconds.[3] Even if the most favorable electronic transition is between two states with the same multiplicity, in some cases, the excited electron inverts its spin and the molecule passes from a singlet state to a triplet state (T_n), this non-emissive process is called inter-system crossing (ISC). Thus, the emission when a molecule in an excited state T_n returns to the ground state is in the form of phosphorescence with a long-lived excited state lifetime between 10^{-6} seconds and several seconds.[3] Despite this transition being forbidden, in some cases, it is possible due to spin-orbit coupling which increases the probability of occurrence of these types of transitions. Spin-orbit coupling is common in molecules where heavy atoms, such as bromine and iodine, and metallic atoms[7] are present, which means that the rate of phosphorescence in these types of molecules is higher.[4]

The two-photon absorption (TPA) is also described in the Perrin-Jablonski diagram. The TPA phenomenon is characterized by the fluorophore excitation to the higher energy states (S_n) by absorption of photons with longer wavelengths and consequently with lower energy.[8] As the energy needed to achieve excited states is the same for one-photon absorption and TPA, with longer wavelengths it is necessary more photons to absorb the same amount of energy.[4] In this case, two photons are simultaneously absorbed to rises the fluorophore to an excited state. The excitation wavelengths in TPA are in the range 720 nm to 950 nm[4] which is in the near-infrared (NIR) region. The use of NIR light presents some advantages when working with biological samples because these longer wavelengths allow deeper penetration and reduced absorption by biological tissues.[9] A limitation of TPA is that the two photons should hit the molecule simultaneously, in which a large number of photons are required, and they should be in phase which only is possible using a laser source. As in one-photon absorption, when a molecule absorbs energy by a two-photon phenomenon it will return to the ground state accompanied by a photon emission in a process called Upconversion. This process is characterized by the release of energy with a smaller wavelength than the energy absorbed, contrary to what happens in the one-photon absorption phenomenon.[8]

Beyond radiative transitions, the Perrin-Jablonski diagram also depicts non-radiative transitions such as internal conversions (IC) and vibrational relaxations. When the energy absorbed by the molecule is higher than the necessary energy to excite the molecule to S_1, it goes to a higher excited state, such as S_2. In this case, the molecule rapidly passes to the lowest-energy excited state S_1 in a non-emissive transition called internal conversion.[3] Another non-radiative process is a vibrational relaxation characterized by the transition between the higher vibrational states and the lowest level of the excited state. Lastly, when a molecule does not lose energy by luminescence, it loses it by the release of thermal energy.[3]

The fluorescence efficiency of a given molecule could be described by the emission quantum yield (φ_f), which is defined as the ratio between the number of emitted and absorbed photons, and is characteristic of each molecule in a particular environment. According to Kasha–Vavilov rule, the emission quantum yield is independent of the excitation wavelength.[10] Emission quantum yield could be calculated through the following equation (Eq. 1),[11] where **F** is the integrated intensities of emission spectra (area), **f** is the absorption factor, in other words, the fraction of the incident light absorbed by the molecule, **n** is the refraction index of the solution, **s** stands for standard and **i** for the intended compound (sample):

$$\varphi_f^{i} = \frac{F^{i} f_s {n_i}^2}{F^{s} f_i {n_s}^2} \times \varphi_f^{s} \qquad \text{(Eq. 1)}$$

An important characteristic of some fluorophores is the ability to interact with molecular oxygen and form reactive oxygen species (ROS) like singlet oxygen when exposed to light: these fluorophores are named photosensitizers (PS). This plays a central role in photodynamic therapy (PDT), which is a widely used non-invasive approach to the treatment of cancer and bacterial, fungal or viral infections and, in the case of infections and sterilization of medical surfaces and instruments, also denominated photodynamic inactivation (PDI). PDT conjugates three essential components: photosensitizer, light, and molecular oxygen. Figure 2[12,13] represents an adaptation of the Perrin-Jablonski diagram that explains photodynamic therapy mechanisms.

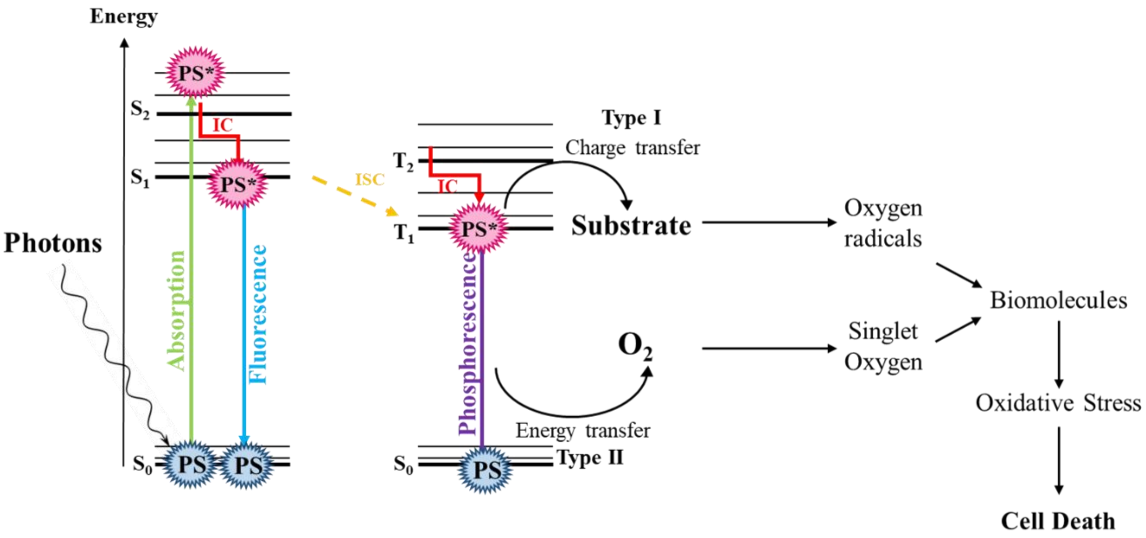

Figure 2: Perrin-Jablonski diagram adaptation to photodynamic therapy.

As demonstrated in figure 2, PDT can undergo two different types of reactions, type I and II. Type I reactions involve a charge transfer from the excited PS to a substrate with consequent formation of oxygen radicals. In a type I mechanism the photosensitizer in a triplet state undergoes a primary reaction with a target biomolecule in its vicinity, leading to a hydrogen atom abstraction or an electron transfer process that results in the formation of a radical.[12,14,15] This radical will react with molecular oxygen to produce multiple oxidized products, usually called reactive oxygen species (ROS), such as superoxide, hydroperoxyl and hydroxyl radicals, and hydrogen peroxide.[15] In contrast to type I reactions, in type II reactions instead of occurring a charge transfer to molecular oxygen it occurs an energy transfer leading to singlet oxygen ($^1O_2$).[12,14,15] The energy that is transferred to oxygen comes from the electronic transition of PS from the excited triplet state to the ground state, regenerating the PS. In both reaction mechanisms, ROS and singlet oxygen will react with the biomolecules, like proteins or lipids, and also organelles in the vicinity inducing oxidative stress and subsequently cell death.

Over the years, several photosensitizers have been studied and they could be divided accordingly to their structure and origin into tetrapyrrole structures, synthetic dyes, and natural products (figure 3).[16] These include porphyrin, phthalocyanine, curcumin, BODIPY derivatives, and so on.

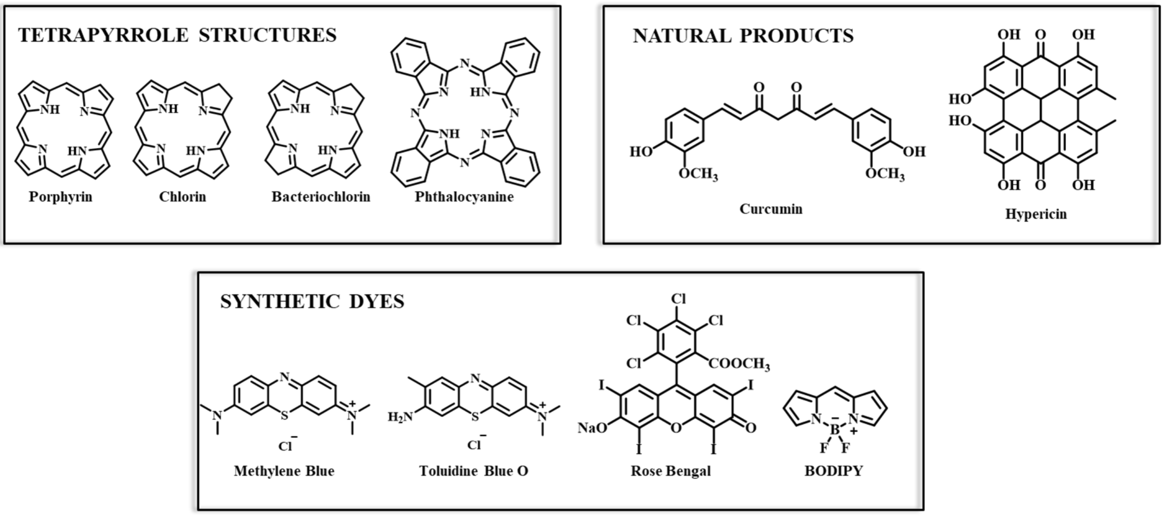

Figure 3: Examples of photosensitizers used in photodynamic therapy.

1.1.3. Energy absorption and emission

Two important photophysical characteristics of molecules in fluorescence are the emission and absorption spectra, which depict where are represented the maximum emission (λ_{emi}) and absorption (λ_{abs}) wavelengths. These two spectra are specific of each molecule and are important to determine at which wavelength the molecule absorbs and emits better. According to George Stokes, an Irish physician and mathematician, the emission wavelength is normally longer than the absorption wavelength, and this difference is denominated Stokes shift.[1]

Molecules have their electrons distributed in molecular orbitals and when one molecule is subjected to a light source it absorbs energy, which promotes one electron to a molecular orbital (MO) of higher energy. Depending on the bond type between the atoms, transitions occur with a different amount of energy absorbed. For example, electrons in a σ bond require higher energy absorption to transit to an excited state (σ^*) than those in a π bond. There are two important molecular orbitals in electronic transitions: the highest occupied molecular orbital (HOMO) and lowest unoccupied molecular orbital (LUMO). For instance, in an electronic transition such as $\pi \rightarrow \pi^*$ the electrons pass from the HOMO to the LUMO. The energy gap between HOMO and LUMO is strongly correlated with π electron conjugation within the molecule, and with higher conjugation smaller will be the energy gap between these two orbitals. In that way, if lower energy is required to promote $\pi \rightarrow \pi^*$ transition the maximum emission and absorption wavelengths are longer. The same effect happens when a heteroatom, like oxygen and nitrogen, is introduced in the π system increasing conjugation, thus inducing a bathochromic shift in the emission and absorption spectra.[1] Aromatic compounds are characterized for being highly conjugated system hence most of the fluorescent compounds are aromatic.

In some compounds, absorption and emission spectra present the characteristic of varying when in solvents with different polarities.[17,18] This characteristic is denominated solvatochromism and is described as the marked change in the absorption band of a certain dye due to a change in solvent polarity where this is dissolved.[19] These differences could be attributed to compounds due to their structural characteristics, being charge transfer properties, such as in push-pull fluorophores, an example.[20] Solvatochromism is classified into negative solvatochromism and positive solvatochromism depending on the kind of shift that is promoted. A negative solvatochromism is related to a hypsochromic shift, also known as blue shift, while a positive solvatochromism is related to a bathochromic shift, also known as red shift.[19] Several dyes have already been described with solvatochromic properties like curcumin derivatives,[21] fluorene derivatives,[22] and many others.[18,23]

1.1.4. Structural effects on fluorescence emission

As seen in the last section, the fluorescence emission wavelength could be modified when the molecular structure is changed in order to promote a change in the energy gap HOMO-LUMO. In this way, fluorescence wavelength could be increased or decreased when some groups that increase or decrease the electron density in the conjugated system are introduced. This is the auxochromic effect and it is promoted by groups such as –OH, –NH_2 or –COOH.

π conjugation is one of the most important parameters when absorption and fluorescence emission wavelengths is concerned. Groups such as –OH, –OR, –NH_2, –NHR, –NR_2 are groups that increase the conjugation of π electrons and activate this system giving to it a lone pair of electrons that will promote a delocalization of the electrons in the aromatic ring. This electronic delocalization induces a shift in the emission and absorption wavelengths.[1,24,25] This type of substituents, that promote an electronic delocalization for giving a lone pair of electrons, could be described as electron-donating groups (EDG). In contrast to EDG, there are some substituents that instead of activating the π-system, deactivate it by decreasing the π conjugation in the system. This deactivation is promoted by nitro and carbonyl groups, considered electron-withdrawing groups (EWG), and is due to the localization of the π electrons. The effect of EWG on compounds is also, like the EDG effect, a shift in the emission and absorption wavelengths. These effects involving a redistribution of electrons in the molecule promoted by EDG and EWG are described as intramolecular charge transfer (ICT).[1,24,25]

Another structural change that promotes a shift in the emission wavelength of a given compound is the presence of a heavy atom like bromine or iodine. The presence of this kind of atoms facilitates ISC due to spin-orbit coupling, promoting phosphorescence instead of fluorescence.[4] In that way, the fluorescence will be quenched and the fluorescence emission quantum yield will be lower.[1]

1.1.5. Fluorescence in solution and in aggregates: ACQ and AIE(E) phenomena

Fluorescence is a characteristic of each fluorophore as well as the intensity of fluorescence. As mentioned before, this intensity is defined by the emission quantum yield and depends on the compound structure, the solvent, and the phase (in solution, amorphous solid, crystalline solid). This fluorescence intensity could be increased or decreased due to several factors and the most important, in addition to structure, are pH, concentration, the stability of the compound in light, and temperature.[26] When the solubility of a fluorophore decreases in the solution, it tends to aggregate, and the aggregates formed can be amorphous, or crystalline.

As the main fluorescent compounds are aromatic and, in this way, have a highly conjugated π system and a planar structure, when they are in a concentrated solution or in the aggregate state they are usually linked by $\pi - \pi$ stacking interactions that promote a quenching of the fluorescence, regardless of the fluorophores being strongly fluorescent in solution. This phenomenon is called aggregation-caused quenching (ACQ).[27] This effect constitutes a limitation when ACQ-compounds are used in biologic systems due to their reduced solubility and, consequently, high aggregation. In that way, their fluorescence will decrease, which makes it harder to locate them in the biological system.

In contrast to ACQ, there are some compounds that, when in a concentrated solution or in the aggregate state, increase their fluorescence intensity instead of decrease. This phenomenon was discovered by Ben Zhong Tang and his co-workers in 2001.[28] During their work, they observed that when a drop of a 1-methyl-1,2,3,4,5-pentaphenylsilole solution was added to a TLC plate the spot that still had solvent was not luminescent under the ultraviolet light and when the spot dried, it started to be luminescent under the UV light. This phenomenon was described as aggregation-induced emission (AIE).[28] A variation of AIE is aggregation-induced emission enhancement (AIEE), that is characterized by compounds that are poorly emissive in the solution state and when in aggregates have an enhancement of their fluorescence intensity.[27] In the recent years, several AIE-compounds have been described in order to have a broad spectrum of AIE luminogens that could be used in biological systems and some examples are shown in figure 4. AIE luminogens could be divided into several groups according to their structure: hydrocarbon luminogens (figure 4b), heteroatom-containing luminogens (figure 4c), luminogens with hydrogen bonds (figure 4d), polymeric luminogens (figure 4e), among others. In the case of polymeric luminogens (figure 4e), the monomer is a hydrocarbon luminogen tetraphenylethylene (TPE) that exhibits AIE properties. The proposed mechanism to explain AIE is the restriction of intramolecular rotations (RIR).[29] This mechanism is based on the principle that in solution the luminogen presents some groups that exhibit rotation and upon aggregation these rotations are blocked and/or restricted.[27] The difference between both states is that in solution the energy of the excited state is dissipated in a non-radiative way while upon rotation restriction this type of decay is hindered and a radiative decay is promoted.[29] These AIE luminogens, like TPE,[30,31] have been used extensively as probes for sensing applications such as fluorescence imaging.[32]

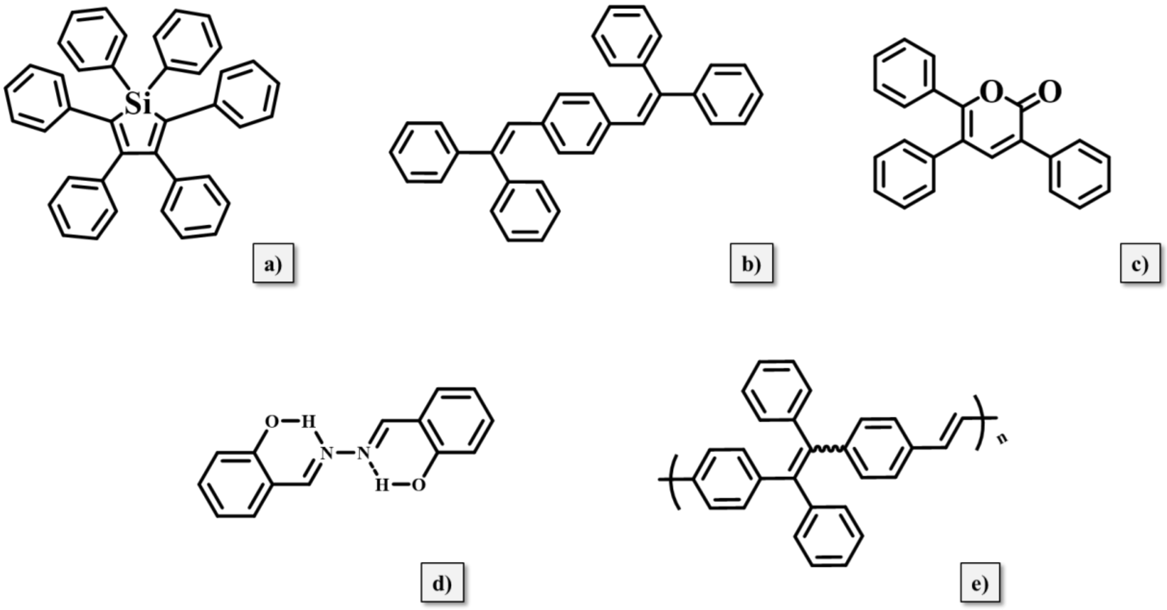

Figure 4: Some examples of compounds that exhibit AIE behavior: a) Hexaphenylsilole (HPS);[33] b) 1,4-di- [(E)-2-phenyl-1-propenyl]benzene;[34] c) 3,5,6-triphenyl-*2H*-pyran-2-one;[35] d) Hydroxylated derivative of *N*,*N*'-disalicylaldazine;[36] e) polymer of TPE monomers.[27]

Aggregates could also be considered H-aggregates or Scheibe-aggregates (J-aggregates). J- and H-aggregates are when there is a strong dipolar interaction between the fluorophores, creating a new species. Figure 5 describes the mechanisms behind the aggregation phenomenon. Depending on the conformation and the angle θ between the dipolar moments of the monomer units[37] the aggregates could be classified into J-aggregates and H-aggregates. If $\theta < 54.7^{o}$ J-aggregates are formed in a head-to-tail conformation, while if $\theta > 54.7^{o}$ H-aggregates are formed in a parallel/sandwich conformation.[37,38] The differences in the conformation of the aggregates promotes differences in the absorption and emission spectra of the dimers formed comparing with the monomer. According to Kasha's exciton model, when a dimer is formed there is a split of the excited state S_1 in two different states.[39] In H-aggregates, when energy is absorbed, only transitions to the higher energy exciton state are allowed being necessary a bigger amount of energy.[39] To return to the ground state, the dimer can emit a photon, but will more probably transit to the first exciton by internal conversion, from where radiative decay to the ground state is forbidden: therefore, both absorption and emission will be blue-shifted compared to the monomer, and the emission intensity will decrease.[37,38] In contrast to H-aggregates, in J-aggregates the only transition allowed is to the lower energy exciton promoting absorption and emission at longer wavelengths, and an increase of the fluorescence quantum yield. While H-aggregates promotes a hypsochromic shift, J-aggregates promotes a bathochromic shift between the absorption spectra of the aggregate relative to the monomer.[40] When there is no particular interaction (just Van der Waals), they are just aggregates: in this case, there is no shift in the wavelengths of absorption and emission, and AIEE can be observed.

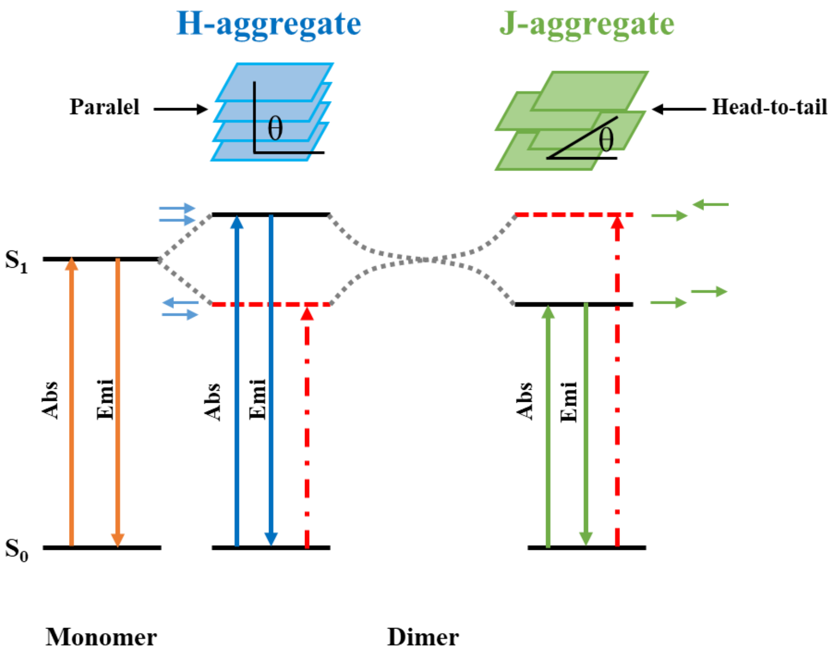

Figure 5: Exciton energy diagram for H- and J-aggregates.

An emerging application for PDT is fluorescence imaging-guided photodynamic therapy where the photosensitizer could be localized using fluorescence microscopy. This is possible due to the PS ability to emit light through fluorescence when subjected to a specific wavelength. Fluorescence imaging-guided is a powerful technique that allows the optimization of PDT with the identification of the preferential accumulation of PS in the biological system and therefore the synthesis could be driven to allow PS accumulation in the desired target in cells. However, some fluorescent PSs aggregate when in biological systems and, as previously mentioned, lose their fluorescence and their ability to form singlet oxygen. To solve this problem, PSs with AIE(E) properties are very useful. These should be able to maintain their ability to form singlet oxygen and their fluorescence to allow identification when in the aggregate state. This could be achieved by joining an effective PS to a molecule that exhibits AIE(E) property.

Recently, some studies have been made to join aggregation-induced emission with photodynamic therapy imaging, but the research in this field is still scarce and there is a need for further investigations.[31,41,42]

1.2. Cellular imaging

Cellular imaging is a powerful technique in the field of biological and biomedical sciences. This technique is based on the principle that organelles, subcellular structures, or biomolecules are stained with a certain dye or molecular probe to allow its visualization using fluorescence microscopy. Ideally, the fluorescent probe will selectively accumulate in a certain organelle or subcellular structure, or bind to a specific biomolecule without causing any change in cell function or structure (figure 6). Therefore, fluorescence imaging provides new knowledge about the cellular mechanisms which is useful in the diagnostic and treatment of diseases, and the development of new drugs based on the structure-affinity of fluorescent probes for organelles, subcellular structures, and biomolecules.

Eukaryotic organisms possess organelles like the nucleus, mitochondria, lysosomes, endoplasmic reticulum, and Golgi apparatus that play an important role in cell viability and maintenance. In contrast with animal cells, fungi possess a cell wall beside a plasma membrane. The design of probes capable to target the different organelles and biomolecules present in the fungal cell is an important step to understand the underlying mechanisms of infection in plant hosts and resistance to actual drugs and fungicides. Taking advantage of the current knowledge on the physicochemical properties of organelles, new fluorescent probes could be designed to target specifically certain organelle. However, some properties should be present in newly designed probes to be suitable for use in biological imaging like low cytotoxicity, high photostability,[43] and NIR emission is preferred to allow a deeper penetration in tissues, a minimal absorption and emission of biological samples, and a reduced scattering.[44]

From the moment that the new probes could localize in the desired organelle, new treatments could be developed to use them to cause severe and irreversible damages in cell structures leading to cell death or a particular inhibition or activation of a cellular process.

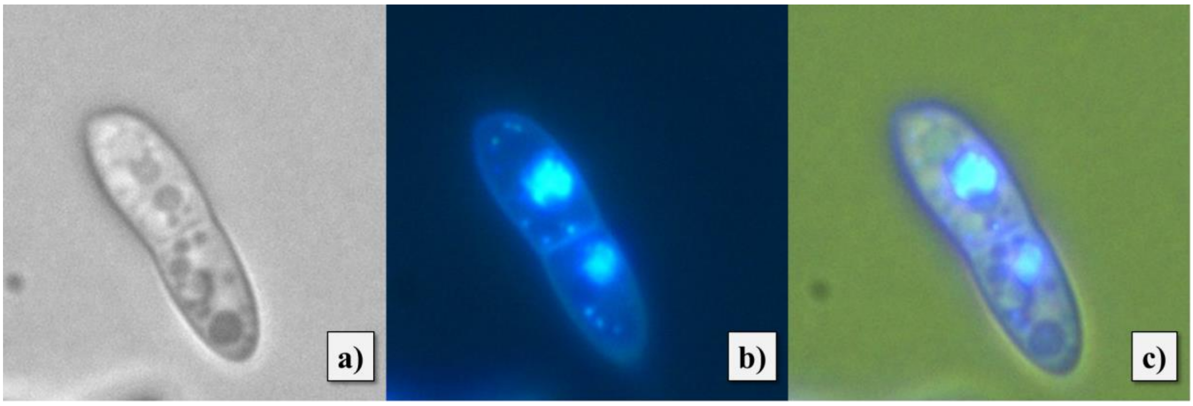

Figure 6: *Fusarium oxysporum* microconidia fluorescence imaging. a) Brightfield imaging of microconidia stained with DAPI, b) Fluorescence imaging (blue channel) of microconidia stained with DAPI, c) merged image using software Fiji ImageJ.

1.2.1. Types of cell imaging

Cell observation under fluorescence microscopy allows the understanding of cellular structures and mechanisms and, depending on the kind of research, it could be performed using live or fixed cells, which require different treatments. The main differences between live-cell imaging and fixed cell imaging will be presented.

1.2.1.1. Live-cell imaging

Live-cell imaging is a widely used technique that uses live cells allowing more dynamic imaging than using dead/fixed cells. Live-cell enables recording the cells in a timelapse which is useful to track cellular mechanisms.[45] Probes used in live-cell should be non-toxic to do not promote any damage in cells, and they are known as vital dyes.[46]

1.2.1.2. Fixed cell imaging

A contrast against live-cell imaging is fixed-cell imaging where cells are firstly fixed in a specific time-point with some chemical fixative before microscopy visualization. In this technique, the main objective is to keep the cell structure in dead cells.[47] Herein cells are preserved in a certain cellular stage, where the cell shape and content are maintained.

Sample preparation

Sample preparation for fluorescence microscopy could be divided in three fundamentals steps: fixation (in case of fixed cells), permeabilization (if needed), and cell labeling. Sometimes the cell labeling is made before the fixative step.

Fixatives used in sample preparation belong to two categories: organic solvents and aldehyde reagents. The organic solvents normally used as fixatives are alcohols (methanol and ethanol, for example) and acetone. Organic solvents are used to dehydrate the tissues, remove lipids and denature proteins.[47] In the case of aldehyde reagents, formaldehyde and glutaraldehyde are used, being formaldehyde the most used even though it is carcinogenic.[48] Aldehyde reagents are known for cross-linking between biomolecules, like proteins and nucleic acids, by promoting intermolecular bridges between the free amine groups.[47] Formaldehyde fixative is usually in a 4% solution.[47]

In some cases, after fixation, the cell is subjected to a permeabilization step with detergents, as Triton X-100 or Tween 20, or with organic solvents, as methanol or acetone. Permeabilization removes cell membrane lipids to allow permeabilization of other molecules as dyes probes or even antibodies in immunohistochemistry.[49] After permeabilization the cells should be washed with a phosphate saline buffer.[49]

The last step in sample preparation is the labeling with the desired probe and incubation to allow probes to enter cells. After incubation cells should be washed with a phosphate saline buffer to remove the dye in excess.

Another method to prepare cells from fungal cell cultures, for example, is using the inverted agar block method.[50] This method is based on cutting a section from the agar culture and placing it in a slide in a drop of a liquid medium, as PBS with a probe if intended, and incubated. Before the microscopy visualization, the agar plug should be washed with PBS and then placed in a slide upon a coverslip. The inverted agar block method is widely used in fungal live-cell imaging.[50] In live-cell imaging, issues such as temperature must be taken into account and the environment should be maintained at the optimal temperatures for the type of cells used.

1.2.2. Probes

Cell imaging probes are a powerful tool concerning staining cellular structures and have gained some interest over the years. Several probes have already been described to label specific structures, organelles, or certain environments inside the cell. In the following sections, will be discussed the most used probes in cell imaging and what kind of structures they stain. Figure 7 and 8 represents the chemical structures of some probes addressed in the further sections.

Cell membrane imaging probes

Cell membranes, characterized by a phospholipid bilayer, besides being the barrier between the extracellular and intracellular media, are also present in organelles. When it comes to stain cell membranes the dyes should have affinity to a hydrophobic environment due to the high amount of lipids present. Octadecyl Rhodamine B (Figure 7 – 18: an example of a rhodamine) is used to stain the plasma membrane[46] which binds it on the hydrophilic medium maintaining the alkyl group in the hydrophobic medium. FM4-64 (Figure 8) and FM1-43 (Figure 8), amphiphilic styryl dyes, are also membrane-staining dyes and increase their fluorescence when located in a hydrophobic environment.[50]

Mitochondria imaging probes

The major group of fluorescent dyes used to label mitochondria is based on its negative membrane potential and some of the commercially available are known as the MitoTracker dyes which include the, Mitotracker Red, MitoTracker Orange, and MitoTracker Deep Red.[51]

Based on the negative membrane potential, some cationic fluorescent dyes have been designed to amplify the probe range like delocalized lipophilic cations, for example, triphenylphosphonium (TPP) (Figure 8), quinoline and pyridine derivatives, cyanine, rhodamine, and DASPMI.[50,52]

FM-dyes (FM4-64 and FM1-43) are also known for staining mitochondria.[50]

Nucleus imaging probes

In a eukaryotic cell, the nucleus is responsible for the storage of cell DNA and also for the regulation of gene expression.[43] Therefore, the nucleus probe design is mainly focused on DNA staining. These dyes are characterized by being positively charged and by binding in the minor groove of the double-strand DNA which is negatively charged.[52] The most common dyes currently used to stain DNA are the blue fluorescent dyes DAPI (4′,6-

diamidino-2-phenylindole) (Figure 7 – 12) and Hoechst dyes (Figure 7 – 13).[46,50,53] However, although both dyes are used in live-cell and fixed staining, Hoechst dyes are preferred over DAPI by being more cell-permeable,[46] in other words, in live cells they cross the nuclear membrane more easily than DAPI.[54]

Dyes as ethidium bromide, acridine orange, Syto dyes (Syto 11, 13, 14, 15 and 16), and also $DIOC_6(3)$ are also able to stain the nucleus.[50,53]

Cell wall imaging probes

Eukaryotic cells of fungi have a structural difference concerning animal cells by presenting a rigid cell wall outside the cell membrane. This cell wall is mainly composed of chitin, glucans, and glycoproteins.[55] A widely used dye to stain cell walls is Calcofluor White M2R (Figure 8) due to its ability to bind to β-1,3-polysaccharides and β-1,4-polysaccharides present in chitin.[56] Calcofluor White should be excited around 347 nm and the structure will appear with a green to blue color.[56]

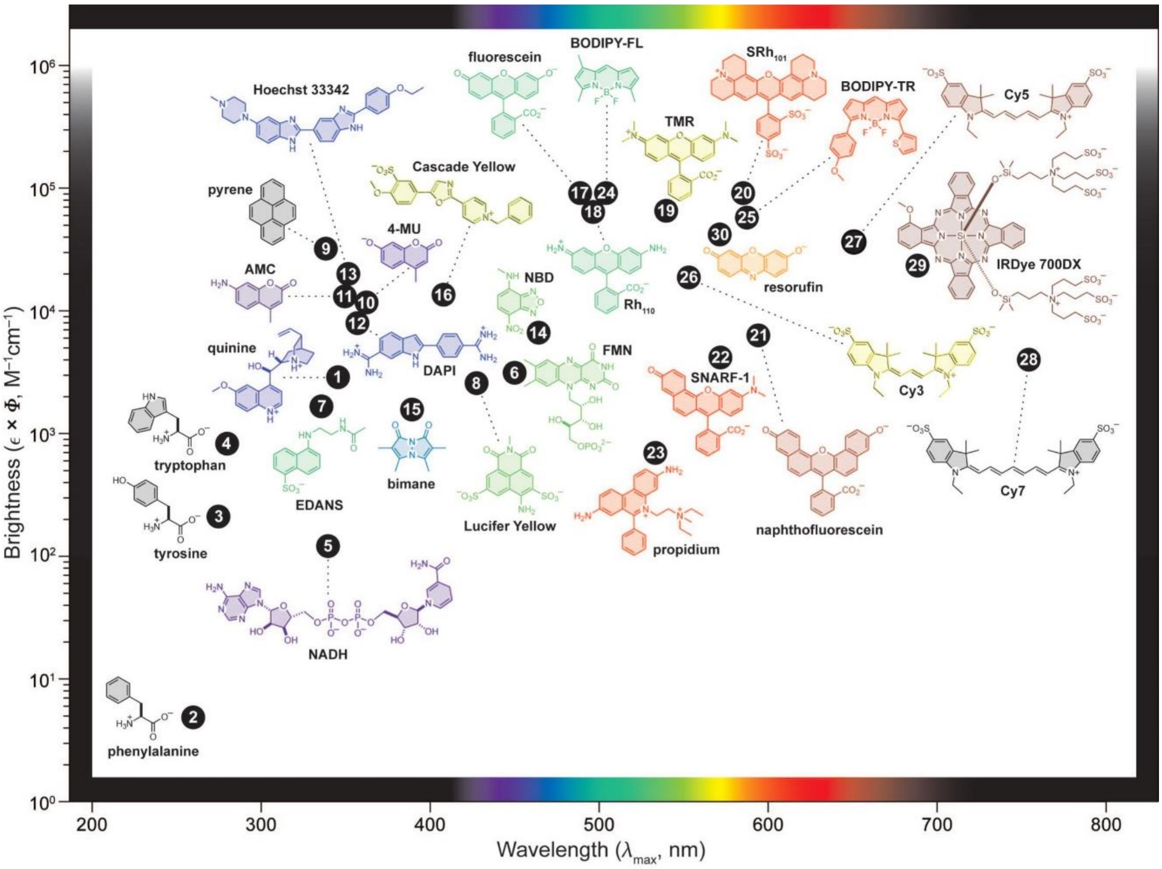

Figure 7: Structure, maximum absorption wavelength and brightness of the major class of fluorophores.[57] Reprinted with permission from Lavis, L. D. & Raines, R. T. Bright Ideas for Chemical Biology. ACS Chem. Biol. 3, 142–155 (2008). Copyright 2021 American Chemical Society

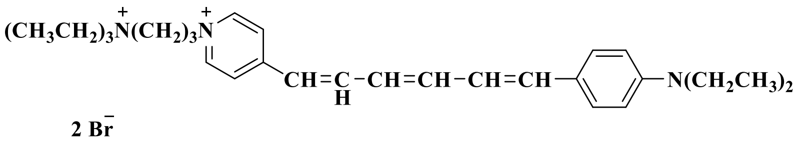

FM4-64

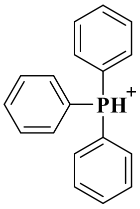

TPP

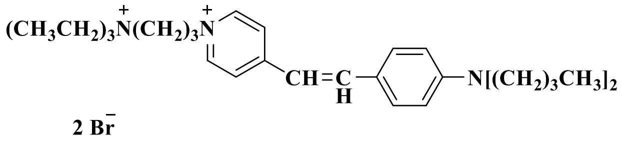

FM1-43

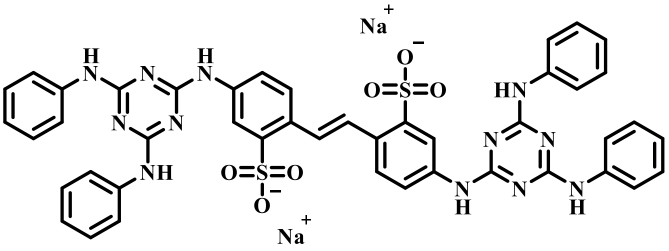

Calcofluor White M2R

Figure 8: Structure of some probes used in cellular imaging. TPP – Triphenylphosphonium.

1.3. Curcumin as a fluorescent probe

1.3.1. Chemical, photophysical and biological properties

Curcumin is a spice with a yellow color found on the rizhome of *Curcuma longa* (turmeric). Curcumin is a polyphenolic molecule and also the primary active compound found in turmeric. Its structure is characterized by two aromatic rings with methoxy and hydroxy groups on *meta* and *para* positions, respectively, linked to a β-diketone through a double bond promoting a symmetric character to the molecule (figure 9). Due to the presence of β-diketone in its structure, curcumin can be found in two tautomeric conformations, keto and enol, derived from the intramolecular hydrogen atom transfer. These tautomeric conformations depend on temperature, solvent polarity, and the substituents of the aromatic rings. Curcumin's hydrophobicity promotes poor solubility in water and good solubility in organic solvents.[58]

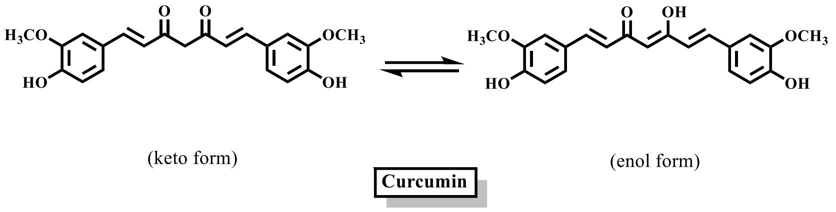

Figure 9: Structure of curcumin extracted from *Curcuma longa.*

When in solution, the structural properties of curcumin promote a strong absorption band in the visible region of the spectra, in the range of 408 to 434 nm, which is due to the electronic transitions $\pi \rightarrow \pi^*$ upon light absorption.[59] Concerning fluorescence emission from curcumin and also from its derivatives, these are strongly dependent on the solvent polarity.[17,21,60] Beyond differences in emission wavelength, differences in emission quantum yield are also seen. Taking into account these differences, the fluorescence emission wavelength of curcumin is between 460 and 550 nm.[61] Some curcumin analogs have been demonstrated two-photon absorption and emission near-infrared spectral region.[62] Curcumin also shows some phosphorescence in the range of 600 to 800 nm and demonstrates some ability to generate $^1O_2$, which makes curcumin a potential photosensitizer.[63]

Beyond the chemical and photophysical properties, curcumin exhibits interesting applications in medicine being considered a molecule with antitumoral,[64] antimicrobial,[65] anti-inflammatory,[66] anti-oxidant properties,[67] among others. After oral administration, curcumin is metabolized by the organism, mainly in the liver.[68] Curcumin metabolites are described in figure 10. Curcumin glucuronide and curcumin sulfate are obtained by an O-conjugation reaction, while the tetra-, hexa- and octa-hydrocurcumin result from a bioreduction.[68,69] Curcumin metabolites have been shown to have biological activites as anti-inflammatory and anti-oxidant.[68] Fungal metabolization of curcumin in *Rhizopus chinensis* has already been described but research in the fungal metabolization of curcumin is still scarce.[70]

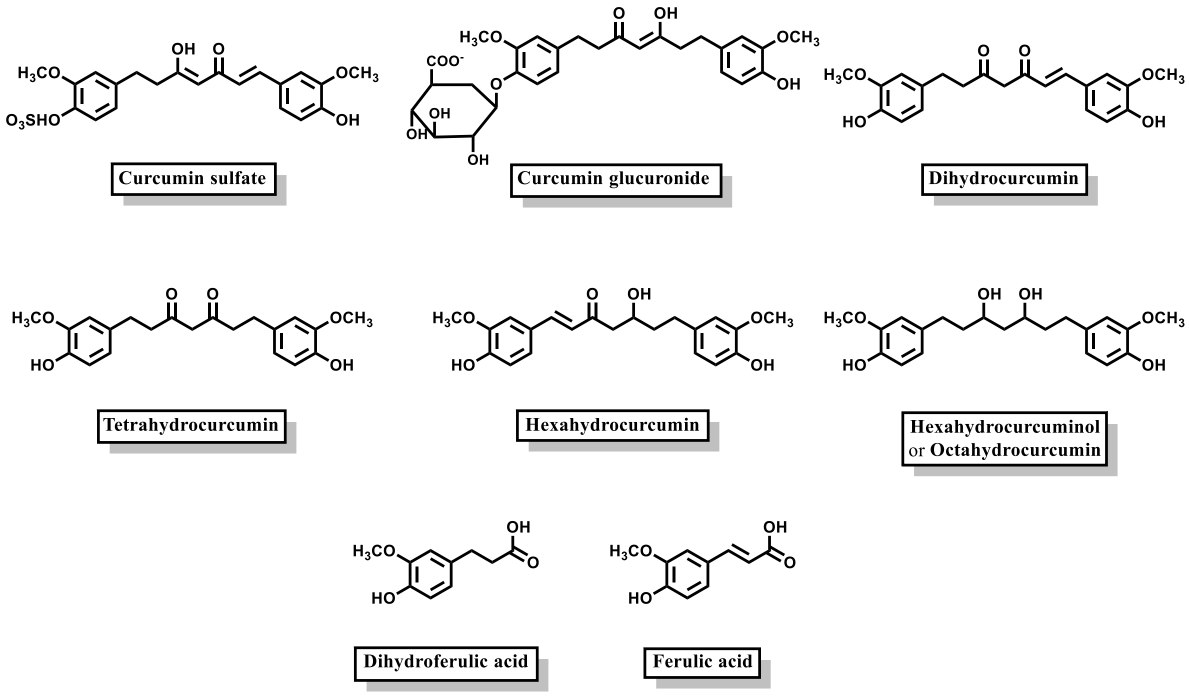

Figure 10: Curcumin metabolites.

Curcumin derivatives have also been studied as potential tools in the diagnosis and treatment of some neurodegenerative diseases such as Parkinson's and Alzheimer's.[71] Some of the molecular targets of curcumin include inflammatory molecules,[72] enzymes,[73] growth factors,[74] transcription factors,[66] and others that exhibit an important role in invasive cell/ tumor integrity, proliferation, and self-defense.

1.3.2. Fluorescence imaging

Curcumin has been associated with several pharmacological properties and also in the detection of Aβ aggregates and reduction of oxidative damages in neurodegenerative diseases.[75,76] Since it has been shown that curcumin accumulates in the senile plaques,[76] several derivatives have been synthesized to improve the curcumin spectroscopic properties keeping the ability to localize into Aβ aggregates, and a new series of compounds with near-infrared fluorescence has been described which includes the CRANAD derivatives (figure 11).[77–79]

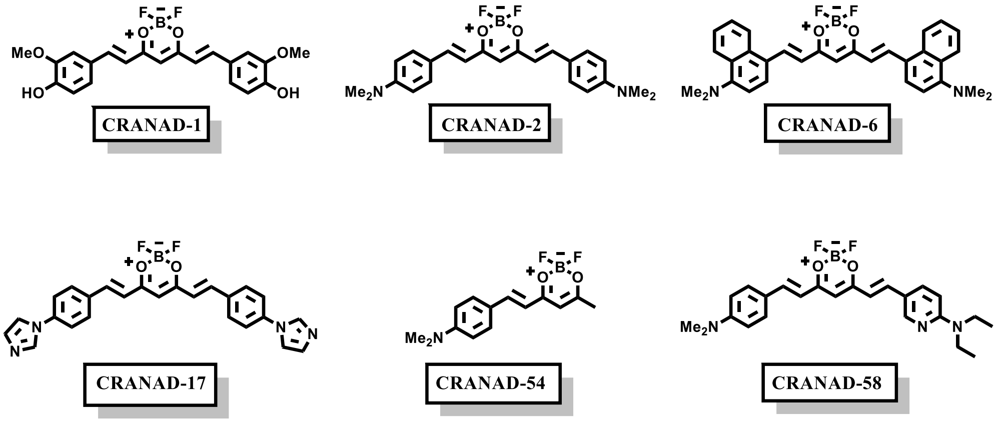

Figure 11: Examples of some curcumin-derivated fluorescent probes CRANAD.

1.3.3. Synthesis: an overview

Curcumin was isolated from *Curcuma longa* for the first time in 1815, but the first report about its synthesis only appear after one century in 1918 by Lampe. This four-step synthetic pathway (scheme 1) has as starting reagents carbomethoxyferuloyl chloride and ethyl acetoacetate.[80] The first step of this reaction includes the condensation of the starting reagents with the consequent formation of the derivative **A**, followed by a saponification and decarboxilation in the second step where the derivative **B** is obtained. In the third step, **B** suffers a condensation with carbomethoxyferuloyl chloride giving origin to **C**. In the last step of the pathway, **C** is heated to high temperatures in acetic acid and the saponification and decarboxilation reactions occur giving the desired product, curcumin.

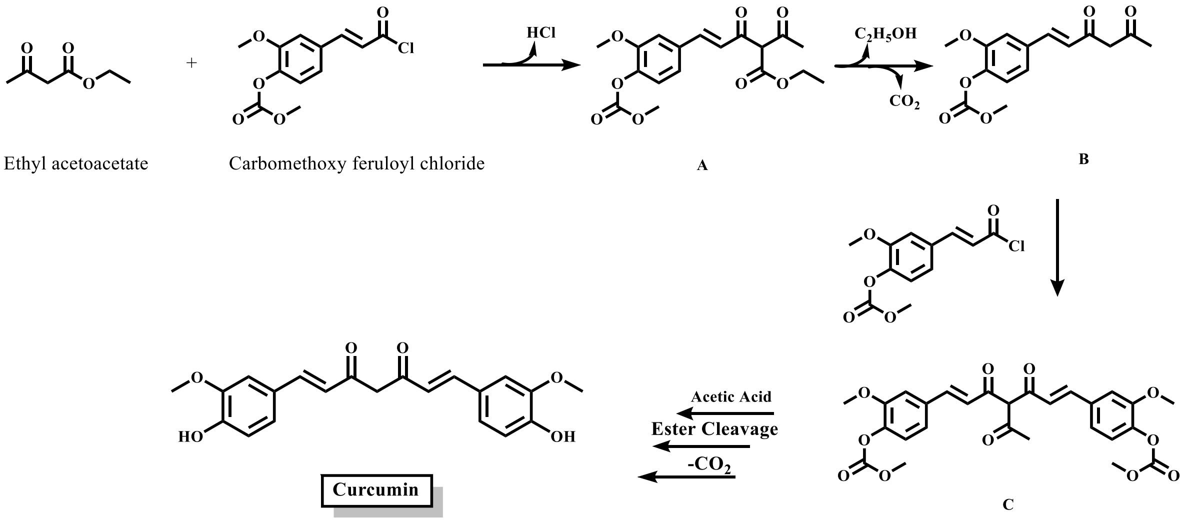

Scheme 1: Synthesis pathway described by Lampe in 1918.[80]

About 30 years later, in 1950, Pavolini described an improvement of the Lampe's pathway, however the reaction yield was not more than 10%.[81] The synthesis involves the direct reaction of two vanillins with acetylacetone, using boron trioxide as a catalyst. This route is described in scheme 2.

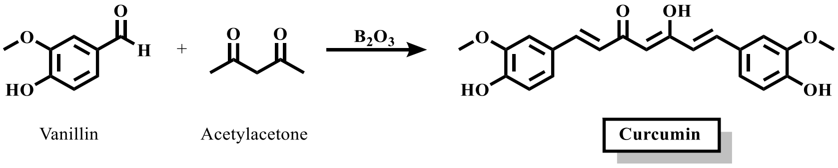

Scheme 2: Synthesis pathway described by Pavolini in 1950.[81]

Later in 1964, Pabon[82] described an easy synthetic pathway of curcumin (scheme 3) that has been used until nowadays with slight modifications and with an improvement in yields.[83–85] The synthesis described by Pabon starts with acetylacetone and boric acid at 75 ºC to form the protected complex of acetylacetone. This step is extremely important to protect the carbon 3 of 2,4-pentanedione. If this step is missed, the Knoevenagel condensation will occur in C-3, due to these hydrogens being more acidic, instead of occurring in C-1 and C-5. After protection, vanillin, and trialkyl borate, at 100 ºC, are added to the boron complex of acetylacetone, and, finally, butylamine is added as a catalyst.[82] Some variations of Pabon reaction are using another boron-based reagent such as boron trifluoride etherate[84] in the protection of acetylacetone, and using other strong amines being piperidine an example.[83] At the end of the reaction, the curcumin is still complexed with the boron difluoride and this complex can be deprotected by the addition of HCl at 50 ºC[82] or by heating it to 100 ºC in dimethyl sulfoxide–methanol to give curcumin in a good yield.[84] If the intended synthesis is another symmetrical curcuminoid beyond curcumin, another aldehyde should be used instead of vanillin, for an asymmetrical curcuminoid two different aldehydes should be used in the same reaction.

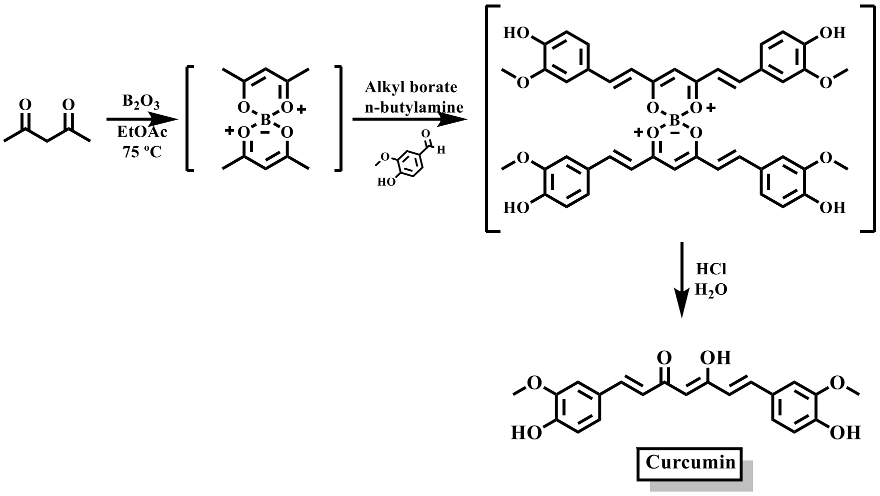

Scheme 3: Synthesis pathway described by Pabon in 1964.[82]

In 2006, Nichols group[86] reported a new synthesis using microwave (MW) irradiation. The reaction consisted of mix cycloalkanone with boron oxide, the appropriate aromatic aldehyde, acetic acid and finally morpholine.[86] The MW-assisted reaction is completed in a few minutes, unlike the Pabon reaction that needs a few hours to be finished.[82]

Several pathways to the synthesis of curcumin derivatives have been described with slight modifications, such as a different boron reagent, amine or solvent, regarding the Pabon reaction. However, the principle is the same as Pabon described. In 2013, Liu and co-workers described several curcuminoids complexed with a BF_2-group (BF_2-curcumin) synthesis using Pabon's method, with $BF_3 \cdot OEt_2$ as boron reagent, in very good yields.[84] In 2014, Fedorenko and his group described a BF_2-curcumin analogs synthesis using acetic anhydride as solvent without the presence of any base with yields of around 60%.[87] Also in 2014, Guifeng Bai synthesized BF_2-curcumin derivatives using piperidine as a catalytic base. Although, in this last synthesis it was possible to obtain the BF_2-curcumin derivatives, their yields were lower than those already described (around 30%).[88]

1.4. Eukaryotic cell models

Eukaryotic cells are characterized by a defined compartment, limited by a membrane, where the genetic information is stored, in contrast to prokaryotic cells, and include animal, plant, fungal, and protist organisms. In this section two types of cells will be approached: fungal and animal (tumoral cells) cells and their role as cell models.

1.4.1. Fungal cell

Fungi morphology is varied and changes throughout their life cycle, for different environmental conditions, for different fungal groups. Often, fungi grow as a mycelium, an organized network of hyphae (interconnected elongated cells) that propagates through the substrate acting as transportation via for nutrient and important metabolites (as enzymes or growth regulators). Hyphae show apical growth and many important roles other than transportation, mainly in higher fungi, where it can be densely packed and form protective structures in peripheral regions of the mycelium.[89]

Fungi can assume the unicellular format, called yeast, generally adapted for liquid substrate environments. There are species capable of propagation and colony formation as yeasts and species that can develop hyphae or pseudohyphae for host tissue invasion.[89,90] Yeast shape can vary between different species and is assumed accordingly with growth polarity, which is affected by biochemical processes and is closely related to cell wall structure.[89] While yeast are characterized by being uninucleate cells, hyphae are multinucleate.[90]

Fungi are eukaryotic microorganisms that present organelles such as mitochondria, Golgi apparatus or, endoplasmc reticulum. In contrast to the animal cell, the fungal cell has a rigid cell wall.[91] The fungi cell wall has an important role in growth, shape, and interactive properties. The cell wall is usually composed of central semicrystalline components in a microfibrillar shape, mainly chitin and glucans or chitosan, and a surrounding amorphous matrix made of glucan and mannoproteins (figure 12), and its composition and organization on each constituent vary according to the fungal species.[92] In general, apical growth on hyphae is promoted by a thinner cell wall at the tip of the structure where a vesicle cluster, named Spitzenkörper, supplies the hyphae extension and is located along the apical growth direction.[89,90] Higher fungi develop septa for hyphae compartmentalization when growing. Septation promotes support of hyphae, and protection from stressed or damaged parts of mycelium. Generally, a healthy mycelium presents hyphae communicating with each other through typical perforated septa that are blocked in case of need for biochemical stress protection.[89]

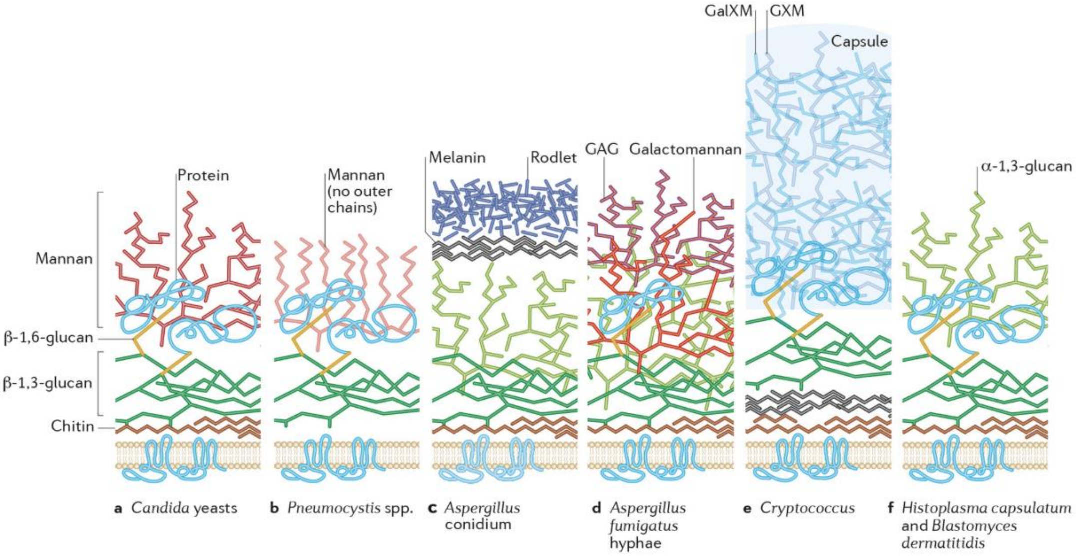

Figure 12: Cell wall organization on different fungal pathogens.[91] Adapted with permission from Gow, N. A. R., Latge, J.-P. & Munro, C. A. The Fungal Cell Wall: Structure, Biosynthesis, and Function. The Fungal Kingdom 5, 267–292 (2017). Copyright 2021 American Society for Microbiology

The reproduction and dispersion functions in fungi are attributed to the cellular structures denominated by spores which could be derived either by asexual (conidia, chlamydospores, and sporangiospores) or by sexual reproduction (ascospores, zygospores, and basidiospores). Conidia spores can still be divided into microconidia and macroconidia, a characteristic of some pathogens.[90,93] Depending on the type of spores they could be uninucleate or multinucleate. Spores are released from mycelium to germinate and then produce specialized hyphae responsible for the colony formation in the new host.[90]

Fusarium oxysporum

Fusarium oxysporum Schlechtend. (*F. oxysporum*) is a filamentous fungus that belongs to the phylum *Ascomycota* specifically to the family of *Nectriaceae* and genus *Fusarium* [Mycobank number: MB#218372]. *F. oxysporum* is a soil-borne fungus that is responsible for the infection of several plants, having an important role in worldwide crop losses and being considered one of the most destructive plant pathogens in crops.[94]

Fusarium oxysporum is characterized by having an asexual life cycle and by the production of the three types of spores, also known as conidia: macroconidia, microconidia (figure 13), and chlamydospores. The morphology of *F. oxysporum* varies in the three types: macroconidia present sickle shape with three or four septa while microconidia are oval-shaped with one or none septum. Chlamydospores are rounded-shaped with thick walls.

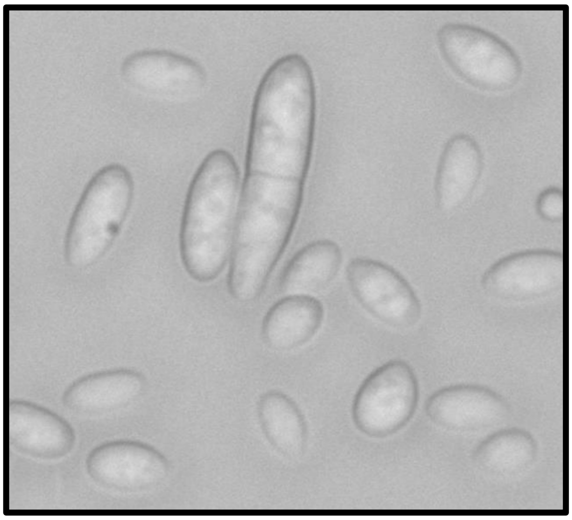

Figure 13: Microconidia spores of *Fusarium oxysporum* using brightfield microscopy.

1.4.2. Human immortalized cell line

Human immortalized cell lines are widely used in medical research for promoting tumor-like conditions, due to their ability to proliferate (almost) indefinitely.[95] These cell line are known for presenting genetically identical populations promoting consistency and reproducibility in results.[95] Some examples of the most used human immortalized cell lines are: HeLa cell line (human epithelial cell from cervical cancer), HEK-293T cell line (human embryonic kidney cell), and SH-SY5Y cell line (human neuroblastoma).[96] In this work, the cell line that will be used is the SH-SY5Y cell line.

SH-SY5Y cells

SH-SY5Y has been widely used as a neuron cell model in neurodegenerative diseases due to its ability to reproduce several functional and biochemical properties of neurons.[97] SH-SY5Y is a three-time subcloned neuroblastoma human cell line derived from the neuroblastoma cell line SK-N-SH which is originated from a biopsy of the bone marrow of a 4 years old girl.[98]

SH-SY5Y cell line is characterized by two different morphologically phenotypes: neuroblast-like (N type) and epithelial-like (S type) phenotypes. N-type non-polarized cell bodies can be differentiated into a phenotype with neuronal markers that are not present in the neuroblast-like cells.[99,100]

The first protocol to cultures of SH-SY5Y was described by Biedler *et al*. in 1978 and has been widely used until nowadays without major modifications.[101]

1.5. Viability and cytotoxicity assays

The biological evaluation of drugs or chemicals, such as fluorophores, in cells is an important step to understand their susceptibility to be used in diagnosis and treatment. Viability and cytotoxicity tests are used to measure cell viability after exposure to some drug or chemical, allowing to understand if they are toxic to cells and what is the maximum concentration that could be applied.[102]

Viability and cytotoxicity assays could be organized in several forms such as the type of measurement[102] (luminescence and fluorescence measurement, among others) or the type of test performed[103] (metabolic tests, cell growth tests, among others). Herein, they will be presented according to the type of measurement.

1.5.1. Dye exclusion assays

Dye exclusion assays are based on the interaction of a certain dye with the cell membrane and here are measured the number of viable cells.[102] In other words, cells without damages in their membrane integrity are considered viable cells and will eliminate the dye while unviable cells will not have this ability. An indirect measure of stained and non-stained cells will give the percentage of viable cells in a function of the total cells in suspension.[103,104] Dye exclusion assays include trypan blue assay, eosin assay, congo red assay, and erythrosine B assay. Among these, trypan blue is the most used.[102,104]

1.5.2. Colorimetric assays

Colorimetric assays are based on the color change in response to a certain biomarker of the metabolic activity of viable cells. This color change is measured using a spectrophotometer. The currently used assays are based on reduction of tetrazolium compounds, on neutral red uptake, and the interaction of the dyes between proteins and DNA (i.e.: crystal violet assay).[102]

Assays based on the reduction of tetrazolium compounds (MTT [3-(4,5-dimethylthiazol-2-yl)-2–5-diphenyltetrazolium bromide], MTS [5-(3-carboxymethoxyphenyl)-2-(4,5-dimethyl-thiazoly)-3-(4-sulfophenyl) tetrazolium], XTT [2,3-bis(2-methoxy-4-nitro-5-sulphophenyl)-5-carboxanilide-2H-tetrazolium], WTS-1 [2-(4-iodophenyl)-3-(4-nitrophenyl)-5-(2,4-disulfophenyl)-2H tetrazolium], WTS-8 [(2-(2-methoxy-4-nitrophenyl)-3-(4-nitrophenyl)-5-(2,4-disulfophenyl)-2H tetrazolium], INT [iodonitrotetrazolium]) measure the mitochondrial activity in viable cells, being reduced by NADH in formazan,[102,105] except for INT salt that is reduced by lactate dehydrogenase released from dead or damaged cells.[102] The quantities of reduced products are measured by spectrophotometry at specific wavelengths.[105]

Neutral red uptake (NRU) is one of the most used assays. NRU crosses the cell membrane through passive diffusion and accumulates in lysosomes, which starts a proton gradient to maintain the pH and neutral red stays charged and stains lysosomes, allowing its spectrophotometric measurement.[102]

1.5.3. Fluorometric assays

Fluorometric assays are based on the detection of fluorescence produced by certain dyes formed in viable cells and these assays are more sensitive than the colorimetric ones.[102] These include the alamarBlue assay,[102,106] the CFDA-AM (5-carboxyfluosceín diacetate) assay,[102] and the protease viability marker assay.[102,105]

AlamarBlue assay is based on the reduction of resazurin, a blue nonfluorescent dye, in resorufin, a pink fluorescent dye, by enzymes present in viable cells. As resazurin is cell-permeable, it enters in cells that did not suffer any damage and is reduced to resorufin by, for example, mitochondrial enzymes, producing a fluorescent signal.[102,105,106] AlamarBlue could also be considered a colorimetric assay where absorbance at 600 and 570 nm is measured, since resazurin and resofurin possess different absorption maxima, 600 and 570 nm, respectively.

Concerning the CFDA-AM assay, this is based on the transformation of 5-carboxyfluoresceín diacetate (non-fluorescent) in fluorescent carboxyfluoresceín by esterases present in the plasma membrane. The CFDA-AM is also considered an indicator of cell membrane integrity.[102,105]

In protease viability marker assay, the protease substrate glycylphenylalanyl-aminofluorocoumarin is transformed in aminofluorocoumarin and a fluorescent signal is seen. This transformation is only possible in viable cells since in dead cells the protease loses its activity.[102,105]

1.5.4. Luminometric assays

Luminometric assays are based on the same principle that fluorometric ones but luminescence is measured instead of fluorescence. Herein we include the ATP assay and real-time viability assay.[102,105]

In ATP assay, the transformation of luciferin to oxyluciferin in the presence of ATP is followed and a luminescence signal is achieved. This could not be seen in unviable cells because they lose the ability to produce ATP, an important catalyst in the reaction of the transformation of luciferin.[102,105]

Finally, in the real-time viability assay, viable cells can transform a pro-substrate (previously added) into a substrate for luciferase (also added previously). That way, if the cells remain viable luciferase will use the substrate formed and produce a luminescent signal that is measured to detect which percentage of viable cells are present.[102,105]

1.6. Objectives

The aim of this work is to synthesize several curcumin derivatives, to test their cytotoxicity in the filamentous fungus *Fusarium oxysporum* and the cell line model SH-SY5Y, and to assess their ability as fluorescent probes for cellular imaging in SH-SY5Y.

The adopted synthetic pathway was described by Liu and co-workers in 2013[84] and is represented in scheme 4.

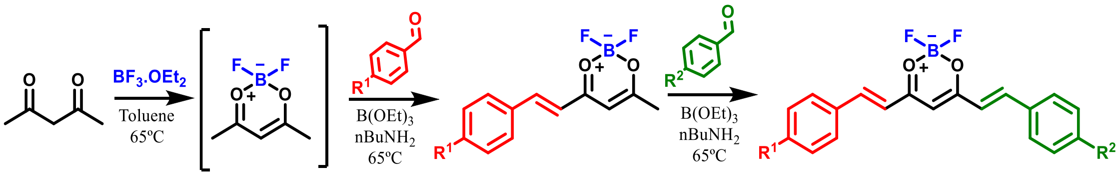

Scheme 4: Adopted synthetic pathway of curcumin derivatives.[84]

All derivatives would be fully characterized and their photophysical properties would be addressed.

The curcumin derivatives would be incubated with the phytopathogenic fungi and the human cell line model SH-SY5Y, and the cell viability would be tested. *Fusarium oxysporum* would be incubated with DAPI and visualized using fluorescence microscopy. In the case of SH-SY5Y cells, curcuminoids would be visualized using fluorescence microscopy, and their interaction with cells would be determined.

2. CHAPTER II

MATERIAL AND METHODS

2.1. Organisms and culture media

The most commonly used conditions to incubate *Fusarium oxysporum* are in a Potato Dextrose Agar (PDA) medium at 28 ºC for 7 days,[107–109] presenting a white cotton-like appearance (figure 14).

Fusarium oxysporum used in this work was grown in Potato Dextrose Agar (PDA, Liofilchem) at 25ºC for 7 days.

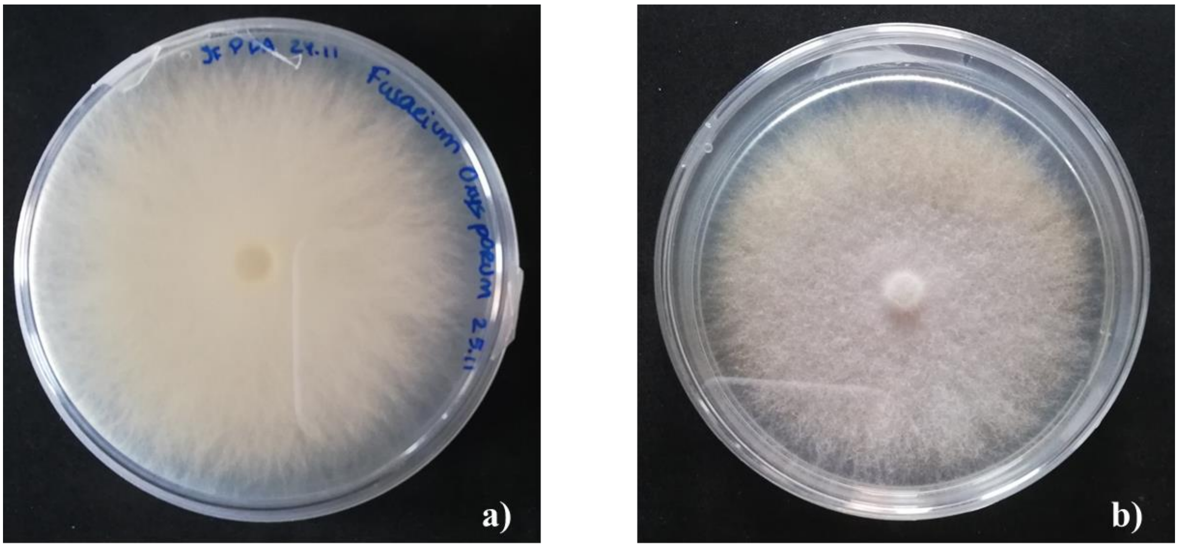

Figure 14: *Fusarium oxysporum* culture in PDA. a) Colony lower surface; b) Colony upper surface.

2.2. Fluorophores synthesis

In this work, 3 routes will be approached to synthesize derivatives **2a-b**, **3a-f** and **4** (scheme 5 and 6). The following sections will describe the general procedures and the synthesis of these derivatives.

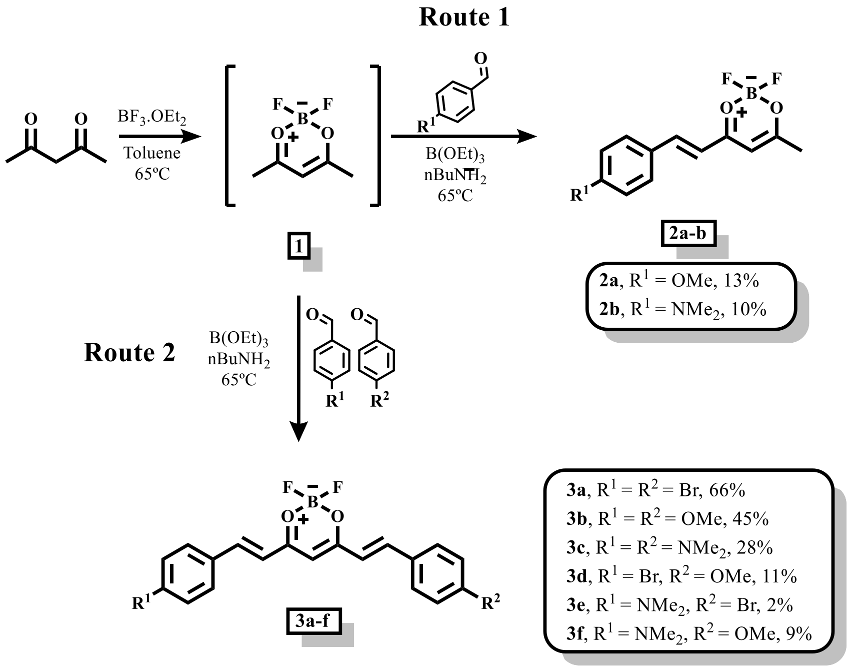

Scheme 5: Synthetic route for the synthesis of curcumin analogs **2a-b**, **3a-f**.

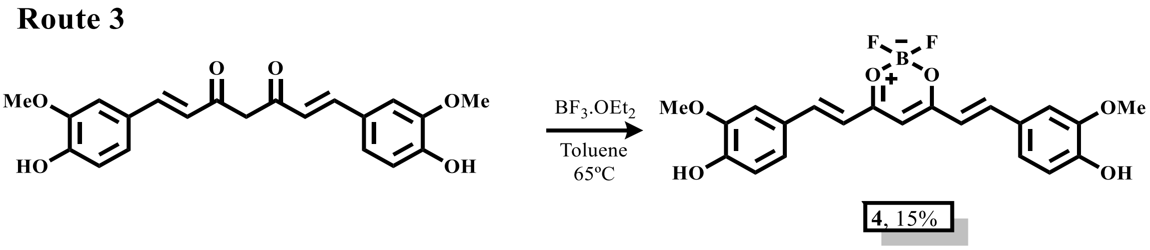

Scheme 6: Synthetic route for the synthesis of curcumin analog **4**.

2.2.1. General

Melting points were measured in a BÜCHI Melting point B-540 apparatus fitted with a microscope and are uncorrected. NMR spectra were recorded with Bruker DRX 300 and 500 spectrometers (300 and 500 for ^{1}H, 75 and 126 for ^{13}C and 282 MHz for ^{19}F), in $CDCl_3$ as solvent, if not stated otherwise. Chemical shifts (δ) are reported in ppm and coupling constants (*J*) in Hz; internal standard was residual peak of the solvent. Unequivocal ^{13}C assignments were made with the aid of 2D gHSQC and gHMBC (delays for one-bond and long-range *J*C/H couplings were optimised for 145 and 7 Hz, respectively) experiments. High resolute mass spectra analyses (HRMS-ESI.) were performed on a microTOF (focus) mass spectrometer. Ions were generated using an

ApolloII (ESI) source. Ionization was achieved by electrospray, using a voltage of 4500 V applied to the needle, and a counter voltage between 100 and 150 V applied to the capillary. Absorption spectra were collected with UV-2501PC, emission and excitation spectra were collected with JASCO Spectrofluorometer FP-8300.

Preparative thin-layer chromatography was performed with Macherey-Nagel G/ UV 254. Column chromatography was performed with ACROS Organics silica gel 60A (0.030-0.200 mm). All other chemicals and solvents used were obtained from commercial sources and were either used as received or dried by standard procedures.

2.2.2. General procedures

i. Procedure for the synthesis of derivative 1[110]

Acetylacetone (1 equiv., 1 mmol) and $BF_3 \cdot OEt_2$ (1.5 equiv., 1.5 mmol) were mixed in toluene (5 mL) at 65ºC. After stirring for 30 minutes, water was added and the organic layer was extracted with CH_2Cl_2 (3 x 15 mL), collected, and dried over anhydrous sodium sulfate. Finally, the solution was concentrated to dryness to afford the compound **1** as an off-white solid.

ii. General procedure for the synthesis of derivatives 2a-b

Acetylacetone (1 equiv., 1 mmol, 0.105 mL) and $BF_3 \cdot OEt_2$ (1.5 equiv., 1.5 mmol, 0.185 mL) were mixed in toluene (4 mL) at 65ºC during 30 minutes. To the mixture at 65ºC and while stirring, the appropriate benzaldehyde (1 equiv., 1 mmol) and $B(OEt)_3$ (2 equiv., 2 mmol, 0.340 mL) were added. Then, $nBuNH_2$ (0.2 equiv., 0.2 mmol, 0.020 mL) was added and the mixture was stirred at 65ºC for 5 hours. Water was added and the organic layer was extracted with CH_2Cl_2 (3 x 15 mL), collected, and dried over anhydrous sodium sulfate. Finally, the solution was concentrated to dryness. The product was precipitated from CH_2Cl_2 and hexane and dried in air or purified by silica gel thin-layer chromatography using CH_2Cl_2 as eluent.

iii. General procedure for the synthesis of derivatives 3a-f

Acetylacetone (1 equiv., 1 mmol, 0.105 mL) and $BF_3 \cdot OEt_2$ (1.5 equiv., 1.5 mmol, 0.185 mL) were mixed in toluene (4 mL) at 65ºC during 30 minutes. To the mixture at 65ºC, the appropriate benzaldehyde (2 equiv., 2 mmol) or benzaldehydes (1 equiv. each, 1 mmol each) and $B(OEt)_3$ (2 equiv., 2 mmol, 0.340 mL) were added. Then, $nBuNH_2$ (0.2 equiv., 0.2 mmol, 0.020 mL) was added and the mixture was stirred at 65ºC for 5 to 21 hours. Water was added and the organic layer was extracted with CH_2Cl_2 (3 x 15 mL), collected, and dried over anhydrous sodium sulfate. Finally, the solution was concentrated to dryness. The product was precipitated from CH_2Cl_2 and hexane and dried in air or purified by silica gel thin-layer chromatography using CH_2Cl_2 as eluent.

2.2.3. Synthesis

i. Synthesis of 2,2-difluoro-4,6-dimethyl-2*H*-1λ^3,3,2λ^4-dioxaborinine (1)[110]

Using the procedure described in section 2.2.2.i., 1 mmol of acetylacetone and 1.5 mmol of $BF_3 \cdot OEt_2$ were mixed for 30 minutes at 65ºC and a yellow solution was obtained. Water was added (15 mL) and the product was extracted with 3 x 15 mL of CH_2Cl_2 and dried over anhydrous sodium sulfate. The pure product was obtained as an off-white solid (0.162 g). Yield: quantitative; ^{1}H NMR (300 MHz, $CDCl_3$) δ 6.00 (s, 1H), 2.25 (s, 6H); ^{19}F NMR (282 MHz, $CDCl_3$) δ -134.51 (^{10}B - 0.2 ^{19}F), -134.57 (^{11}B - 0.8 ^{19}F).

ii. Synthesis of (*E*)-2,2-difluoro-4-(4-methoxystyryl)-6-methyl-2*H*-1λ^3,3,2λ^4-dioxaborinine (2a)

Using the procedure described in section 2.2.2.ii., *p*-methoxybenzaldehyde (1 equiv., 1 mmol, 0.121 mL) was added. After column purification with CH_2Cl_2/Hex (1:1) and CH_2Cl_2, the product **2a** was obtained as a yellow solid (0.0342g). Yield: 13%; mp: 136-139ºC; ^{1}H NMR (300 MHz, $CDCl_3$) δ 8.05 (d, *J* = 15.6 Hz, 1H), 7.58 (d, *J* = 8.8 Hz, 2H), 6.95 (d, *J* = 8.8 Hz, 2H), 6.51 (d, *J* = 15.6 Hz, 1H), 5.96 (s, 1H), 3.88 (s, 3H, OMe), 2.32 (s, 3H, Me); ^{13}C NMR (75 MHz, $CDCl_3$) δ 190.37 (CO), 180.80 (CO), 163.10, 148.60, 131.41, 126.58, 117.06, 114.82, 101.13, 55.57 (OMe), 24.22 (Me); ^{19}F NMR (282 MHz, $CDCl_3$) δ -136.19 (^{10}B - 0.2 ^{19}F), -136.29 (^{11}B - 0.8 ^{19}F); ESI/HRMS on going.

iii. Synthesis of (*E*)-4-(2-(2,2-difluoro-6-methyl-2*H*-1λ^3,3,2λ^4-dioxaborinin-4-yl)vinyl)-*N*,*N*-dimethylaniline (2b)

Using the procedure described in section 2.2.2.ii., *p*-(dimethylamino)benzaldehyde (1 equiv., 1 mmol, 0.149 g) was added. After purification by silica gel thin-layer chromatography with CH_2Cl_2/Hex (1:1) and CH_2Cl_2, the product **2b** was obtained as a red solid (0.0187g). Yield: 10%; mp: 181-184ºC; ^{1}H NMR (500 MHz, $CDCl_3$) δ 8.05 (d, *J* = 15.3 Hz, 1H), 7.52 (d, *J* = 9.0 Hz, 2H), 6.69 (d, *J* = 9.0 Hz, 2H), 6.38 (d, *J* = 15.3 Hz, 1H), 5.87 (s, 1H), 3.10 (s, 6H, NMe_2), 2.27 (s, 3H, Me); ^{13}C NMR (126 MHz, $CDCl_3$) δ 187.14 (CO), 180.71 (CO), 153.23, 150.09, 132.75, 121.92, 115.00, 111.92, 100.84, 40.15 (NMe_2), 23.96 (Me); ^{19}F NMR (282 MHz, $CDCl_3$) δ -137.09 (^{10}B - 0.2 ^{19}F), -137.15 (^{11}B - 0.8 ^{19}F); ESI/HRMS m/z: $[M + Na]^+$ Calcd for $C_{14}H_{16}O_2NBF_2Na$ 302.1140; Found 302.1128.

iv. Synthesis of 4,6-bis((*E*)-4-bromostyryl)-2,2-difluoro-2*H*-1λ^3,3,2λ^4-dioxaborinine (3a)[84]

Using the procedure described in section 2.2.2.iii., *p*-bromobenzaldehyde (2 equiv., 2 mmol, 0.185 g) was added. After column purification with CH_2Cl_2/Hex (1:1) and CH_2Cl_2, the product **3a** was obtained as an orange solid (0.320g). Yield: 66%; mp > 289 ºC (degradation); ^{1}H NMR (500 MHz, $CDCl_3$) δ 8.02 (d, *J* = 15.6 Hz, 2H), 7.59 (d, *J* = 8.5 Hz, 4H), 7.49 (d, *J* = 8.5 Hz, 4H), 6.73 (d, *J* = 15.6 Hz, 2H), 6.10 (s, 1H); ^{13}C NMR (126 MHz, $CDCl_3$) δ 180.21 (CO), 146.38, 132.81, 132.62, 130.43, 126.71 (CBr), 121.00, 102.54; ^{19}F NMR (282 MHz, Acetone) δ -135.47 (^{10}B - 0.2 ^{19}F), -135.53 (^{11}B - 0.8 ^{19}F).

v. Synthesis of 2,2-difluoro-4,6-bis((*E*)-4-methoxystyryl)-2*H*-1λ^3,3,2λ^4-dioxaborinine (3b)[84]

Using the procedure described in section 2.2.2.iii., *p*-methoxybenzaldehyde (2 equiv., 2 mmol, 0.242 mL) was added. The product **3b** was obtained by crystallization from CH_2Cl_2 and hexane as purple crystals (0.172g). Yield: 45%; mp: 242-245ºC; ^{1}H NMR (300 MHz, $CDCl_3$) δ 8.00 (d, *J* = 15.5 Hz, 2H), 7.57 (d, *J* = 8.8 Hz, 4H), 6.94 (d, *J* = 8.8 Hz, 4H), 6.58 (d, *J* = 15.5 Hz, 2H), 6.01 (s, 1H), 3.87 (s, 6H, OMe); ^{13}C NMR (75 MHz, $CDCl_3$) δ 179.48 (CO), 162.80, 146.90, 131.21, 126.99, 118.07, 114.76, 102.06, 55.55 (OMe); ^{19}F NMR (282 MHz, $CDCl_3$) δ -137.38 (^{10}B - 0.2 ^{19}F), -137.44 (^{11}B - 0.8 ^{19}F); ESI/HRMS m/z: $[M - F]^+$ Calcd. for $C_{21}H_{19}O_4BF$ 365.1360; Found 365.1349.

vi. Synthesis of 4,4'-((1*E*,1'*E*)-(2,2-difluoro-2*H*-1λ^3,3,2λ^4-dioxaborinine-4,6-diyl)bis(ethene-2,1-diyl))bis(*N*,*N*-dimethylaniline) (3c)[84]

Using the procedure described in section 2.2.2.iii., *p*-(N,N-dimethylamino)benzaldehyde (2 equiv., 2 mmol, 0.300 g) was added. The product **3c** was obtained by precipitation from CH_2Cl_2 and hexane as a black solid (0.115g). Yield: 28%; mp: 312-315ºC; ^{1}H NMR (300 MHz, $CDCl_3$) δ 7.96 (d, *J* = 15.3 Hz, 2H), 7.51 (d, *J* = 8.9 Hz, 4H), 6.68 (d, *J* = 8.9 Hz, 4H), 6.46 (d, *J* = 15.3 Hz, 2H), 5.89 (s, 1H), 3.08 (s, 12H); ^{13}C NMR (126 MHz, $CDCl_3$) δ 177.87 (CO), 152.66, 146.84, 131.40, 122.37, 114.96, 111.90, 100.979, 40.15 (NMe_2); ^{19}F NMR (282 MHz, $CDCl_3$) δ -138.77 (^{10}B – 0.2 ^{19}F), -138.84 (^{11}B – 0.8 ^{19}F); ESI/HRMS m/z: $[M - F]^+$ Calcd. for $C_{23}H_{25}O_2N_2BF$ 391.1993; Found 391.1982.

vii. Synthesis of 4-((*E*)-4-bromostyryl)-2,2-difluoro-6-((*E*)-4-methoxystyryl)-2*H*-1λ^3,3,2λ^4-dioxaborinine (3d)

Using the procedure described in the section 2.2.2.iii., *p*-bromobenzaldehyde (1 equiv., 1 mmol, 0.185 g) and *p*-methoxybenzaldehyde (1 equiv., 1 mmol, 0.121 mL) were added. After column purification with CH_2Cl_2 and silica gel thin-layer chromatography with CH_2Cl_2/Hex (1:1) two main products were obtained: derivative **3b** (0.085 g, 22% yield) and derivative **3d**. **3d** was obtained as a red solid (0.0463g). Yield: 11%; mp: 242-245ºC; ^{1}H NMR (300 MHz, $CDCl_3$) δ 8.05 (d, *J* = 15.5 Hz, 1H), 7.93 (d, *J* = 15.7 Hz, 1H), 7.59 (d, *J* = 7.3 Hz, 2H), 7.56 (d, *J* = 7.3 Hz, 2H), 7.45 (d, *J* = 8.7 Hz, 2H), 6.95 (d, *J* = 8.7 Hz, 2H), 6.70 (d, *J* = 15.7 Hz, 1H), 6.60 (d, *J* = 15.5 Hz, 1H), 6.05 (s, 1H), 3.88 (s, 3H, OMe); ^{13}C NMR (75 MHz, $CDCl_3$) δ 180.91 (CO), 178.54 (CO), 163.18, 148.26, 144.96, 133.04, 132.49, 131.53, 130.23, 126.78, 126.17, 121.31, 117.76, 114.86, 102.18, 55.59 (OMe); ^{19}F NMR (282 MHz, $CDCl_3$) δ -136.89 (^{10}B – 0.2 ^{19}F), -136.95 (^{11}B – 0.8 ^{19}F); ESI/HRMS m/z: $[M + Na]^+$ Calcd. for $C_{20}H_{16}O_3BrBF_2Na$ 455.0242; Found 455.0232.

viii. Synthesis of 4-((*E*)-2-(6-((*E*)-4-bromostyryl)-2,2-difluoro-2*H*-1,3λ^3,2λ^4-dioxaborinin-4-yl)vinyl)-*N*,*N*-dimethylaniline (3e)

Using the procedure described in section 2.2.2.iii., *p*-bromobenzaldehyde (1 equiv., 1 mmol, 0.185 g) and *p*-(N,N-dimethylamino)benzaldehyde (1 equiv., 1 mmol, 0.149 g) were added. After purification by silica gel chromatography with CH_2Cl_2/Hex(1:1)/5% MeOH, product **3e** was obtained as a green solid (0.009 g) Yield: 2%; mp: 271-274ºC; ^{1}H NMR (500 MHz, $CDCl_3$) δ 8.09 (d, *J* = 15.1 Hz, 1H), 7.87 (d, *J* = 15.6 Hz, 1H), 7.56 – 7.52 (m, 4H), 7.45 (d, *J* = 8.5 Hz, 2H), 6.70 (d, *J* = 9.0 Hz, 2H), 6.66 (d, *J* = 15.6 Hz, 1H), 6.48 (d, *J* = 15.1 Hz, 1H), 5.97 (s, 1H), 3.12 (s, 6H, NMe_2); ^{13}C NMR (126 MHz, $CDCl_3$) δ 180.64 (CO), 175.88 (CO), 153.38, 149.94, 143.02, 133.47, 132.35, 129.98, 125.46, 121.94, 121.77, 113.90, 111.98, 101.96, 40.17 (NMe_2); ^{19}F NMR (282 MHz, $CDCl_3$) δ -138.02 (^{10}B - 0.2 ^{19}F), -138.08 (^{11}B - 0.8 ^{19}F); ESI/HRMS m/z: $[M - F]^+$ Calcd. for $C_{21}H_{19}O_2NBrBF$ 426.0676; Found 426.0667.

ix. Synthesis of 4-((*E*)-2-(2,2-difluoro-6-((*E*)-4-methoxystyryl)-2*H*-1,3λ^3,2λ^4-dioxaborinin-4-yl)vinyl)-*N*,*N*-dimethylaniline (3f)

Using the procedure described in section 2.2.2.iii., *p*-methoxybenzaldehyde (1 equiv., 1 mmol, 0.121 mL) and *p*-(N,N-dimethylamino)benzaldehyde (1 equiv., 1 mmol, 0.149 g) were added. After purification by silica gel chromatography with Toluene/5% MeOH product **3f** was obtained as a green solid (0.036 g). Yield: 9%; mp: 255-258 ºC; ^{1}H NMR (500 MHz, $CDCl_3$) δ 8.03 (d, *J* = 15.2 Hz, 1H), 7.94 (d, *J* = 15.5 Hz, 1H), 7.56 (d, *J* = 8.5 Hz, 2H), 7.53 (d, *J* = 8.6 Hz, 2H), 6.94 (d, *J* = 8.5 Hz, 2H), 6.69 (d, *J* = 8.6 Hz, 2H), 6.56 (d, *J* = 15.5 Hz, 1H), 6.47 (d, *J* = 15.2 Hz, 1H), 5.94 (s, 1H), 3.87 (s, 3H, OMe), 3.10 (s, 6H, NMe_2); ^{13}C NMR (126 MHz, $CDCl_3$) δ 179.65 (CO), 177.16 (CO), 162.31, 153.05, 148.64, 145.00, 131.92, 130.80, 127.34, 122.07, 118.55, 114.65, 114.33, 111.93, 101.38, 55.51 (OMe), 40.15 (NMe_2); ^{19}F NMR (282 MHz, $CDCl_3$) δ -138.26 (^{10}B - 0.2 ^{19}F), -138.32 (^{11}B - 0.8 ^{19}F); ESI/HRMS m/z: $[M - F]^+$ Calcd. for $C_{22}H_{22}O_3NBF$ 378.1677; Found 378.1670.

x. Synthesis of 4,4'-((1*E*,1'*E*)-(2,2-difluoro-2*H*-1λ^3,3,2λ^4-dioxaborinine-4,6-diyl)bis(ethene-2,1-diyl))bis(2-methoxyphenol) (4)[84]

Using a similar procedure as described in section 2.2.2.i to obtain the intermediary BF_2–complex, the commercial curcumin 95% (1 equiv., 2.7 mmol, 0.100 mg) was dissolved in toluene (5 mL) and $BF_3{\cdot}OEt_2$ (1,5 equiv., 1.5 mmol, 0.05 mL) was added and the solution was stirred for 1 hour at 65ºC. Product **4**, after precipitation with CH_2Cl_2 and hexane, was obtained by purification by silica gel chromatography using EtOAc as an eluent as a red solid (0.017g). Yield: 15%; mp > 216 ºC (degradation); ^{1}H NMR (300

MHz, Acetone) δ 8.65 (s, 2H, OH), 7.95 (d, *J* = 15.6 Hz, 2H), 7.48 (d, *J* = 2.0 Hz, 2H), 7.37 (dd, *J* = 8.3, 2.0 Hz, 2H), 6.97-6.90 (m, 4H), 6.36 (s, 1H), 3.94 (s, 6H, OMe); ^{13}C NMR (75 MHz, Acetone) δ 179.70 (CO), 148.10, 146.73, 126.73, 124.86, 118.19, 115.67, 111.69, 101.09, 55.47 (OMe); ^{19}F NMR (282 MHz, Acetone) δ -137.53 (^{10}B – 0.2 ^{19}F), -137.59(^{11}B – 0.8 ^{19}F).

2.3. Electronic absorption and fluorescence emission properties

The electronic absorption spectra of the synthesized compounds **2b** and **3a-f** were recorded at different concentrations (between $1x10^{-7}$M and $3x10^{-5}$M) in tetrahydrofuran, ensuring that the Beer-Lambert law is followed.

Fluorescence emission spectra of the synthesized compounds **2b**, **3a-f**, **4** and curcumin were recorded at the same concentrations as the absorption spectra, ensuring that fluorescence emission is a non-saturated curve. The standard used for quantum yield calculation of compounds **2b**, **3a-b**, **3d**, and **4** (in THF) was compound **4** which presents a quantum yield of 0.62 in dichloromethane,[60] and for compounds **3c** (in THF), **3e** and **3f** was compound **3c** in DCM which presents a quantum yield of 0.47.[83] Figure 15 represents the qualitative emission of compounds **2b**, **3a-f**, **4**, and curcumin.

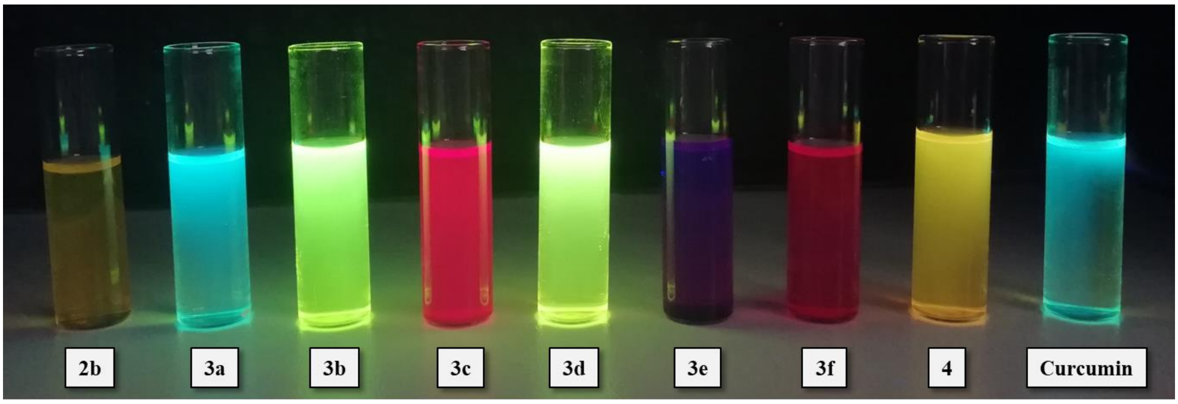

Figure 15: Qualitative emission of compounds **2b**, **3a-f**, **4** and curcumin under a UV lamp (366 nm wavelength).

2.4. Cytotoxicity to *Fusarium oxysporum*

Cytotoxicity assay was performed using a double layer medium technique, where the fluorophores (**2b**, **3a-f**, **4**, and curcumin) dissolved in acetone were incorporated in a PDA soft medium (5 g/L of agar) ensuring a fluorophore final concentration of 100 µM in each culture. This PDA soft medium was subsequently poured in a thin layer onto a PDA solid medium (15 g/L of agar). In the culture plate, two perpendicular lines (figure 16) were drawn and the fungal mycelium was inoculated in the intersection of these two lines (mycelium plug of 6 mm). Two types of controls were performed: a control where no acetone was incorporated in the PDA soft medium and a control where the same percentage of acetone was incorporated in PDA soft medium to understand the effect of acetone in the cell growth. All the cultures were incubated for 7 days, at 25 ºC, in the dark, and during the incubation, the mean diameter of mycelial growth was daily measured. Three replicates were made for each fluorophore and controls. The statistical analysis was performed on software Graphpad Prism 8.4.2.

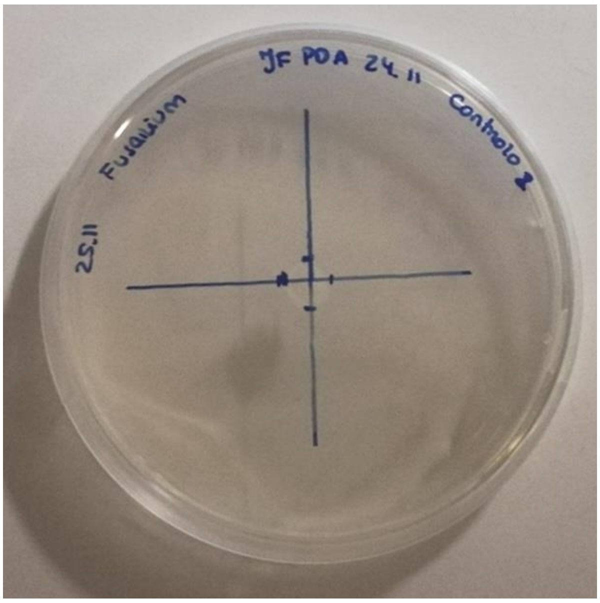

Figure 16: Representation of the two perpendicular lines for the measure of mycelial growth.

2.5. Viability in SH-SY5Y cells

The SH-SY5Y human neuroblastoma cell line, a well-known *ex vivo* neuronal model,[111] was maintained in Minimum Essential Media (MEM):F12 (1:1; Gibco, Invitrogen) supplemented with 10% FBS and 1% AA solution, and incubated in a 5% CO_2 humidified incubator at 37ºC. $1x10^4$ live cells at c.a. 60% confluence were incubated, in the dark, for 3 h with 25 and 50 μM media solutions of the fluorophores in acetone, the vehicle used in control conditions (at 0.1%). The resazurin metabolic assay was used to assess cytotoxicity.[112] Briefly, at the same time of fluorophores incubation, a resazurin

(Sigma-Aldrich) solution (0.1 mg mL^{-1} resazurin in phosphate buffer saline (PBS) [Pierce, Perbio, Thermo Scientific, Bonn, Germany]) was added to the cells' media until a final 10% solution. Reduction of resazurin to resofurin in the cells media was measured spectrophotometrically (Infinite M200 PRO, Tecan) at 570 and 600 nm, and the final O.D. calculated.[112] Data was plotted as percentage of the control cells (no fluorophores) final O.D.. Experiments were conducted in triplicate.

2.6. Cell Imaging

2.6.1. *Fusarium oxysporum* – microscopic assays

Brightfield and fluorescence visualization of *Fusarium oxysporum* was performed on a LEICA DM2000 LED microscope with a LEICA 100x objective with an aperture of 1.25, and photographs were taken using a LEICA DFC7000 T camera.

For brightfield images, the sample preparation was performed using the inverted block agar method.[50] In a sterilized slide, 20 µL of PBS were pipetted into the center and the mycelium agar block was placed on the PBS. Then a sterilized cover slide was placed on the preparation making sure that no bubbles were formed and then visualized under brightfield microscopy.

For fluorescence images, the mycelium agar block was incubated for 1 hour at 25 ºC, in the dark, with 10 µL of the nuclear dye DAPI (2µg/mL))and 10 µL of PBS. After incubation, the mycelium agar block was washed three times with PBS to remove the dye in excess. The slide preparation was performed using the same technique used for brightfield images. The visualization with the fluorescence microscopy was performed in a first instance with the brightfield technique and then with the filter DAPI and both channels were recorded. The images were processed using the software Fiji ImageJ.

2.6.2. SH-SY5Y cells – cellular staining with curcumin derivatives

After resazurin metabolic assay the cells were washed 3 times with PBS and fixed with 4% formaldehyde. Fluorescence microscopy was carried out in a motorized inverted widefield fluorescence microscope Olympus IX81 with analySIS software with a LC Plan FI 20x objective with an aperture of 0.4, using phase contrast and the filters DAPI, GFP and TRITC.

3. CHAPTER III

RESULTS AND DISCUSSION

3.1. Synthesis

The synthetic strategy toward the curcumin derivatives is based on a previously reported strategy.[84] The general synthetic route is described in schemes 7 and 8. In this section, the synthesis and characterization of derivatives **2a,b** will be presented. As their subsequent transformation into derivatives **3a-f** was not effective, the direct reaction of **1** with two different aldehydes was used to prepare the curcumin analogs **3a-f**.

In this section will be presented the attempts to optimize the synthetic route described by Liu group[84] in an attempt to isolate derivatives **2** for further reaction with a different aldehyde to obtain an asymmetric derivative of curcumin (**3**) (scheme 7). However, the synthesis and isolation of derivatives **2** proved not to be effective and the direct reaction of two different aldehydes to obtain derivatives **3** was performed. The complete characterization of the obtained derivatives is also demonstrated.

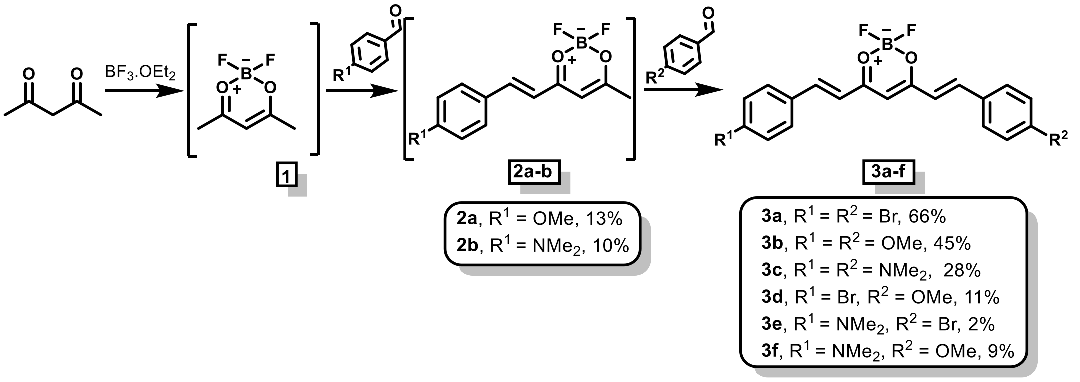

2a, R^1 = OMe, 13%
2b, R^1 = NMe_2, 10%

3a, R^1 = R^2 = Br, 66%
3b, R^1 = R^2 = OMe, 45%
3c, R^1 = R^2 = NMe_2, 28%
3d, R^1 = Br, R^2 = OMe, 11%
3e, R^1 = NMe_2, R^2 = Br, 2%
3f, R^1 = NMe_2, R^2 = OMe, 9%

Scheme 7: Synthetic route for the synthesis of curcumin analogs **2a-b** and **3a-f**.

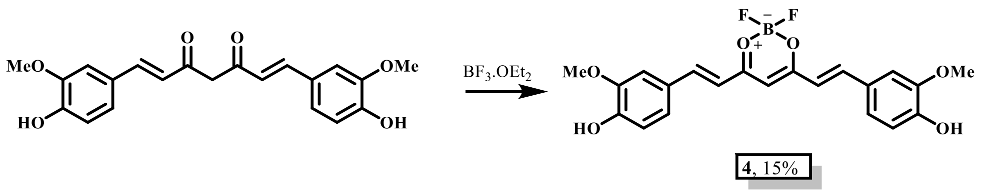

4, 15%

Scheme 8: Synthetic route for the synthesis of curcumin analog **4**.

3.1.1. Synthesis of derivatives 2a-b and NMR characterization

To perform the synthesis of the curcumin derivatives **2**, several reaction conditions were tested in order to find the optimal conditions for this reaction.

All the experimental conditions tested for the synthesis of derivative **2a** are represented in Table 1. The first synthesis attempt (table 1, entry 1) was based on the reaction described by Rivoal *et al.* [113] where 1 equivalent of acetylacetone and 0.5 equivalent of boron reagent were dissolved in ethyl acetate at 60ºC for 30 minutes. Then 1 equivalent of the desired benzaldehyde and 1 equivalent of alkyl borate, in ethyl acetate, were added to the previous mixture. After 30 minutes the catalytic base was added.[113] The first attempt did not go as expected and some modifications were made to obtain **2a**, as changing the solvent (to toluene), the base (to piperidine) and the time of reaction, however, the reaction did not work (table 1 entry 2-6). That way, the pathway described by Liu and co-workers in 2013[84] was tried, where toluene, $nBuNH_2$, and 65 ºC were used resulting in derivative **2a** (table 1 entry 7). Nevertheless, the yield is still low.

Table 1: Experimental reaction conditions for the synthesis of derivative **2a**.

Entry	R^1	Δ (ºC)	Time	Solvent	Base	Yield (%)	Ref
1[a]	-OMe	60	19h	EtOAc (10 mL)	$nBuNH_2$	0	[113]
2[b]	-OMe	rt	5h30	EtOAc	Piperidine	0	---
3	-OMe	rt	3h	Toluene	Piperidine	0	[113]
4	-OMe	rt	17h	Toluene (10 mL)	Piperidine (2 drops)	0	---
5	-OMe	rt	18h	Toluene	Piperidine	0	[113]
6	-OMe	rt	22h	Toluene (5 mL)	Piperidine (0.1 mL)	0	[113]
7	-OMe	65	4h30m	Toluene	$nBuNH_2$	13	[84]

[a] 3 equivalent of acetylacetone, 4.5 equivalent of BF_3OEt_2 and 0.6 equivalent of base were used.

[b] 2 equivalent of base were used.

Applying the synthetic pathway described in entry 7 of table 1, different aldehydes were used to obtain other derivatives. Some adaptions were needed (table 2). However, only *p*-(N,N)-dimethylbenzaldehyde and *p*-methylbenzaldehyde (traces) were successful.

Table 2: Experimental reaction conditions for the synthesis of derivatives **2**, in toluene.

Entry	**R^1**	**Δ (ºC)**	**Time**	**Solvent (mL)**	**Base**	**Yield (%)**	**Ref**
1	-OMe	65	4h30m	2	$nBuNH_2$	13	[84]
2	$-NMe_2$	65	1h15m	2	$nBuNH_2$	10	[84]
3[a]	-Me	100	3h	5	Et_2NH	3 (traces)	---
4[b]	-Br	65	20h	2	$nBuNH_2$	0	---
5[a]	-Br	100	21h30m	5	Et_2NH	0	---
6[c]	-Me	rt	25m	5	NaH	0	---
7	-OH	100	8h	2	Et_3N	0	---
8	$-NO_2$	65	2h30m	2	$nBuNH_2$	0	[84]
9	-H	65	7h15m	2	$nBuNH_2$	0	[84]

[a] 2 equivalent of base were used.

[b] 2 equivalent of acetylacetone were used.

[c] 1.5 equivalent of base were used.

This synthetic pathway, to obtain the derivatives **2,** proved to be not so effective even with the changes on the reaction conditions and at the end of most reactions, the starting reagents were always present in the initial proportion. However, in some experiments, derivative **2** was obtained, with a low yield, and in others the condensation happens on both sides, obtaining derivative **3**. The aldehydes used in the attempt to obtain derivative **2** include the aldehydes with -OMe, -Br, $-NMe_2$, -Me, -OH, $-NO_2$, and -H as substituent. The only substituents that yield derivative **2** were -OMe (**2a**), $-NMe_2$ (**2b**), and -Me (traces) in very low yields. Considering the mechanism of the reaction described in scheme 9, we could understand that the first step is characterized by the deprotonation of the terminal methyl group promoted by a base, being, in this case, an amine, forming a carbanion. Then the carbanion group will react with an aldehyde to form the double bond after water release.

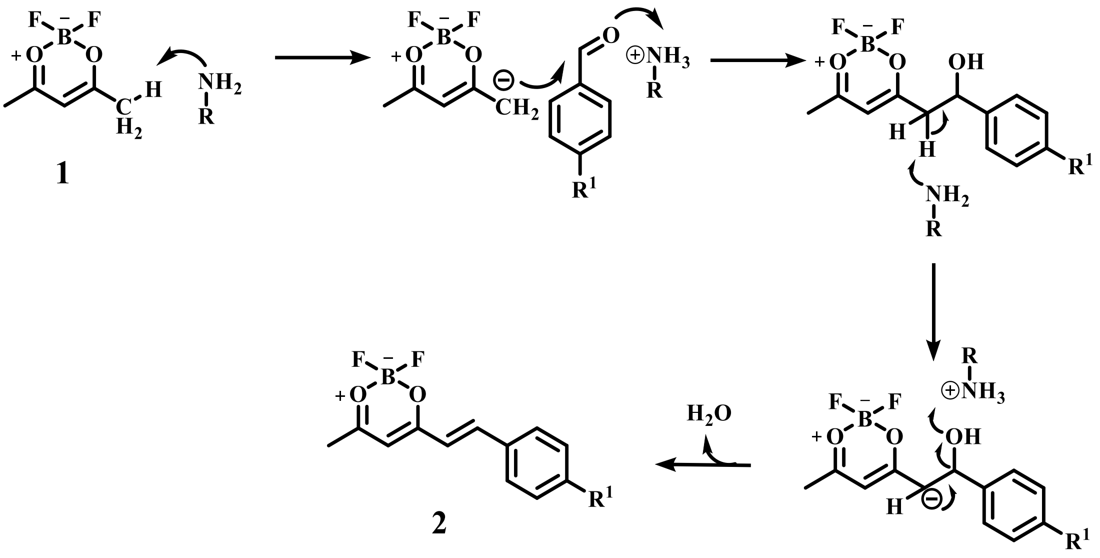

Scheme 9: Reaction mechanism of derivatives **2** synthesis.

As described in section 2.2.2.ii, when derivative **1** is formed, the aldehyde is added before the base. As the reaction shows to be more prone to the reaction on both sides of the derivative **1**, a possible way to obtain only derivative **2** is the addition of an excess of acetylacetone, to have more derivative **1** available, and force the reaction with the addition of the amine, allowing the formation of the carbanion, and only then slowly add the desired aldehyde. However, there is the problem that the excess of amine could react with the aldehyde forming an imine. To solve this problem addition of a large excess of acetylacetone is necessary so that when the aldehyde is added there is a large amount of the carbanion of derivative **1**. This strategy was tested for derivative **2a** and, after analysis of the ^{1}H NMR and ^{19}F NMR spectra, seems that derivative **2a** is present in the reaction mixture. However, the purification was complex and the pure **2a** was not obtained.

NMR spectroscopy for derivatives 2

Both derivatives **2a-b** were fully characterized by NMR spectroscopy (^{1}H, ^{13}C, ^{19}F, COSY, HSQC, HMBC). Herein will be presented the assignment peaks for derivative **2b** as an example to explain the assignments in these derivatives.

Figure 17 represents the ^{1}H NMR spectrum of derivative **2b**. The singlet at 2.27 ppm indicates the presence of one terminal methyl group, showing that the reaction only occurred on one side of the acetylacetone. The doublets at 8.05 ppm and 6.38 ppm (*J*= 15.3 Hz), each one integrating for 1 proton, prove that the double bond is present, and the coupling constant of 15.3 Hz indicates that it is in *E* configuration. The proton of the boron complex appears as a singlet at 5.87 ppm. Finally, the aromatic protons appear as two doublets at 7.52 and 6.69 ppm.

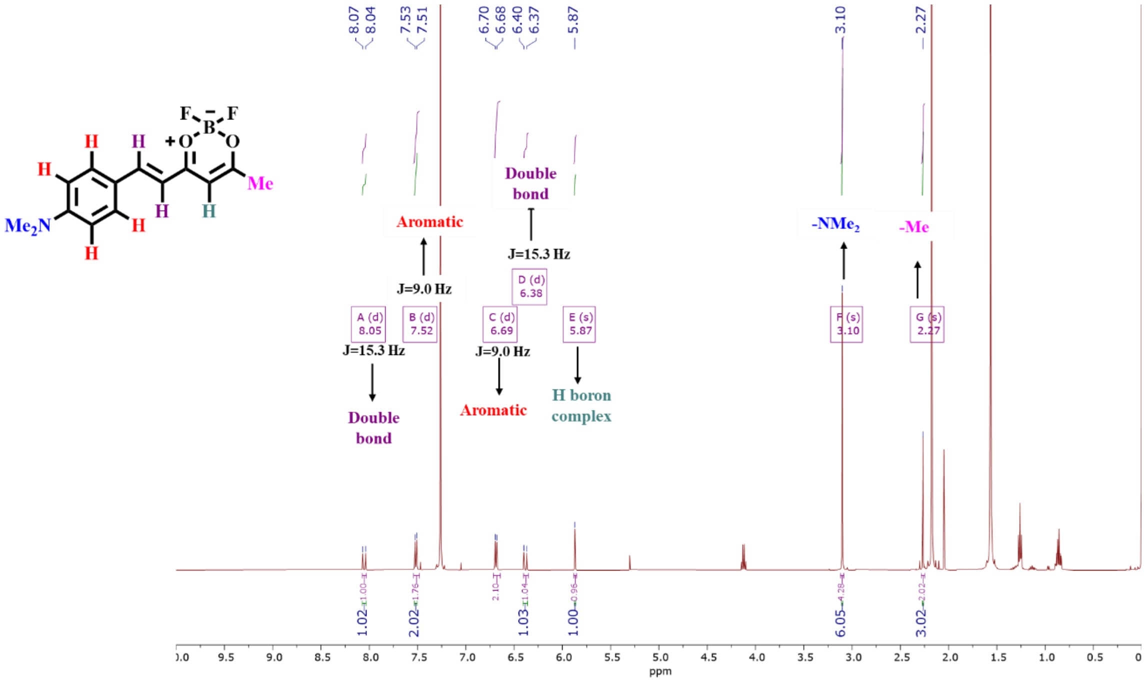

Figure 17: ^{1}H NMR spectrum and assignments for derivative **2b**.

COSY NMR spectrum (figure 18) shows the coupling between the protons. Herein we can confirm that the aromatic protons only couple with each other, and that the protons of the double bond also couple with each other, as expected.

Figure 19 represents the ^{19}F NMR spectrum and two peaks can be seen, corresponding to the fluor atoms present in the molecule. Despite the two fluor atoms being equivalent, two different peaks are seen due to the isotopic effect of the neighboring boron atom, which presents two different isotopes, ^{10}B and ^{11}B. The integration of the peaks is due to the relative abundance of boron that is around 20% for ^{10}B and around 80% for ^{11}B. The presence of these two singlets, and their proportions, confirms the presence of the fluoroborate complex.

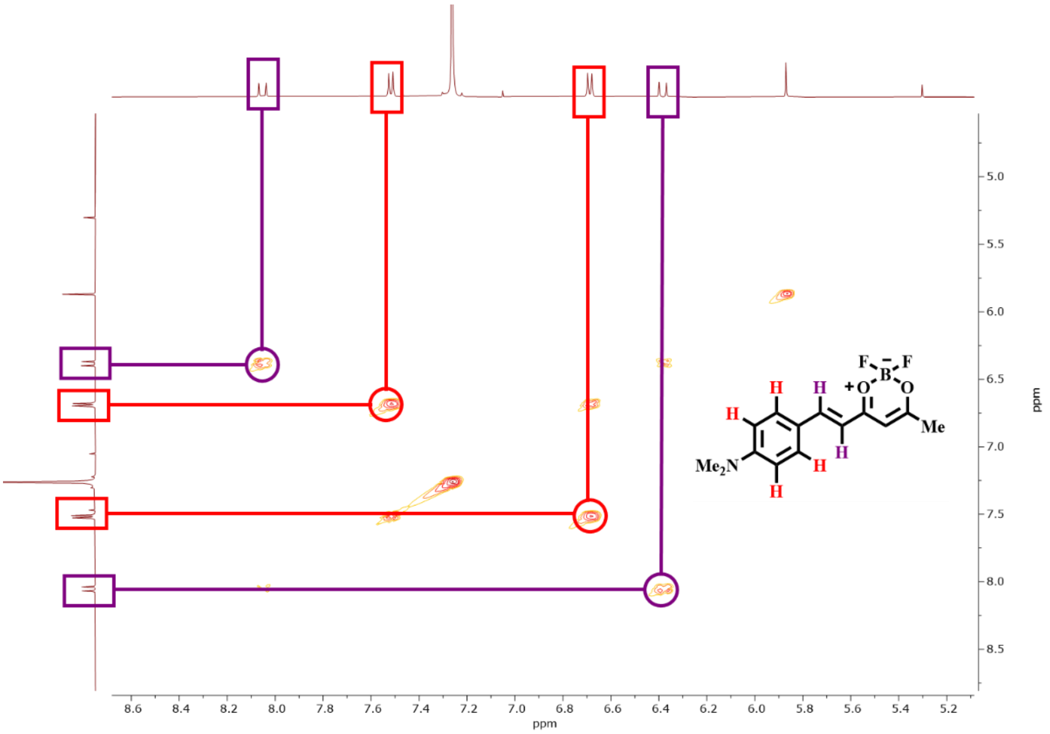

Figure 18: COSY NMR spectrum and assignments for derivative **2b**.

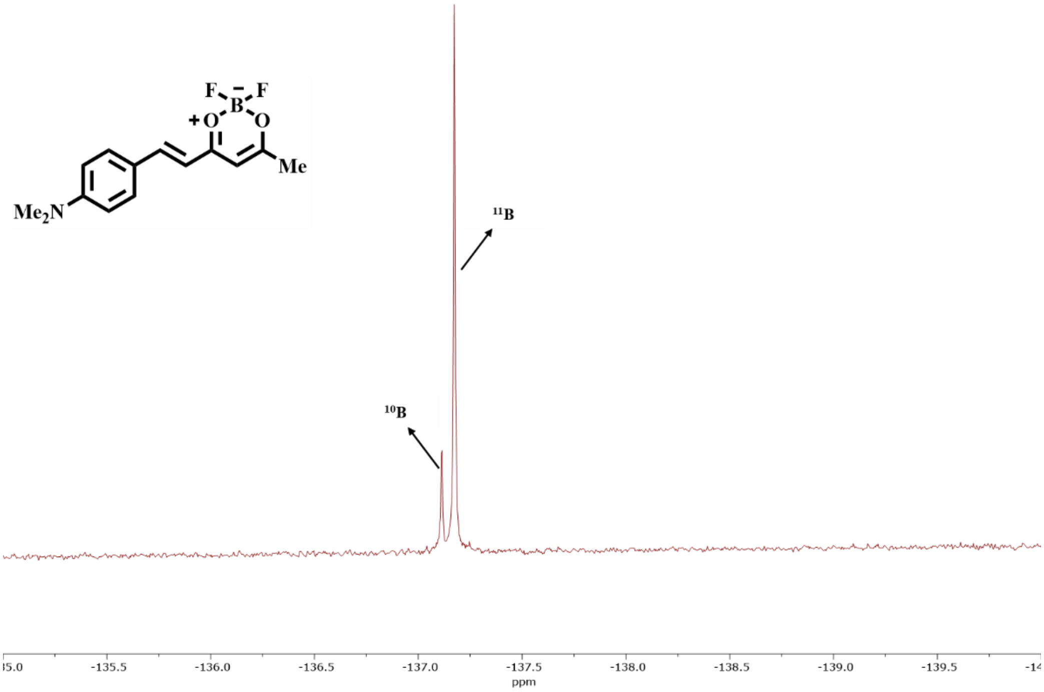

Figure 19: ^{19}F NMR spectrum for derivative **2b**.

The bidimensional NMR spectroscopy helps in the attribution of each carbon peak. That way, before the analysis of the ^{13}C NMR spectrum (figure 22) it is useful to analyze the bidimensional spectra HSQC (figure 20) and HMBC (figure 21). Analyzing the HSQC spectrum it is possible to attribute the correlations at 1 bond between carbons and protons. Looking at the correlation peaks, it is possible to attribute the carbon peak at 23.96 ppm to the terminal methyl group and the carbon peak at 40.15 ppm to the equivalent carbons of the N,N-dimethylamino group. It is also possible to attribute the carbon peak at 100.84 ppm to the carbon of boron complex, as it is correlated to the respective proton.

Concerning the analysis of the HMBC spectrum (figure 21), it is possible to attribute the correlations at 2 to 3 bonds between carbons and protons. That way, the protons of the methyl group only correlate with two different carbons, being one of them the carbon of the boron complex (3 bonds). The other carbon which correlates at 2 bonds is the carbon of the carbonyl group closer to the methyl group. That way, it is possible to conclude that the peak of this carbon is at 187.14 ppm. In the same way, the peak of the second carbonyl group could be discovered. The -H of the boron complex only couples with one more carbon at 2 or 3 bonds that correspond to the second carbonyl group with a peak at 180.71 ppm.

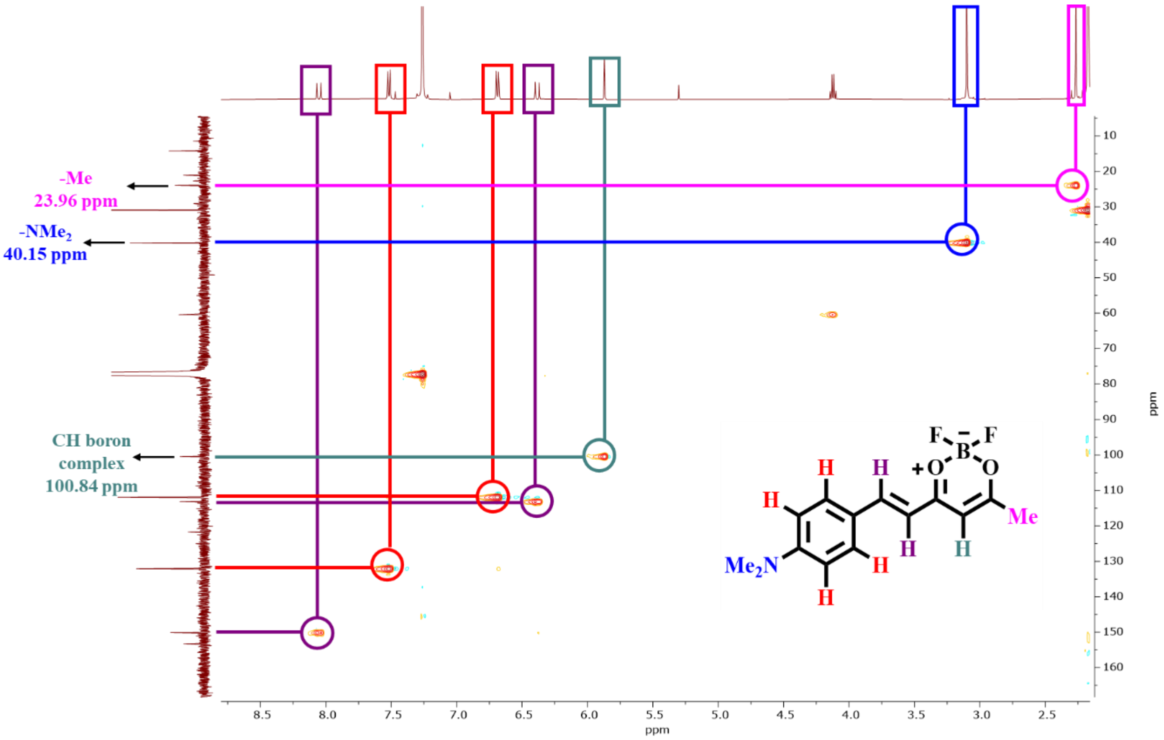

Figure 20: HSQC NMR spectrum and assignments for derivative **2b**.

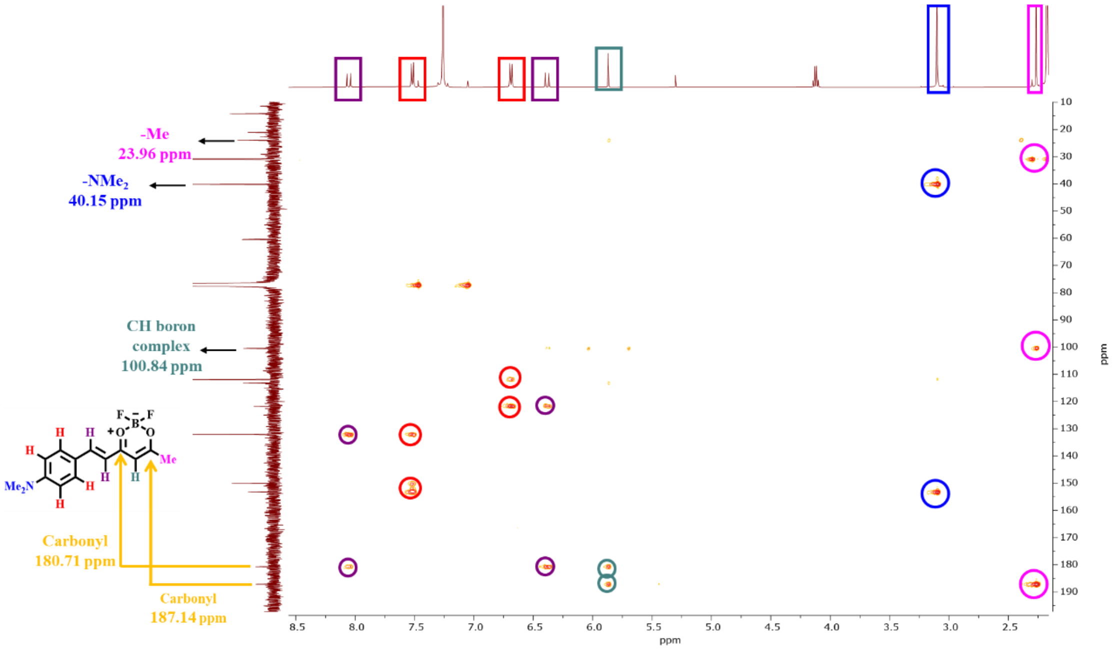

Figure 21: HMBC NMR spectrum and assignments for derivative **2b**.

Finally, it is possible to correlate the other carbon peaks in the ^{13}C NMR spectrum to the correspondent protons in the molecule.

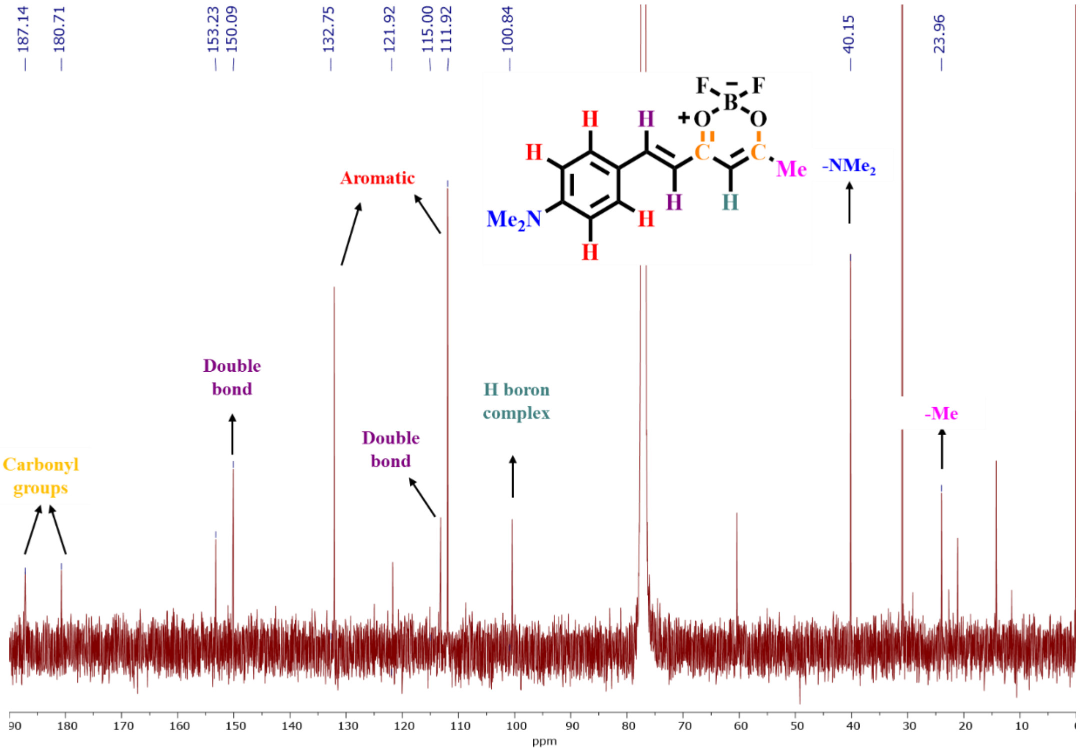

Figure 22: ^{13}C NMR spectrum and assignments for derivative **2b**.

3.1.2. Synthesis of derivatives 3a-f and 4, and NMR characterization

The initial strategy for the synthesis of derivatives **3a-f** was to isolate derivatives **2** and perform a condensation with a different aldehyde to synthesize asymmetrical curcuminoids. However, the synthesis of curcuminoids **2** did not go as expected, and this route was abandoned. An alternative strategy was implemented, using 1 equivalent of two different aldehydes to obtain the asymmetrical derivatives.

Table 3 represents all the experimental conditions tested for the synthesis of derivatives **3**. The initial experimental conditions for the synthesis of derivatives **3** were based on the synthesis described by Liu[84] and correspond to 1 equivalent of acetylacetone, 1.5 equivalent of $BF_3\cdot OEt_2$, 2 equivalent of the corresponding benzaldehyde or 1 equivalent of each corresponding benzaldehyde, 2 equivalent of $B(OEt)_3$ and 0.2 equivalent of base in toluene.

Table 3: Experimental reaction conditions for the synthesis of derivatives **3**.

Entry	**R^1**	**R^2**	**Δ (ºC)**	**Time**	**Solvent (mL)**	**Base**	**Yield (%)**	**Ref**
1[a]	-Br	-Br	100	overnight	2	---	0	87
2	-H	Benzophenone	65	6h	2	$nBuNH_2$	0	84
3[b]	-H	Benzophenone	reflux	21h30	2	Et_2NH	0	---
4[c]	-OMe	Benzophenone	65	5h	10	$nBuNH_2$	0	84
5[d]	-Br	-Br	65	2h	2	$nBuNH_2$	13	84
6	-Br	-Br	65	6h	2	$nBuNH_2$	66	84
7	-OMe	-OMe	65	20h	2	$nBuNH_2$	45	84
8	-OMe	-Br	65	16h	7	$nBuNH_2$	11	84
9[e]	$-NMe_2$	$-NMe_2$	100	17h	5	Et_2NH	27	---
10	$-NMe_2$	$- NMe_2$	65	21h	2	$nBuNH_2$	28	84
11	-Br	$- NMe_2$	65	1h	3	$nBuNH_2$	2	84
12	-OMe	$- NMe_2$	65	1h30m	4	$nBuNH_2$	9	84
13	-2,4-Cl	-2,4-Cl	65	21h	4	$nBuNH_2$	0	84
14	-Cl	-Cl	65	21h	4	$nBuNH_2$	0	84
15	-Br	-Cl	65	20h	4	$nBuNH_2$	0	84

[a] 1 equivalent of derivative **1** was used without $B(OEt)_3$ and base, the solvent used was acetic anhydride.

[b] 4 equivalent of base were used.

[c] 1 equivalent of derivative **2a**.

[d] 1 equivalent of aldehyde was used.

[e] 2 equivalent of base.

The preferred synthetic pathway, resulting in higher yields, uses 0.2 equivalent of $nBuNH_2$ as the base and 2 mL of toluene as solvent, as described by Liu and co-workers.[84]

The difference between our route and the one described by Liu group[84] is the dehydrating agent, where we use triethyl borate instead of tributyl borate. Therefore, they described yields of 95% for this reaction while our highest yield was 66% for derivative 3**a** and this synthetic route does not seem to be the most adequate. As for derivatives **2**, several aldehydes were used to attempt derivatives **3** and these include -Br, -H, -OMe, -2,4-Cl, -Cl, and -NMe_2 as R substituents, and also benzophenone. However, only symmetrical derivatives of -Br (**3a**), -OMe (**3b**), and -NMe_2 (**3c**), and asymmetrical derivatives with -OMe and -Br (**3d**), -Br and NMe_2 (**3e**), and -OMe and NMe_2 (**3f**) were obtained, with yields between 2% and 66%. In derivatives **2** it was denoted that the benzaldehydes with electron-donating groups as R substituent seems to have more ability to react and form the desired product. Purification procedures of derivatives **3e** and **3f** were complex due to their low solubility in solvents as acetone, DCM and EtOAc and the presence of a sub-product, the symmetrical derivative of -NMe_2 (**3c**). The polarity of derivatives **3e** and **3f** are very similar to derivative **3c** and purification by thin layer chromatography was very difficult. Several purification steps were necessary, resulting in compounds losses and a decrease of isolated yield.

For the synthesis of derivative **4**, as described in section 2.2.2.i, the curcumin was subjected to a reaction with the boron reagent $BF_3 \cdot OEt_2$ (scheme 8).

All obtained derivatives were characterized by NMR spectroscopy (^{1}H, ^{13}C, ^{19}F, COSY, HSQC, and HMBC) and a description of an example for each class of derivative is described below.

NMR spectroscopy for symmetrical derivative 3

Herein the assignment of the peaks for derivative **3b** will be presented**,** as an example to explain the assignments in these derivatives.

The NMR spectra for derivative **3b** are similar to the NMR spectra of **2b**. Figure 23 represents the ^{1}H NMR spectrum for derivative **3b**. The characteristic peak of the proton of the boron complex is present as a singlet at 6.01 ppm integrating for 1 proton, while the double bonds are present at 8.00 ppm and 6.58 ppm (J= 15.5 Hz) each one integrating for 2 protons, indicating that the reaction occurred on both sides of the acetylacetone.

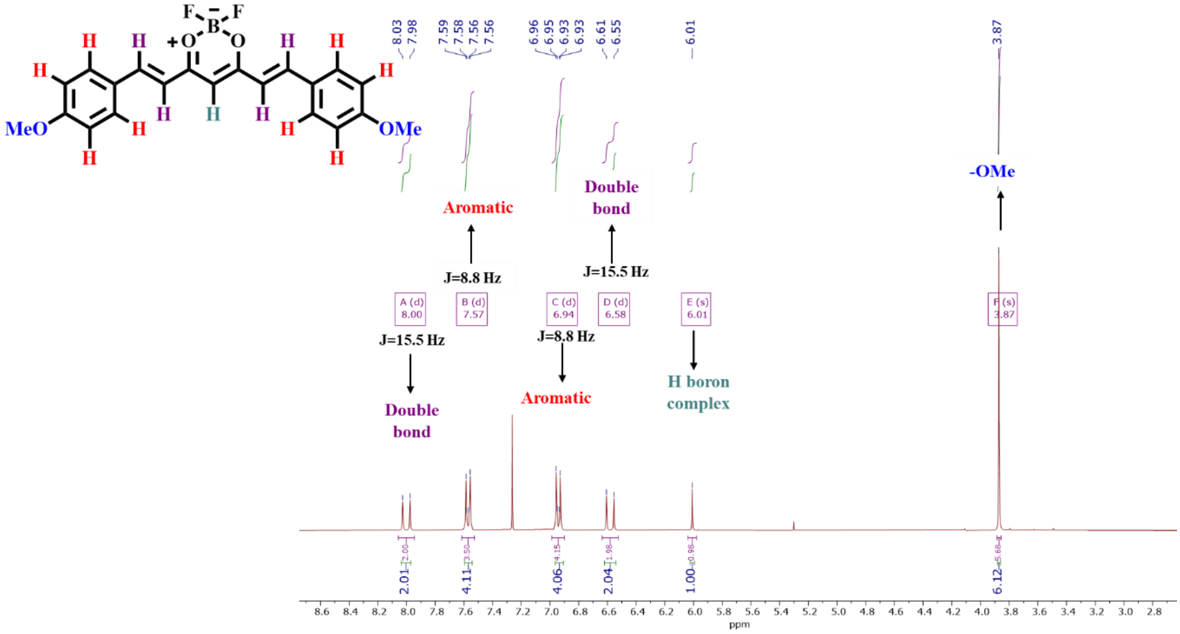

Figure 23: ^{1}H NMR spectrum and assignments for derivative **3b**.

In the COSY NMR spectrum (figure 24), we can see that the aromatic protons only couple with each other, and the protons from the double bond also couple with each other, as in derivatives **2**.

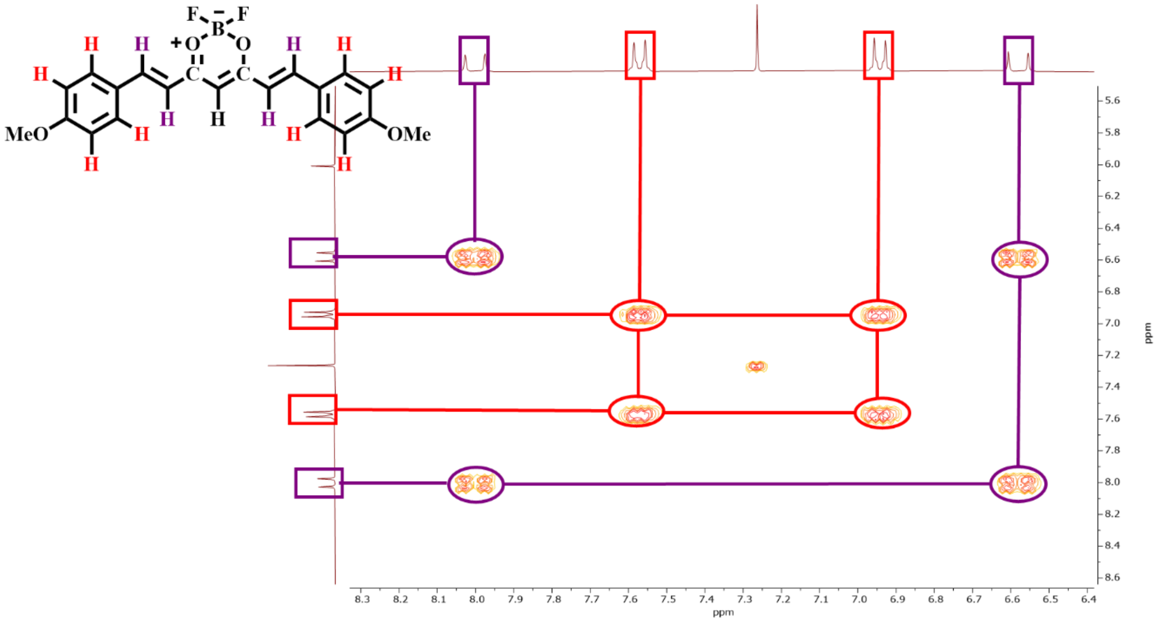

Figure 24: COSY NMR spectrum and assignments for derivative **3b**.

Figure 25 represents the ^{19}F NMR spectrum and two peaks can be seen, corresponding to the equivalent fluor atoms present in the molecule, linked to the two different isotopes of Boron, ^{10}B (20%) and ^{11}B (80%).

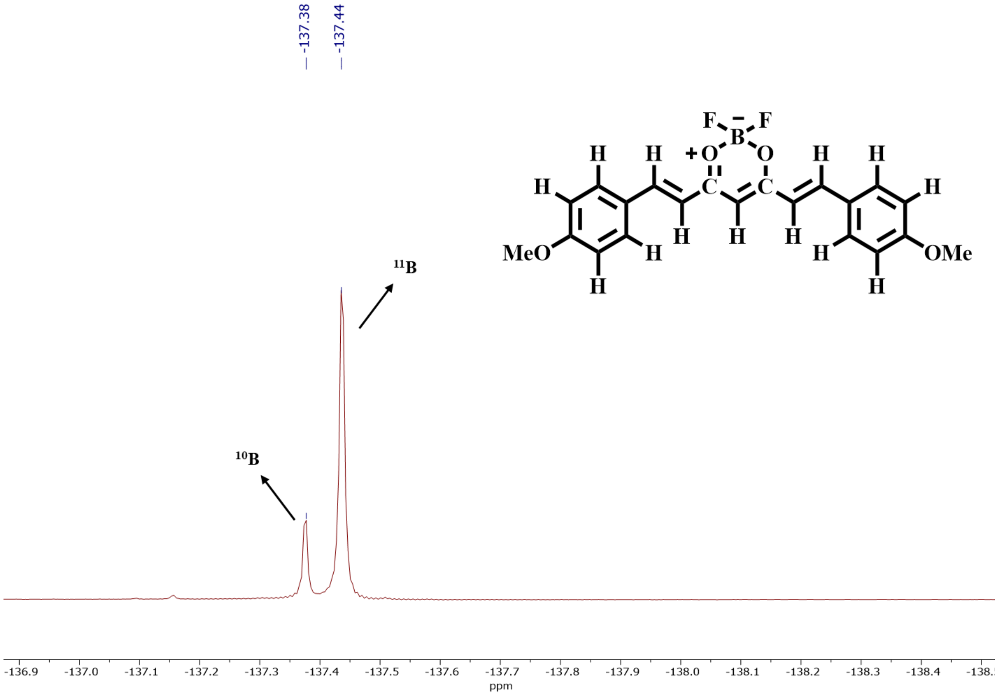

Figure 25: ^{19}F NMR spectrum and assignments for derivative **3b**.

As in derivatives **2** before the analysis of the ^{13}C NMR spectrum (figure 28), it is useful to analyze the bidimensional spectra HSQC (figure 26) and HMBC (figure 27). Analyzing the HSQC spectrum, it is possible to attribute the correlations at 1 bond between carbons and protons. That way, by observation of figure 25, it is possible to attribute the carbon peak at 55.55 ppm to the carbon of the methoxy group and the carbon peak at 102.06 ppm to the carbon of the boron complex.

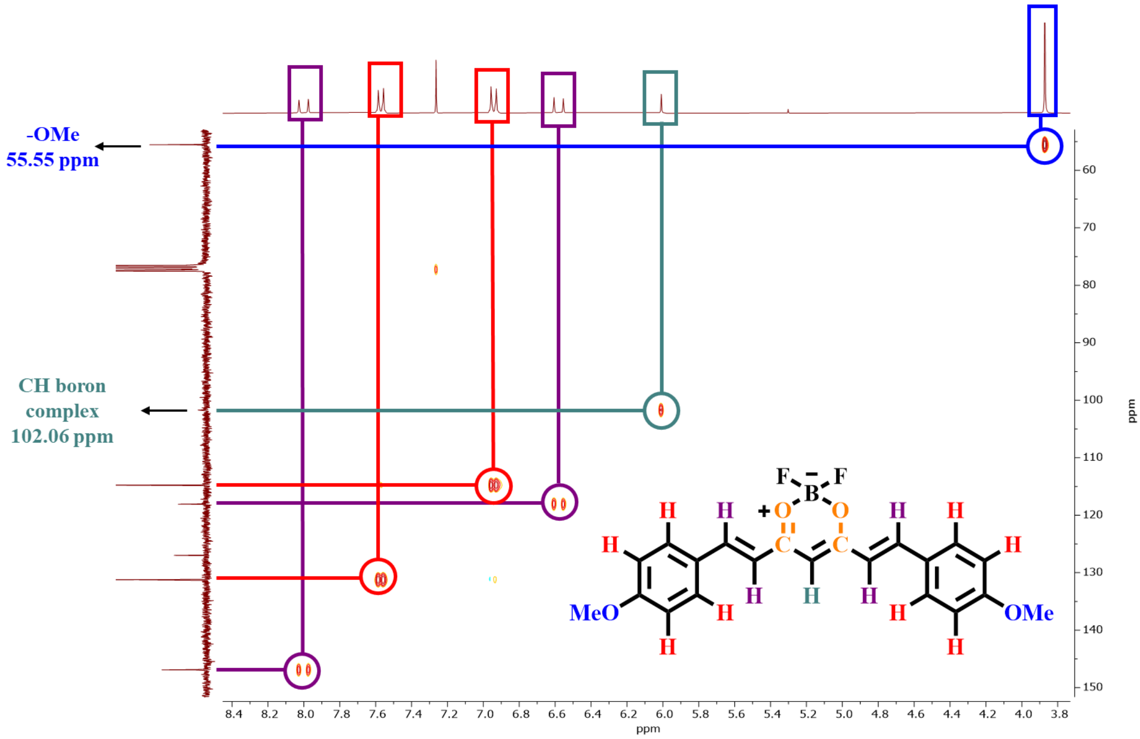

Figure 26: HSQC NMR spectrum and assignments for derivative **3b**.

Analyzing the HMBC spectrum (figure 27), it is possible to see that the proton of the boron complex only correlates with one carbon peak at 179.48 ppm, which also correlates with the two double bonds. That way, it is possible to conclude that the carbon peak at 179.48 ppm corresponds to the carbonyl groups. There is only one peak for the two carbonyl groups because, as a symmetrical molecule, the two groups are equivalent. Analyzing the spectrum, it is possible to observe that the carbon peak at 162.80 ppm correlates with both peaks of the aromatic hydrogens and with the peak of the methoxy group. That way, it is possible to conclude that the peak at 162.80 ppm belongs to the carbon that has the methoxy group as a substituent.

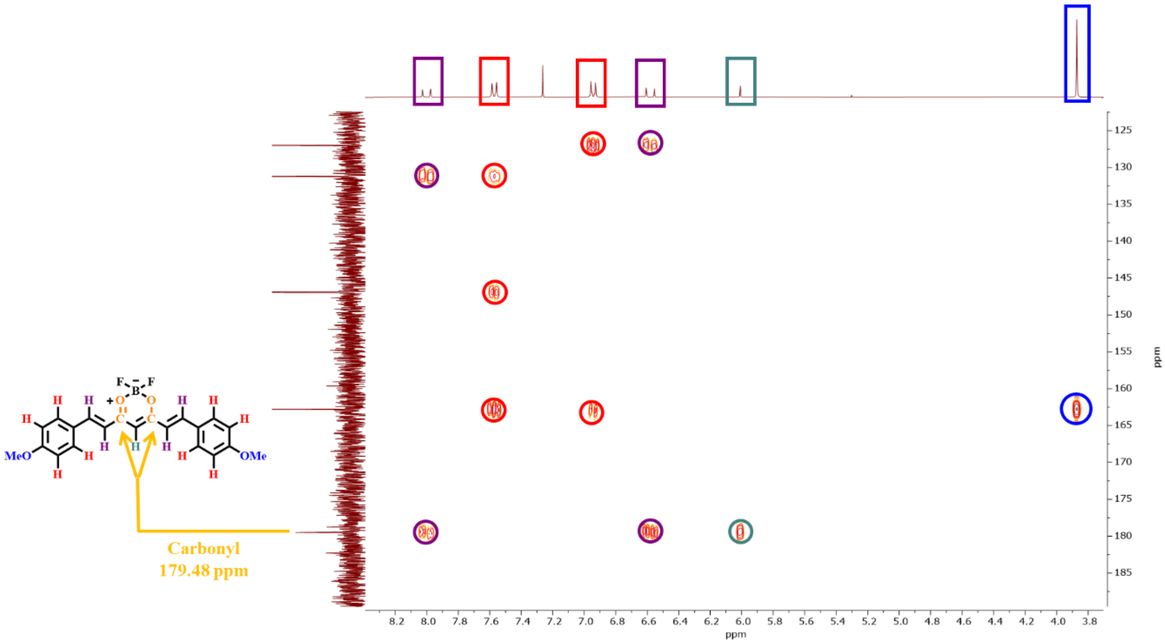

Figure 27: HMBC NMR spectrum and assignments for derivative **3b**.

Finally, it is possible to attribute the carbon peaks in the ^{13}C NMR spectrum to the correspondent protons in the molecule.

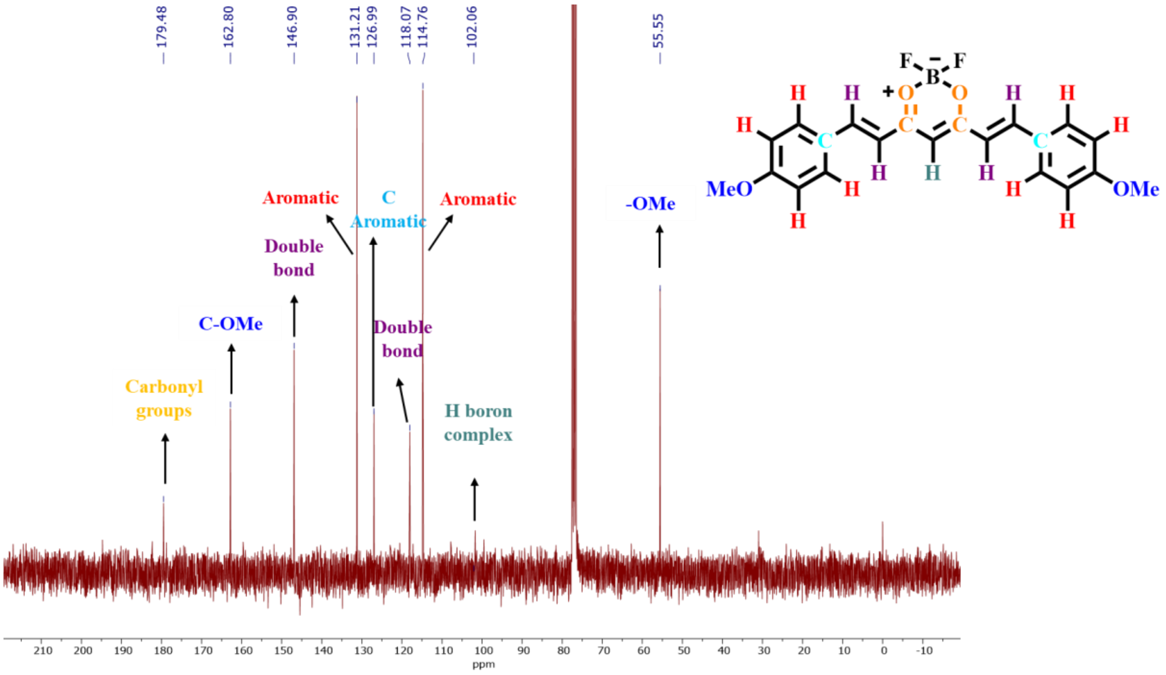

Figure 28: ^{13}C NMR spectrum and assignments for derivative **3b**.

NMR spectroscopy for asymmetrical derivative 3

Herein the assignment of the peaks for derivative **3f** will be presented as an example to explain the assignments in these derivatives.

The NMR spectra for derivative **3f** have a similar interpretation to the NMR spectra of **3b**, however, there are some differences due to the asymmetry of the molecule **3f**. Figure 29 represents the ^{1}H NMR spectrum for derivative **3f**. The characteristic peak of the -H of the boron complex is present as a singlet at 5.94 ppm integrating for 1 proton, while the double bonds are split in four peaks present at 8.03 ppm and 6.47 ppm (J= 15.2 Hz) and at 7.94 ppm and 6.56 ppm (J= 15.5 Hz), each one integrating for 1 proton. The presence of 4 protons in the double bonds indicates that the reaction occurred on both sides of the acetylacetone.

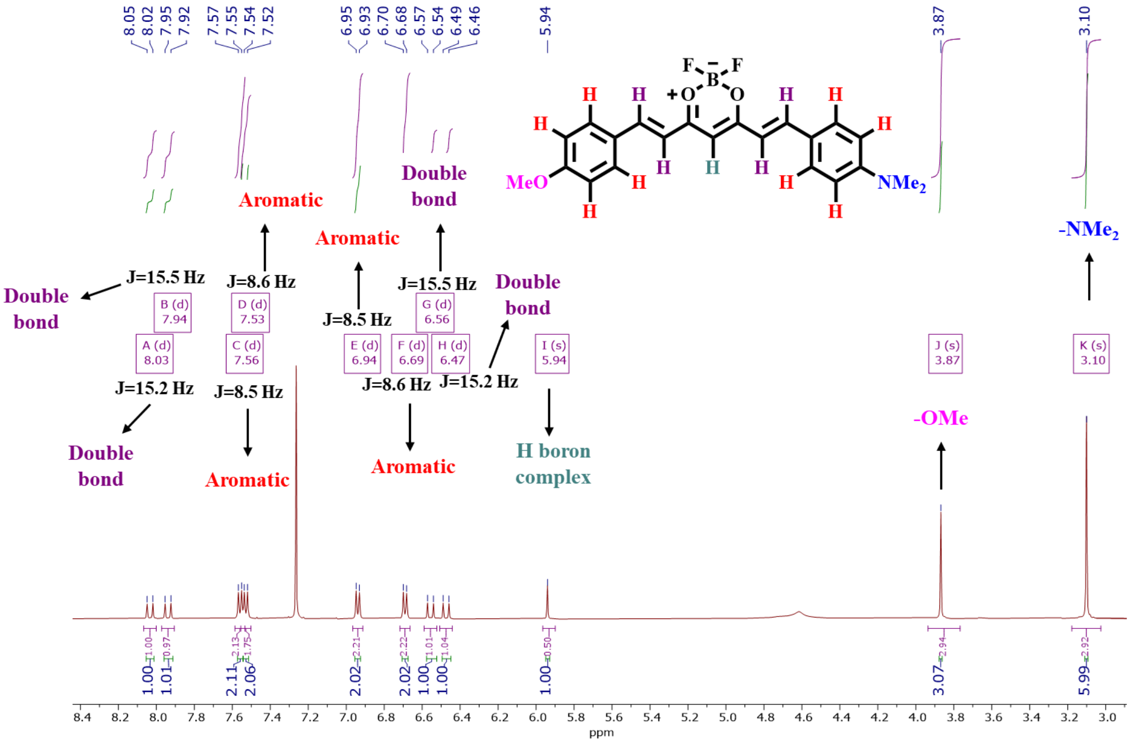

Figure 29: ^{1}H NMR spectrum and assignments for derivative **3f**

In the COSY NMR spectrum (figure 30) we can see that the aromatic protons only couple with each other and the protons from the double bond also couple with each other, as in derivatives **2** and **3b**.

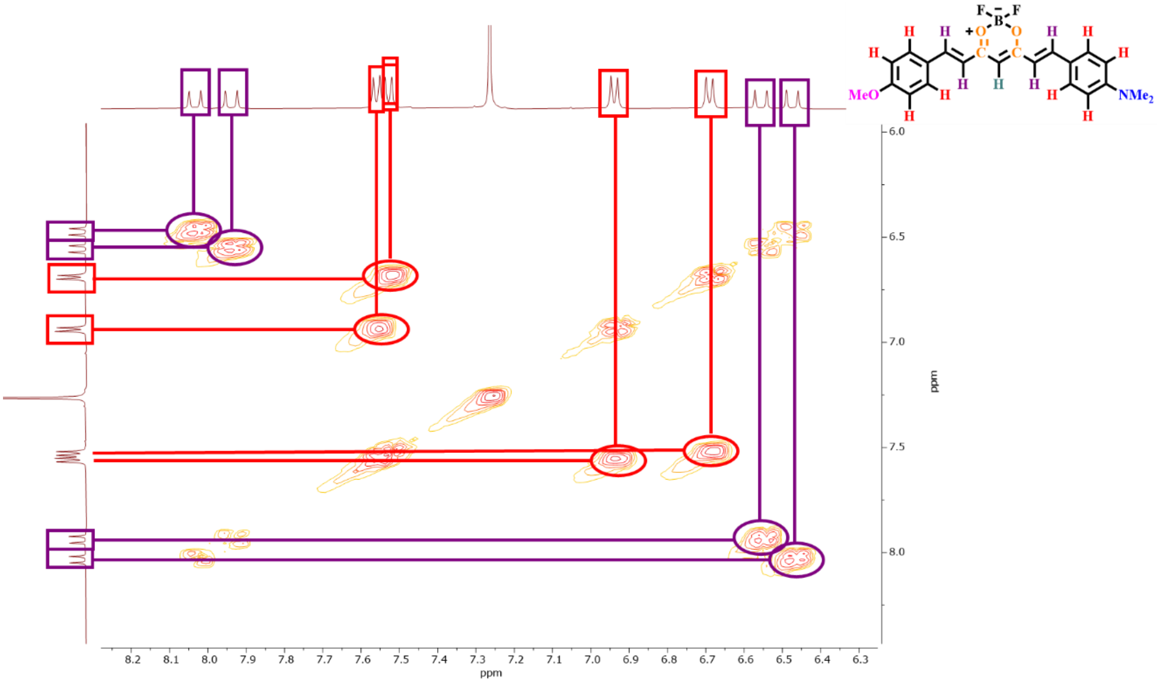

Figure 30: COSY NMR spectrum and assignments for derivative **3f**.

Figure 31 represents the ^{19}F NMR spectrum and two peaks can be seen, corresponding to the equivalent fluor atoms present in the molecule linked to the two different isotopes of Boron, ^{10}B (20%) and ^{11}B (80%), as expected.

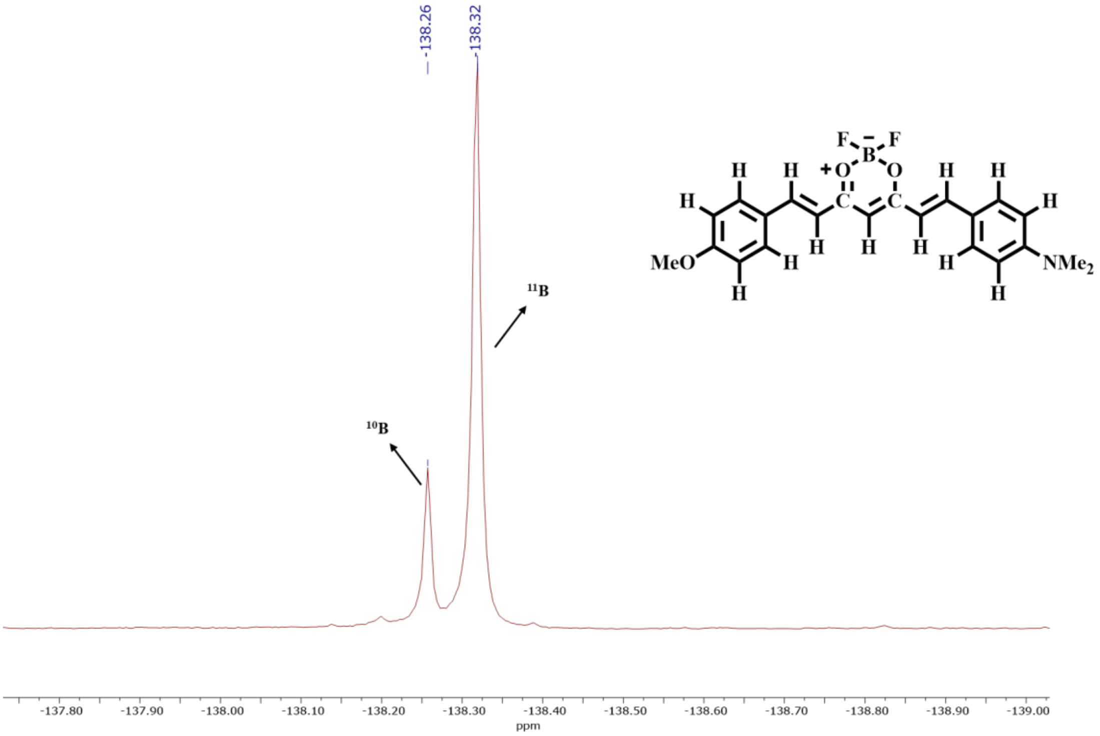

Figure 31: ^{19}F NMR spectrum and assignments for derivative **3f**.

As in derivatives previously described, before the analysis of the ^{13}C NMR spectrum (figure 34) it is useful to analyze the bidimensional spectra HSQC (figure 32) and HMBC (figure 33). Analyzing the HSQC spectrum, it is possible to attribute the correlations at 1 bond between carbons and protons. That way, by observation of figure 31, it is possible to attribute the carbon peak at 40.15 ppm to the carbon of the N,N-dimethylamino group, the carbon peak at 55.51 ppm to the carbon of the methoxy group and the carbon peak at 101.38 ppm to the carbon of the boron complex.

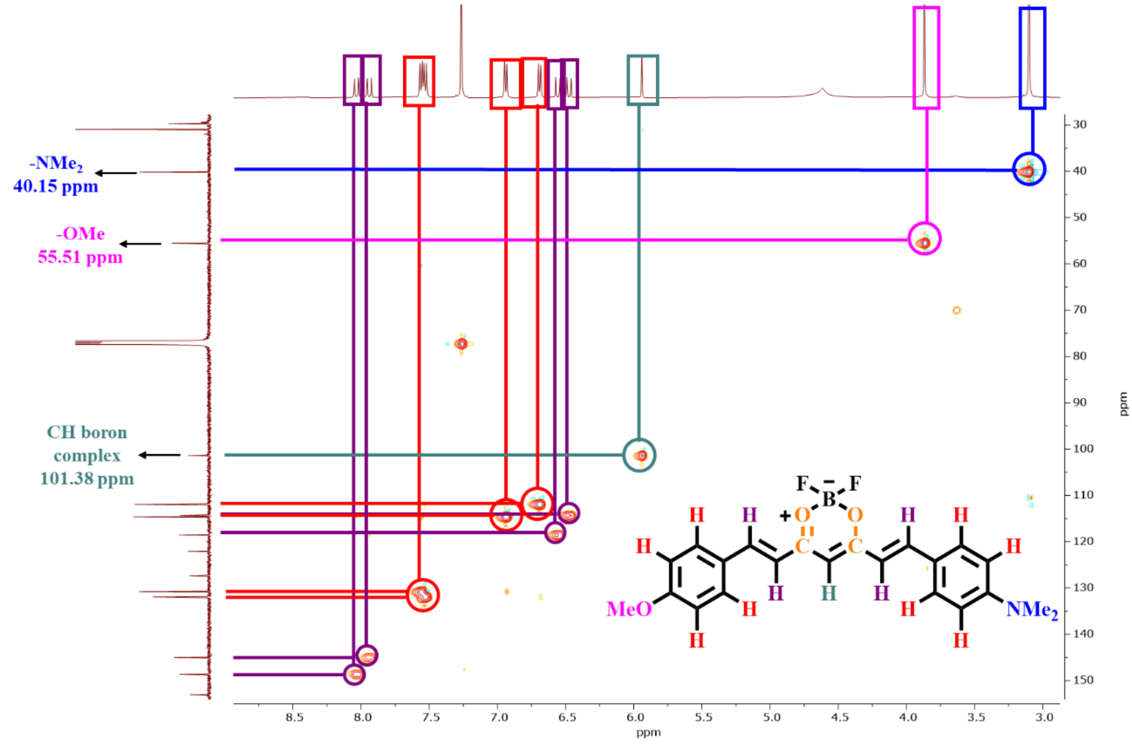

Figure 32: HSQC NMR spectrum and assignments for derivative **3f**.

Analyzing the HMBC spectrum (figure 33), it is possible to see that the proton of the boron complex correlates with two carbon peaks at 177.16 ppm and 179.65 ppm, which also are correlated with the four double bonds. It is also possible to see that the N,N-dimethylamino group indirectly correlates with the same proton doublet from one double bond that correlates with the carbonyl peak at 179.65 ppm (see figure 33, dashed blue line). The same happens with the methoxy group with the carbonyl peak at 177.16 ppm (see figure 33, dashed yellow line). In contrast to derivative **3b,** there are two peaks for the carbonyl groups because, as an asymmetrical molecule, the two groups are not equivalent.

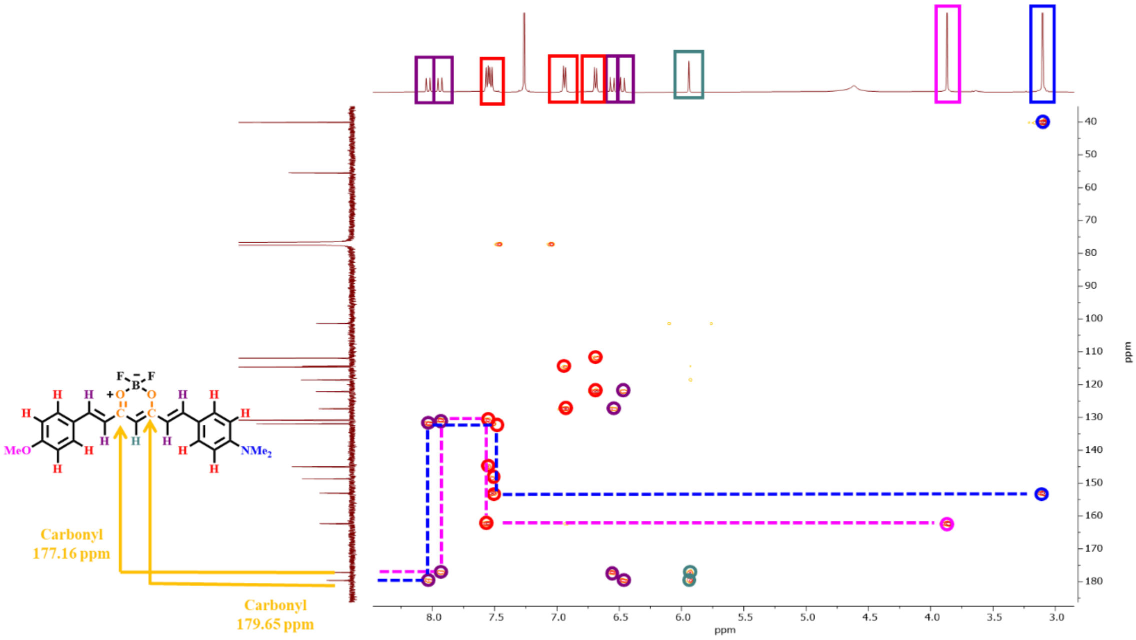

Figure 33: HMBC NMR spectrum and assignments for derivative **3f**.

Finally, it is possible to attribute the carbon peaks in the ^{13}C NMR spectrum to the correspondent protons in the molecule.

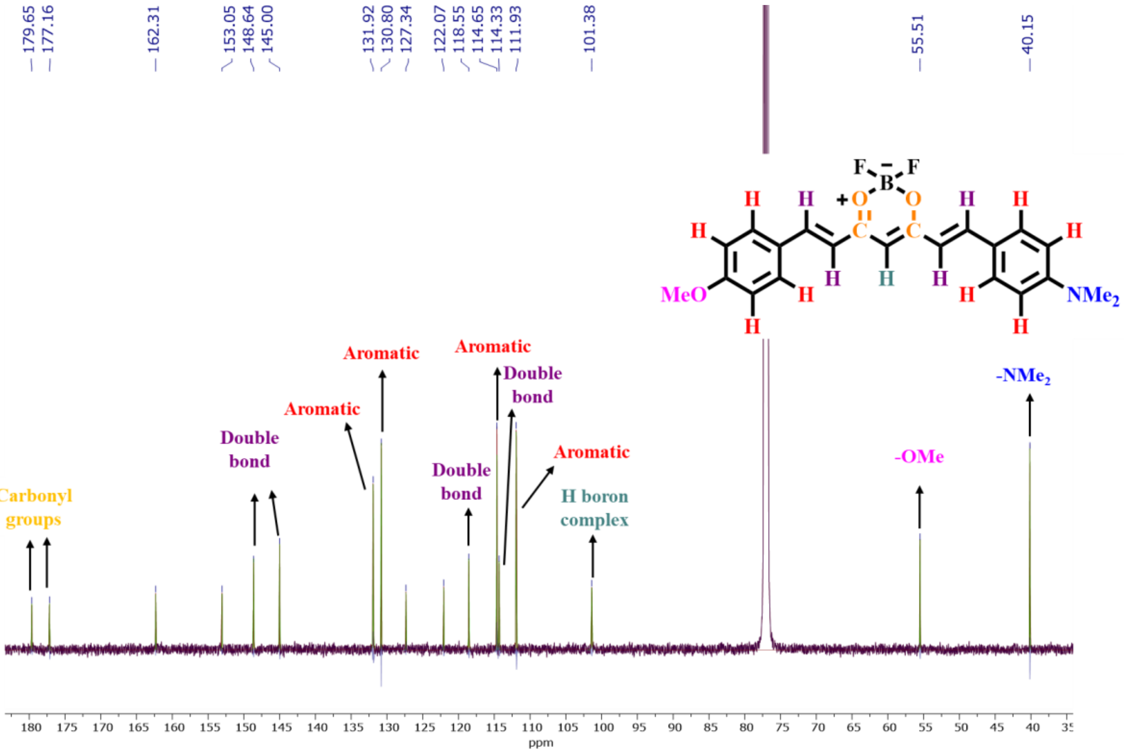

Figure 34: ^{13}C NMR spectrum and assignments for derivative **3f**.

Crystal structures

Slow evaporation of a saturated solution of derivative **3b** in THF resulted in the formation of two different needle-shaped crystals: a purple and an orange. The single crystal X-Ray diffraction of each crystal was performed and the asymmetric unit and the unit cell of purple and orange crystals are represented in figures 35 and 37, respectively.

Through the results obtained by the X-Ray diffraction (figure 35) of the purple crystal, it was possible to conclude that **3b** crystallized with a disordered solvent molecule (THF) and that it presents a planar conformation.

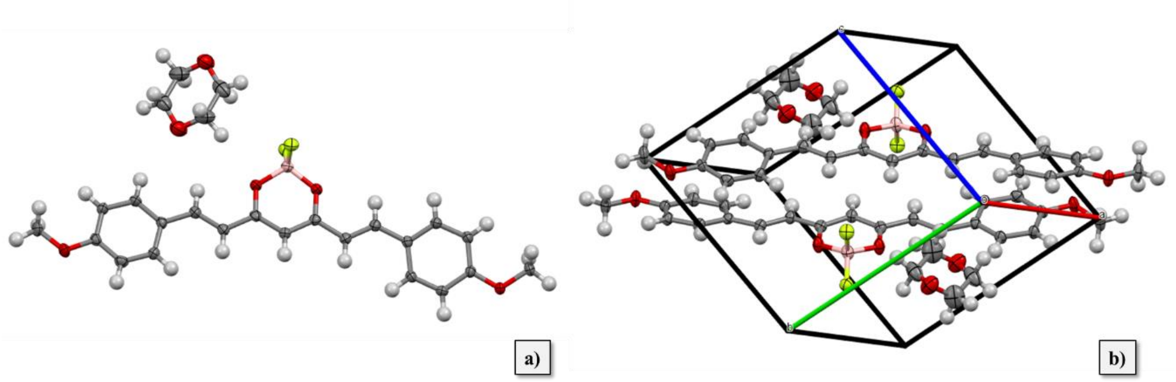

Figure 35: Molecular structure of compound **3b** (a) and unit cell content (b). Thermal ellipsoids are shown at 50% probability level, hydrogen atoms are shown with an arbitrary radius (0.30Å). C, grey: O, red; B, pink; F, yellow; H, white.

The distances between the atoms are represented in figure 36 and with this information, it is possible to confirm the structure of **3b** direct localization of the double bonds (C=C distance of 1.32 Å for both)[114] and the equivalence between both carbonyl atoms (intermediate C=O/C–O distance of 1.29 Å for both).[114] The distance between two carbon atoms in a double bond with the *E* configuration is described by having a bond length of 1.3 Å.[114] Concerning the central ring where the boron complex is present, is possible to observe that there is an electron delocalization inside the ring. This is justified by the intermediate bond lengths between a single and a double bond in the carbon-oxygen (distance of 1.29 Å) and the carbon-carbon bonds (distance of 1.36 Å). These results are coherent with the NMR spectra.

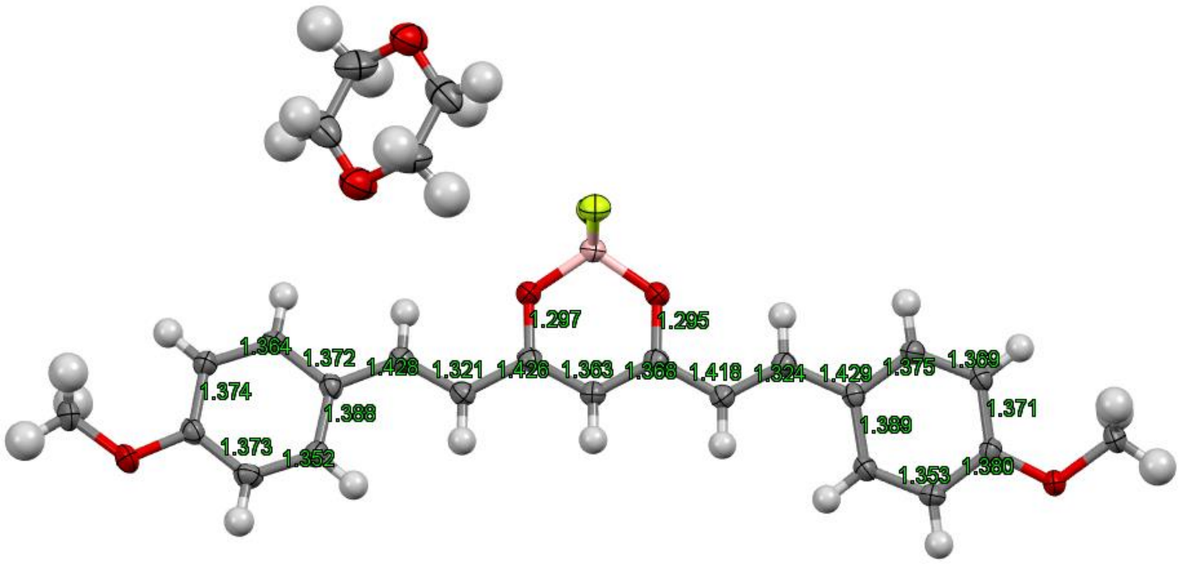

Figure 36: Distances between atoms in the molecular structure of **3b**. Thermal ellipsoids are shown at 50% probability level, hydrogen atoms are shown with an arbitrary radius (0.30Å). C, grey: O, red; B, pink; F, yellow; H, white.

Through the results obtained by the X-Ray diffraction (figure 37) of the orange crystal, it was possible to conclude that **3b** suffered hydrolysis of the BF$_2$ group, probably because of the presence of water in the THF, originating a deprotected curcuminoid from **3b**. The crystal allows verifying that the deprotected curcuminoid also presents a planar conformation.

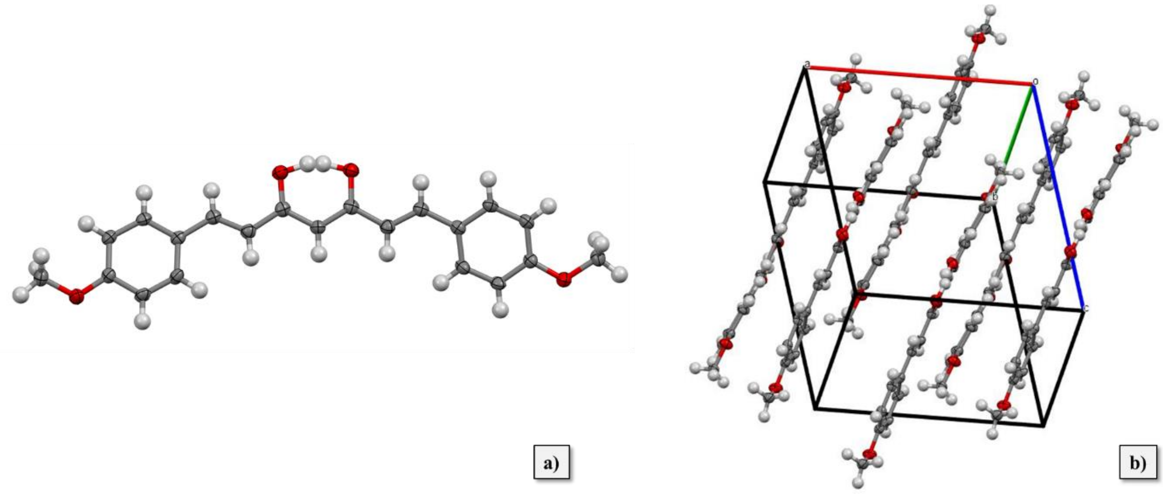

Figure 37: Molecular structure of the deprotected curcuminoid from **3b** (a) and unit cell content (b). Thermal ellipsoids are shown at 50% probability level, hydrogen atoms are shown with an arbitrary radius (0.30Å). C, grey: O, red; H, white.

As in the purple crystal of **3b**, the distances between atoms (figure 38) are coherent with the structure of the deprotected curcuminoid from **3b**. The *E* configuration double bonds (C=C distance of 1.34 Å for both)[114] and the equivalence between both carbonyl atoms (intermediate C=O/C–O distance of 1.29 Å for both) were identified. The distance of 1.39 Å, as seen in **3b**, indicates an intermediate between a single and a double bond in carbon-carbon bonds.

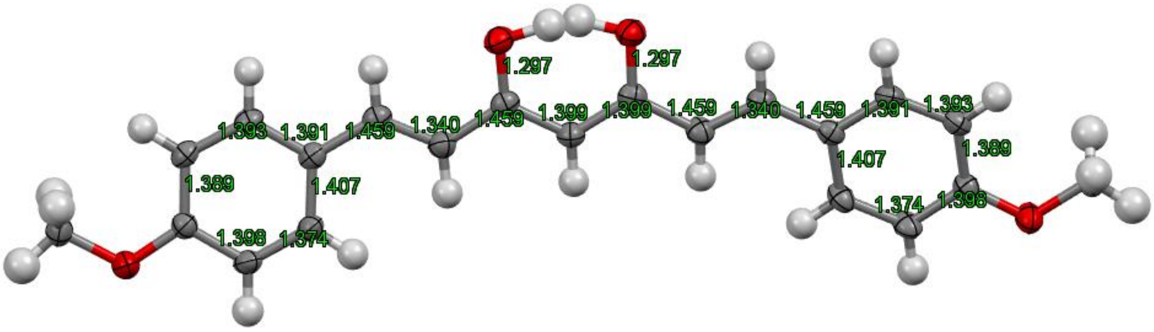

Figure 38: Distances between atoms in the molecular structure of the deprotected curcuminoid from **3b**. Thermal ellipsoids are shown at 50% probability level, hydrogen atoms are shown with an arbitrary radius (0.30Å). C, grey: O, red; H, white.

Electronic absorption and fluorescence emission properties

Absorption and emission spectra of the curcuminoid derivatives obtained were recorded in THF (figure 40 and 41, respectively), except for compound **2a** due to not having enough quantity. The absorption and emission spectra of compounds **3c** and **4** in DCM are represented in figure 39.

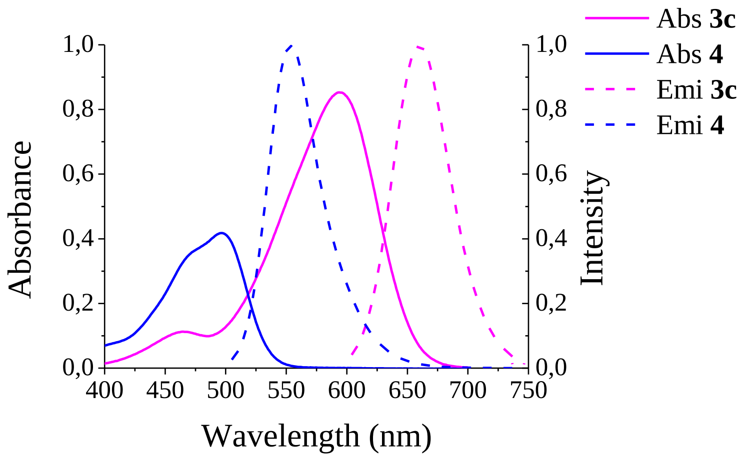

Figure 39: Absorption (at a concentration of 1 x 10^{-5} M) and emission spectra of curcumin derivatives **3c** and **4** in DCM. Excitation at 594 nm for **3c** and at 495 nm for **4**.

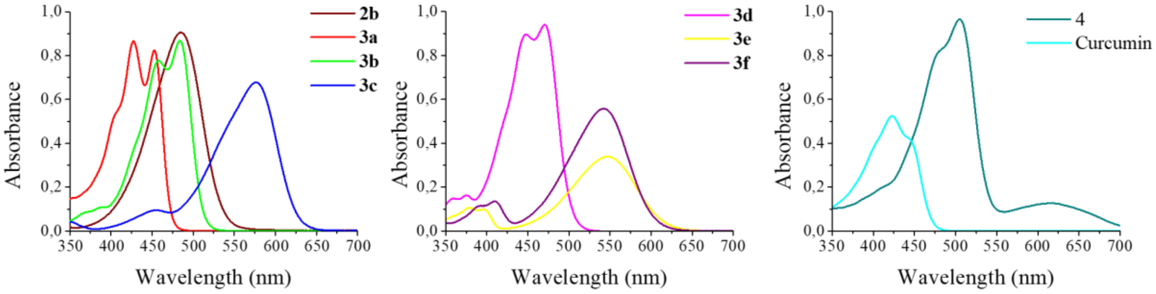

Figure 40: Absorption spectra of compounds **2b**, **3a-f**, **4** and curcumin in THF at a concentration of 1.75 x 10^{-6} M for **2b**, 3 x 10^{-5} M for **3a**, 1 x 10^{-5} M for **3b**, **3e**, **3f** and curcumin, 1.75 x 10^{-5} M for **3c**, 1.5 x 10^{-5} M for **3d** and 2.5 x 10^{-5} M for **4**.

Analyzing the absorption spectra of all derivatives, the maximum absorption wavelength varies between 423 nm and 576 nm. It is possible to denote that compounds **3** with the electron-donating groups -OMe and -NMe_2 promote a red-shift in the spectra, being the compound **3c** the one that has a longer maximum absorption wavelength. Comparing with the maximum absorption wavelength of curcumin, it is shown that the modifications made to obtain derivatives **3** and **4** induce a bathochromic shift in all absorption spectra of curcumin derivatives.

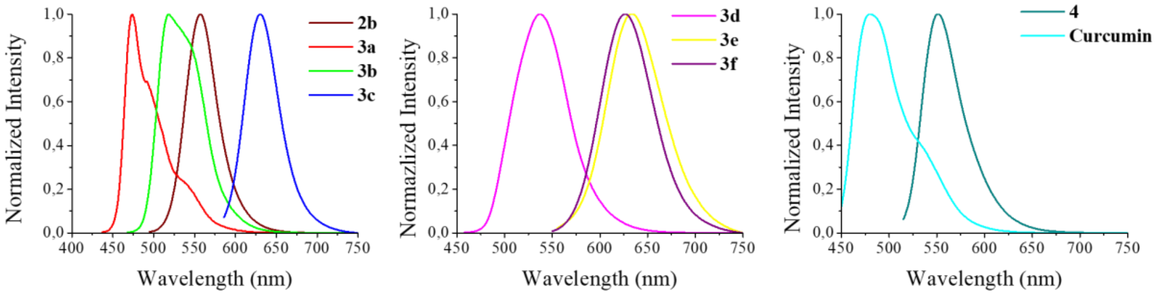

Figure 41: Normalized fluorescence spectra of compounds **2b**, **3a-f**, **4**, and curcumin recorded in THF. Excitation at 485 nm for **2b**, 427 nm for **3a**, 458 nm for **3b**, 576 nm for **3c**, 448 nm for **3d**, 545 nm for **3e**, 540 nm for **3f**, 505 nm for **4**, and 420 nm for curcumin.

A similar effect to that of the absorption spectra happens in the emission spectra. Concerning the maximum emission wavelength, these vary between 472 nm and 632 nm. As in the absorption spectra, the compounds with electron-donating groups show emission at longer wavelengths, almost in the NIR region, as intended. These bathochromic shifts in emission wavelengths could be due not only to the presence of the electron-donating groups but also due to the presence of the group BF_2. This conclusion could be demonstrated by comparing the absorption and emission spectra of curcumin and compound **4**, curcumin complexed with the BF_2 group (figures 40 and 41, respectively). Comparing both spectra it is possible to denote that **4** possess a bathochromic shift relative to curcumin, which can be caused by the insertion of the group BF_2.

The photophysical properties of obtained curcuminoids are represented in table 4: maximum absorption wavelength and maximum emission wavelength, as well as the molar absorptivity (ε), the Stokes shift ($\Delta\nu_{ST}$), the emission quantum yield (φ_f) and the brightness (ε x φ_f).

Table 4: Photophysical properties in THF of curcumin derivatives **2b**, **3a-f**, **4** and curcumin.

Fluorophore	$\lambda_{abs\ max}$ (nm)	ε ($M^{-1}cm^{-1}$)	$\Delta\nu_{ST}$ (cm^{-1})	$\lambda_{emi\ max}$ (nm)	φ_f	Brightness ($M^{-1}cm^{-1}$)
2b	485	523 000	2666	557	0.09[1]	46 000
3a	453	30 000	889	472	0.58[1]	17 400
3b	484	90 000	1319	517	0.88[1]	79 500
3c	576	40 000	1463	629	0.71[2]	29 000
3d	470	65 000	2655	537	0.69[1]	45 000
3e	546	33 000	2492	632	0.18[2]	6 000
3f	542	60 000	2476	626	0.10[2]	6 000
4	505	40 000	1619	550	0.41[1]	16 000
Curcumin	423	53 000	2764	479	0.47[1]	25 000

[1] Standard: **4**, ϕ_f = 0,58 (58%) in DCM.

[2] Standard: **3c**, ϕ_f = 0,43 (43%) in DCM.

According to the results described in table 4, the compound that has a higher molar absorptivity is compound **2b**, however it presents the lower emission quantum yield. The emission quantum yields of the compounds vary between 9% and 88%, being compound **3b** the higher. Fluorophores **3b**, **3c**, and **3e** show a marked difference in the emission quantum yields, and this difference could be explained by the presence of the electron-donating groups -OMe and -NMe_2 which increase the delocalization and changes the electronic distribution. However, the compounds **3e** and **3f** did not emit as expected since they also have electron-donating groups and show low emission quantum yields. The brightness of all compounds is similar to each other.

Figure 42 represents the distribution of the curcuminoids obtained in the electromagnetic spectra along with brightness compared with the common probes used in cell imaging.

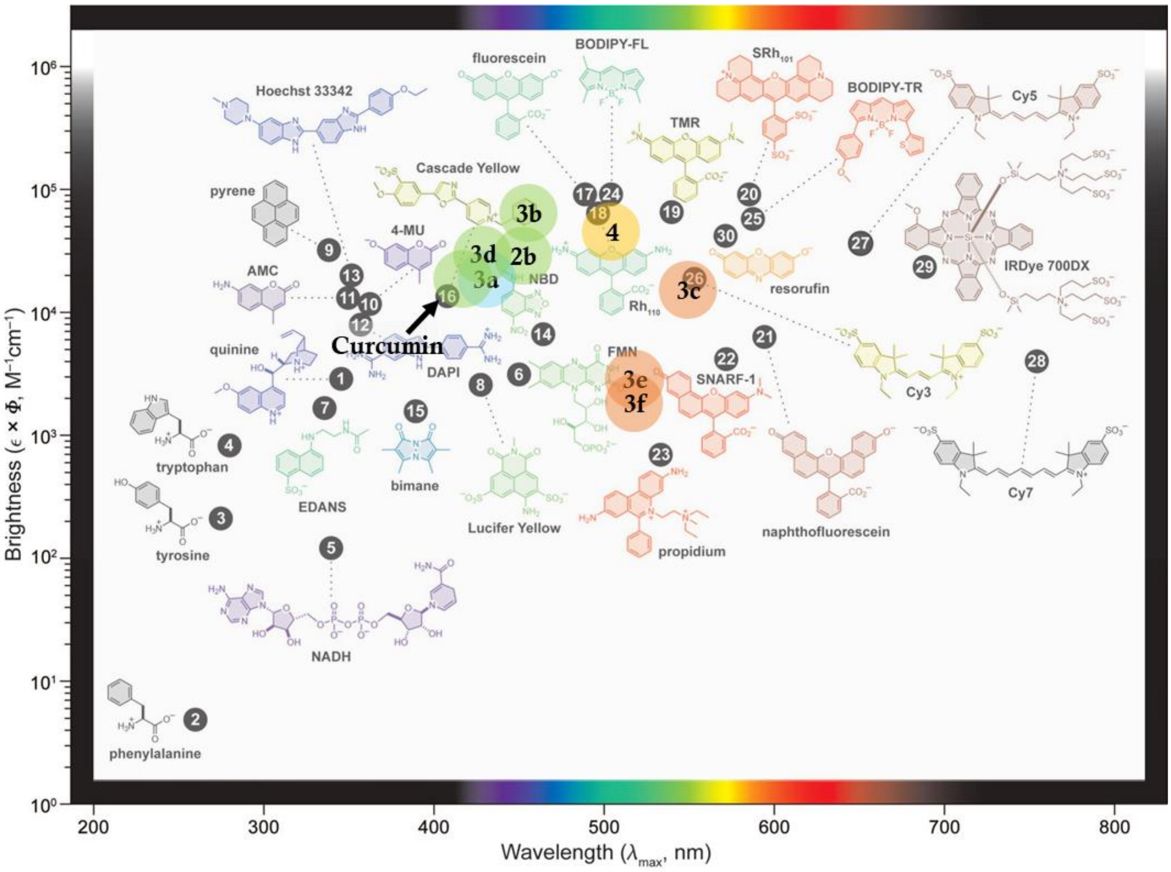

Figure 42: Fluorophore brightness *vs* absorption wavelength of the curcuminoids obtained and the most common probes used in cell imaging. The color of the compounds represents the color of the emission wavelength.[57] Adapted with permission from Lavis, L. D. & Raines, R. T. Bright Ideas for Chemical Biology. ACS Chem. Biol. 3, 142–155 (2008). Copyright 2021 American Chemical Society

Some of the curcumin derivatives synthesized present a fluorescence emission in the green region of the visible spectra (**2b**, **3b**, **3d**, and curcumin) close to the probe Nitrobenzoxadiazole (NBD) however, curcumin derivatives present a higher brightness. Despite presenting a similar maximum absorption wavelength to NBD, derivative **3a** presents smaller stokes shifts, emitting in the blue region of the visible spectra. Derivative **4** absorbs in a close wavelength to BODIPY-FL but presenting a larger stokes shift by emitting in the yellow region. The most red-shifted curcumin derivatives are **3c**, **3e**, and **3f** and are close to the emission range of resorufin and SNARF-1. That way, it is possible to verify that the synthesized curcumin derivatives possess a wide distribution over the UV-Vis spectra both in their absorption and emission wavelengths.

3.2. Cytotoxicity against *Fusarium oxysporum*

The biological evaluation of curcumin derivatives **2b**, **3**, **4** obtained, and curcumin was performed by measuring the mycelial growth over 7 days at 25 ºC (figure 43, figure 44, and figure 45). Curcumin has been shown as a potential photosensitizer for antimicrobial photodynamic therapy,[81] that way to avoid a possible photosensitization of *Fusarium oxysporum* by curcumin derivatives, their cytotoxicity was assessed in a dark environment.

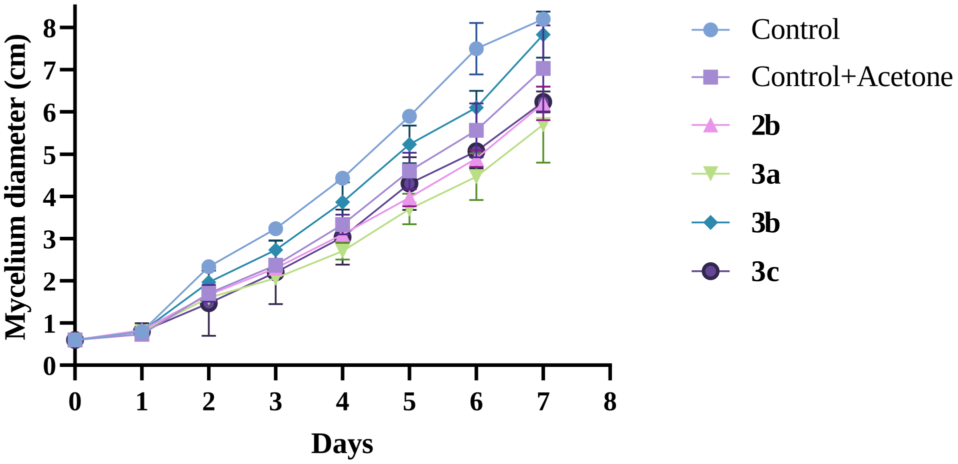

Figure 43: Mycelial growth of *Fusarium oxysporum* over 7 days in dark with the curcumin derivatives **2b**, and **3a-c** at a concentration of 100 µM. Control was performed without any derivative or acetone, and control+acetone was performed with the same volume of acetone without any derivative. The values correspond to the average of 3 replicates and the error bars correspond to the standard deviation.

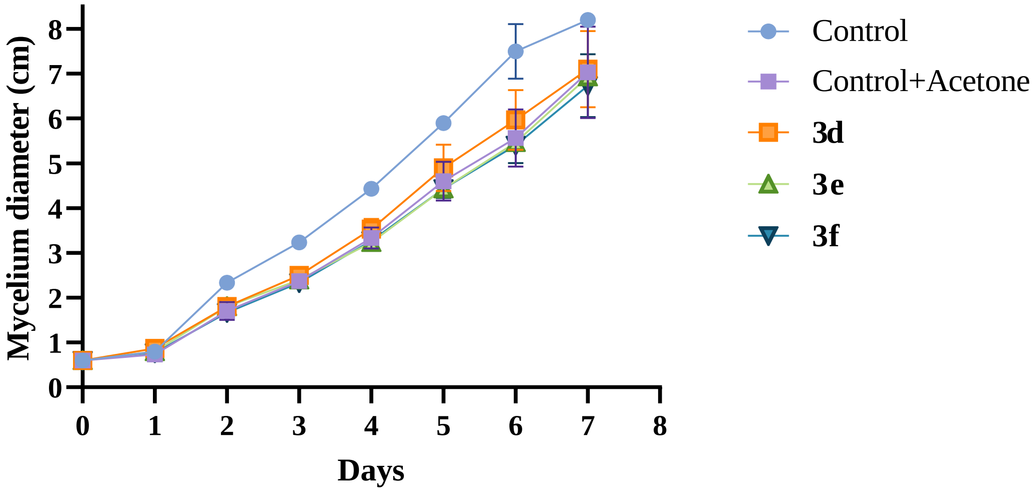

Figure 44: Mycelial growth of *Fusarium oxysporum* over 7 days in dark with the curcumin derivatives **3d-f** at a concentration of 100 µM. Control was performed without any derivative or acetone, and control+acetone was performed with the same volume of acetone without any derivative. The values correspond to the average of 3 replicates and the error bars correspond to the standard deviation.

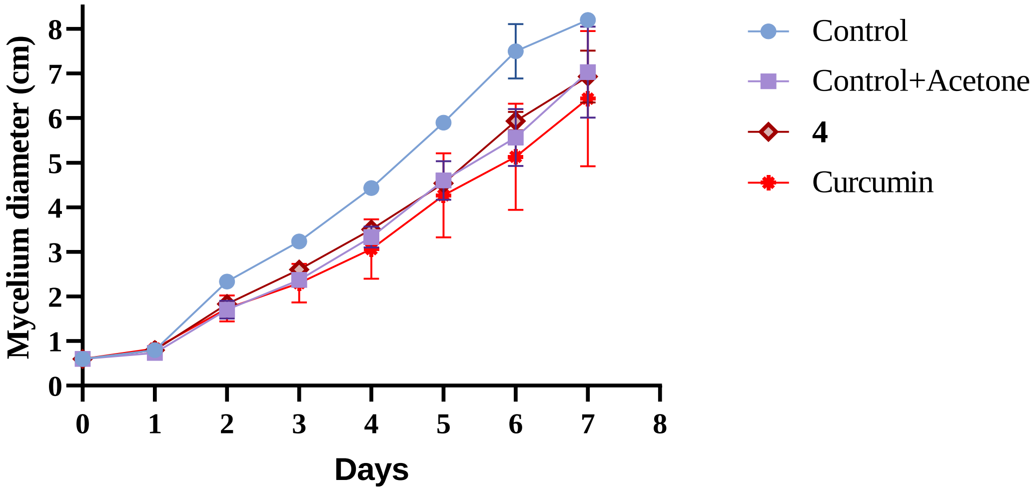

Figure 45: Mycelial growth of *Fusarium oxysporum* over 7 days in dark with the curcumin derivative **4** and curcumin at a concentration of 100 µM. Control was performed without any derivative or acetone, and control+acetone was performed with the same volume of acetone without any derivative. The values correspond to the average of 3 replicates and the error bars correspond to the standard deviation.

Incubation with curcumin derivatives **2b**, **3a-f**, **4** and curcumin, at the conditions that the assay was performed, did not inactivate the mycelial growth of *Fusarium oxysporum*. However, it is possible to observe that with derivatives **2b**, **3a-c,** and Control+Acetone the mycelial growth from the second day was always lower than the control group of plates. To understand if there are evidence of statistically significative differences at the end of the assay, statistical analysis with the method One-way ANOVA Multiple Comparisons was performed using the software Graphpad Prism 8.4.2.

Analyzing the results obtained in the statistical analysis it is possible to conclude that there are evidences that the toxicity of curcumin derivatives **2b**, **3a**, and **3c** are significantly different between each one of these and the control group (for an α=0.05 the obtained p_{values} are: 0.0266, 0.0042, 0.0300, respectively. However, it is not possible to infer if these differences are due to the presence of curcumin derivatives in the medium or if they are related to external factors, like light or contaminants. That way, for a more accurate results, it would be necessary to perform more independent assays with 3 or more replicates each and also perform independent assays under day light.

Along the 7 days of incubation, a gradual discoloration of culture media containing the curcumin derivatives **2b**, **3a-f**, and **4** was observed. The gradual discoloration along the 7 days of the plates with the curcumin derivative **3e** is represented in figure 46. Three potential explanations could rationalize this phenomenon. The first potential explanation is that, in the conditions used, the curcuminoids could suffer some degradation. The second hypothesis is that curcumin could enter into the fungal cell leaving the medium colorless. The last potential explanation is that the curcumin derivatives enter into the fungal cell and is metabolized by *Fusarium oxysporum*. Zhang, Xing and their groups showed the microbial transformation of curcumin with curcumin 4′-O-β-D-glucoside and hexahydrocurcumin as major products in the filamentous fungi *Rhizopus chinensis*.[70] That way, it is a possibility that *Fusarium oxyposrum* could metabolize curcumin derivatives giving origin to curcumin metabolites or just remain in this microorganism as curcumin.

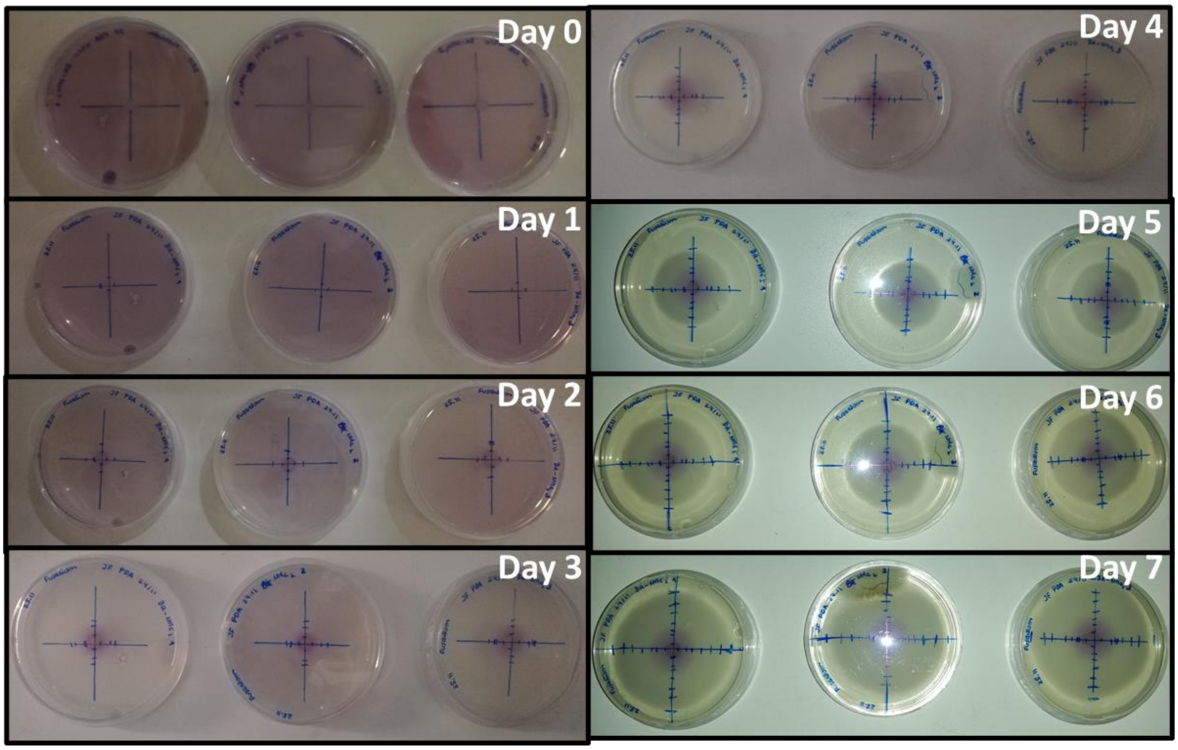

Figure 46: Mycelial growth of *Fusarium oxusporum* incubated in PDA with curcumin derivative **3e** at 25 ºC over 7 days.

Considering the results obtained, it is possible to conclude that the curcuminoids tested, in the conditions of the experiment, did not inhibit the *Fusarium oxysporum* growth so they are not considered toxic to this fungus in these conditions.

3.3. Viability in SH-SY5Y cells

The viability of curcumin derivatives **2b**, **3**, **4** obtained, and curcumin was performed by a resazurin test, and the results are represented in figure 47.

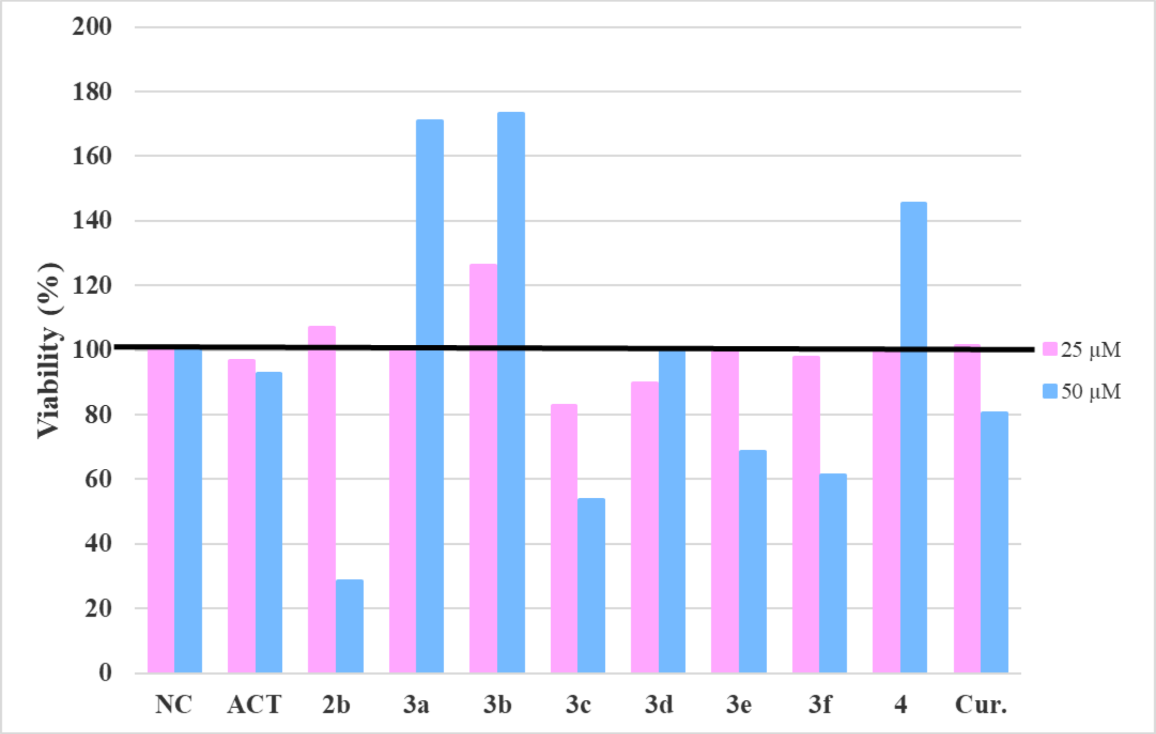

Figure 47: Cell viability assays of SH-SY5Y cells exposed to 25 and 50 uM of fluorophores 2b, 3a-f, 4, and curcumin for 3 h. NC – negative control; ACT – Control only with acetone and resazurin

The resazurin method is an indirect measure where the reduction of resazurin in resorufin by live cells is measured by its fluorescence which is always dependent on the rate of cell metabolization. In this case, to avoid the interference of compounds fluorescence, the ratio between the absorbance at 570 nm (absorption maximum of resorufin) and 600 nm (absorption maximum of resazurin)[115] was measured to evaluate the viability of the cells. However, the absorbance measurement of resorufin shows lower sensitivity than fluorescence measurement, which could explain some inconsistencies in the results obtained.[102]

Analyzing the results depicted in figure 47, it is possible to conclude that for a concentration of 25 µM, all curcuminoids present a good profile of viability being for all curcuminoids more than 80%. However, for a concentration of 50 µM the results are not so coherent. While some fluorophores present viabilities above 140% others are lower than 30%, which does not happen in a concentration of 25 µM where the results are consistent. Taking in consideration that only 1 biological replicate (with 3 technical replicates) was performed, the results are not conclusive and could be derived from an error in the observation and measurement.

Assuming that the results are without the influence of any measurement error, it is suggested that the curcuminoids, in both concentrations tests, are not toxic to the cells, in the conditions tested, with viabilities above 60% for most compounds. However, for fluorophores **2b**, **3c**, **3e**, and **3f**, the viability at a concentration of 50 μM is strongly reduced, being the decrease of more than 70% in the case of **2b**, showing some toxicity to SH-SY5Y cells which could result from some accidental exposure to light during the assay, however, whenever possible the plates were maintained under subdued light. The interference of the organic solvent acetone could be neglected so that the cell viability is above 90% for both concentrations.

3.4. Cell Imaging

3.4.1. *Fusarium oxysporum* – microscopy analyses

Brightfield visualization of *Fusarium oxysporum* was performed to identify the fungal structures of this phytopathogenic fungus, namely the type of spores present in the culture. Under brightfield microscopy, it was possible to identify the presence of the microconidia and the hyphae (figure 48). With the obtained images it was possible to identify the elliptical, oval, and kidney-shaped microconidia[116] and the hyphae structures. However, the image did not show the presence of different spores, like macroconidia and chlamydospores.

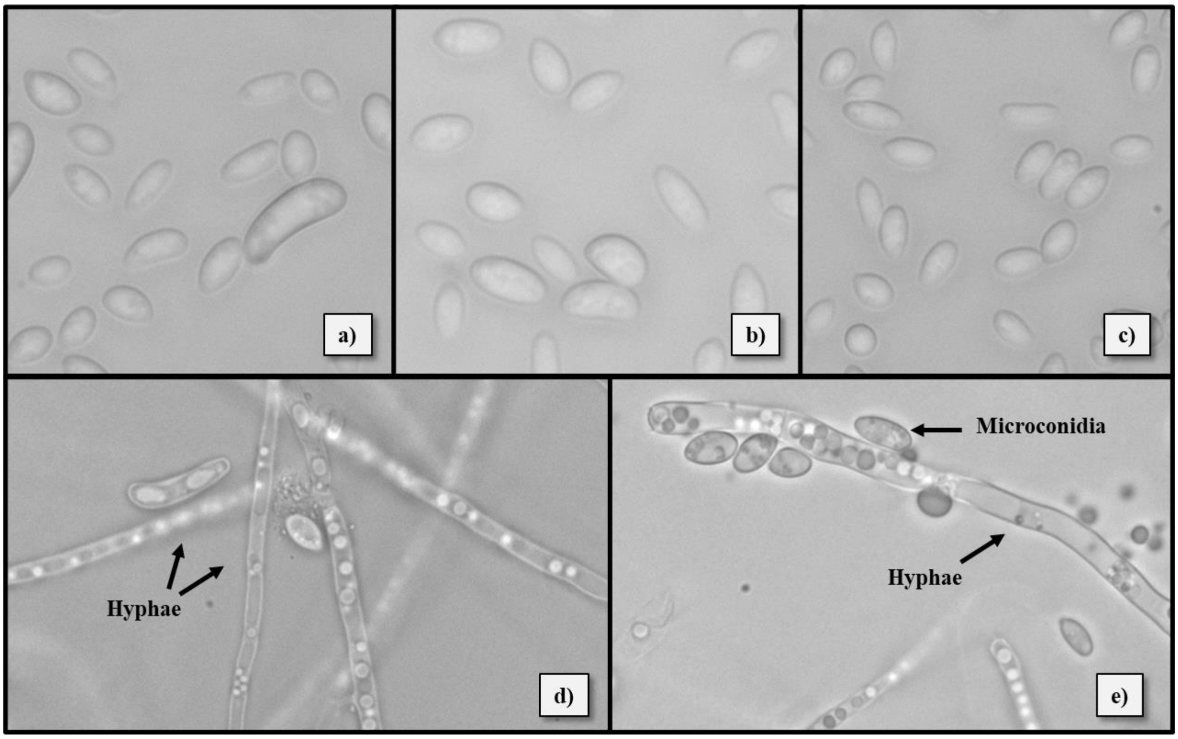

Figure 48: Brightfield microscopy of *Fusarium oxysporum*. a)-c) microconidia spores; d) hyphae; e) microconidia attached to hyphae.

Fluorescence microscopy of *Fusarium oxysporum* with the nuclear probe DAPI was included as a control for fluorescence imaging (figure 49). Fluorescence cell imaging of *Fusarium oxysporum* after incubation with DAPI allowed the visualization of the nucleus in microconidia and hyphae by the emission of a blue fluorescence when the filter A from Leica[117] was used. This filter allows the probe excitation between 340 and 380 nm and the emission detection around 425 nm. As DAPI presents a maximum absorption wavelength of 358 nm and a maximum emission wavelength of 461 nm, filter A is adequate to see the nucleus using DAPI as a probe.

In an attempt to understand the localization of curcumin derivatives obtained (**2a**, **3a-f**, **4,** and curcumin) in the fungal cell, a co-localization of derivatives with DAPI was performed. However, the available filters (A, I3 [Excitation: 450-490 nm; Emission: 515 nm] and N21 [Excitation: 515-561 nm; Emission: 590 nm] from Leica[117]) did not allow the adequate observation of curcumin derivatives since none of them has the proper excitation and emission wavelengths to use with the curcuminoids obtained. An alternative approach to view the obtained compounds is a full scan (lambda scan) of the UV-Vis and fluorescence spectra using, for example, a confocal microscope.

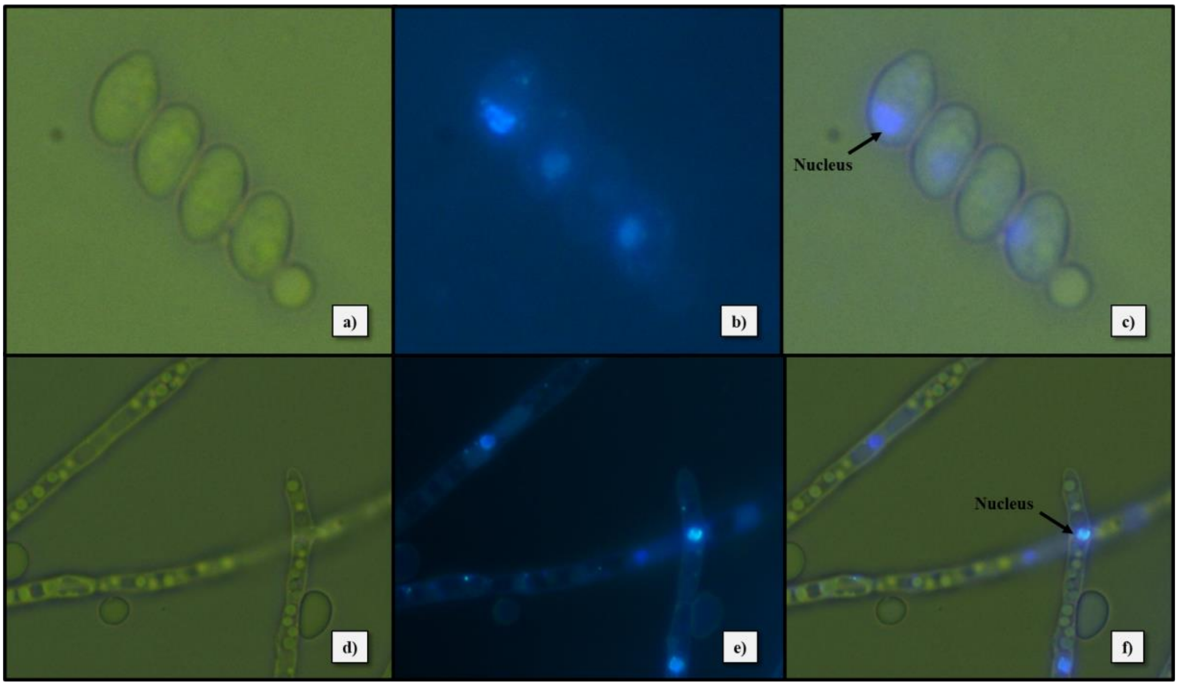

Figure 49: *Fusarium oxysporum* fluorescence imaging. a) Brightfield image of stained microconidia with DAPI, b) Fluorescence imaging of stained microconidia with DAPI, c) microconidia merged image, d) Brightfield image of stained hyphae with DAPI, e) Fluorescence imaging of stained hyphae with DAPI, f) hyphae merged image. Image processing was performed using the software Fiji ImageJ.

Fusarium oxyposrum could be considered a good cell model because it represents a fungi group that presents cellular structures more complexes, like spores with a rigid cell wall in contrast with yeasts. Hence when it is possible to stain such structure or mechanism inside this type of cells, it opens a new path to the development of compounds capable to stain more simple cells. That way, since *Fusarium oxysporum* imaging research is still scarce,[118–120] it will be interesting to develop new derivatives capable of staining specific cellular structures or certain mechanisms to apply in new treatment techniques.

3.4.2. SH-SY5Y cells – cellular staining with curcumin derivatives

Fluorescence microscopy was performed to evaluate the interaction of obtained curcuminoids with SH-SY5Y cells using three different filters to allow the excitation and visualization of compound fluorescence at the proper excitation and emission wavelengths. The filters used were the DAPI filter (Excitation: 330-385 nm; Emission: 420 nm, blue channel), GFP filter (Excitation: 450-480 nm; Emission: 515 nm, green channel), and TRITC filter (Excitation: 510-550 nm; Emission: 590 nm, red channel). As mentioned before, the choice of the filter is an important role in the visualization of a certain compound and it should be inside the fluorophores excitation and emission bands. The observations were performed at two different concentrations of curcuminoids, 25 μM and 50 μM, being 50 μM the one showing some *focis* (defined fluorescent spots) for some compounds. At a concentration of 50 μM, for compounds **2b**, **3a-c**, and **3f** it was possible to visualize fluorescence inside the cells. In case of **2b**, a small fluorescence was seen in the filters of TRITC and GFP, while for **3a** fluorescence was seen in the filters of TRITC, GFP (small) and also a very few fluorescence in DAPI lastly, in **3b** only a small fluorescence in TRITC filter was seen. However, in **3a**, **3c**, and **3f** fluorescent *focis* in cells were observed in the filter TRITC. The emission wavelengths in cells are coherent with those observed in solution. The filters used possibly are not the most adequate for the synthesized curcuminoids since they do not the curcuminoids excitation and emission maxima in their range, even though they are inside the curcuminoids excitation and emission band.

Figure 50 shows the microscopic observations for the curcuminoids **3a** (figure 49 a) and **3f** (figure 49 b) where the *focis* could be observed (black arrow).

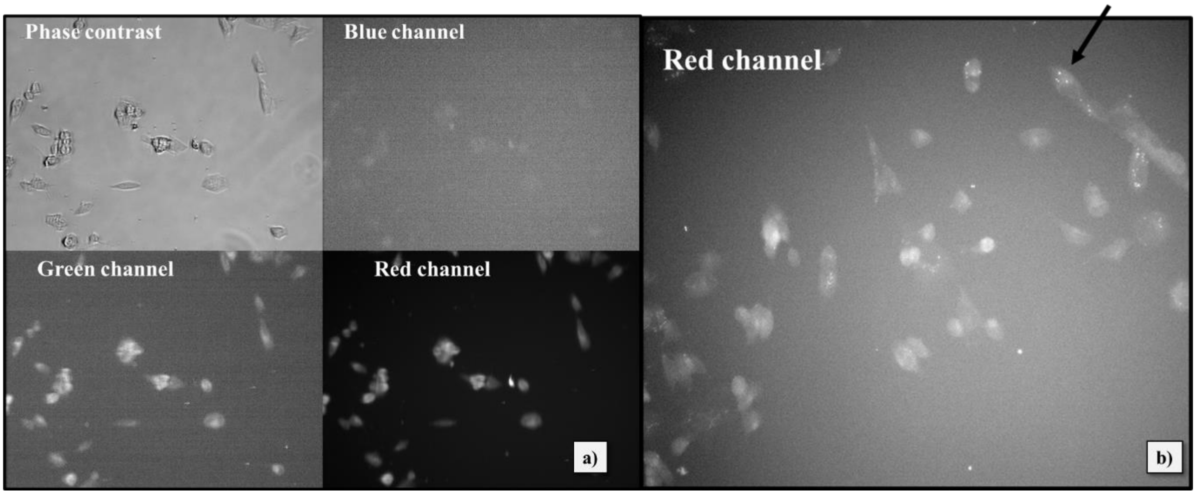

Figure 50: SH-SY5Y incubated fluorophore a) phase contrast, and blue, green, and red channels of **3a** and b) red channel of **3f** at 50 uM concentration for 3 h.

However, the fluorescence in TRITC could not be only derived from the curcuminoids since autofluorescence was observed in control cells with this filter,[121] but the presence of well-defined *focis* inside cells in this channel can indicate the presence of **3c** and **3f** in the cytoplasm. Additionally, the fact that observations were made in a medium different from the one used in fluorescence spectroscopy where fluorescence emission spectra were obtained could promote different patterns of fluorescence. The apparent localization in the cytoplasm of the curcuminoids tested are in good agreement with recent reports,[122] where four curcumin derivatives were tested as potential photosensitizers for PDT in prostate cancer cells, and the intracellular localization was studied. In their study, Kazantzis *et al.*[122] demonstrate that the four curcumin derivatives entered inside the cancer cells and were located preferentially in the cytoplasm and perinuclear region. They also prove that the curcuminoids were not localized in the mitochondria and lysosomes by the co-localization with MitoTracker and LysoTracker staining, respectively.[122] Considering this report and the promising results of localization of the curcuminoids **3a**, **3c**, and **3f** it will be interesting to examine cells incubated with these derivatives in confocal microscopy to exclude the autofluorescence of the cells and to have a more specific excitation wavelength and fluorescence emission collection, and also use cells not so differentiated, with fewer passages, since differentiation increase the cell autofluorescence.[121]

4. CHAPTER IV

CONCLUSIONS AND FUTURE PERSPECTIVES

In this study, a family of curcumin derivatives was obtained to be used in cellular imaging of two different cellular models, the phytopathogenic fungi *Fusarium oxysporum* and the human cells SH-SY5Y.

All compounds were obtained in fair yields, characterized by NMR spectroscopy and X-Ray diffraction (**3b**, and deprotected **3b**), and their photophysical properties were studied. Through the analysis of the photophysical properties, it is possible to conclude that both absorption and emission spectra are red-shifted when electron-donating groups are added and also that the BF_2 complex promotes a bathochromic shift relatively to curcumin.

Microscopic observations of the fungi *Fusarium oxysporum* and nucleus localization inside *Fusarium oxysporum* structures were performed. The effect on the growth of each curcuminoid in *Fusarium oxysporum* was tested and the results showed that in the conditions performed, there was no inhibition on growth. However, there is the need for novel independent assays to be carried out for the results to have a more statistical significance and be more conclusive.

Microscopic observations of the interaction of the curcuminoids obtained in SH-SY5Y cells were performed and promising results were obtained for **3a**, **3c**, and **3f** at a concentration of 50 μM. However, more biological replicates are needed for the results to have a more statistical significance and be more conclusive.

As future perspective it is suggested the confocal microscopy of the *Fusarium oxysporum* and SH-SY5Y cells incubated with the curcumin derivatives to overcome the problem of cells autofluorescence and to have a more specific wavelength of excitation and emission collection.

As curcumin has been demonstrated as a potential photosensitizer, it would be interesting to test the curcumin derivatives **2a**, **3a-f**, **4**, and also curcumin, performance in photodynamic inactivation in these cell models, since the research in this field using curcumin derivatives still scarce. That way, their photostability and their ability to form singlet oxygen should be tested in the first place. The localization of curcumin derivatives inside *Fusarium oxysporum* and SH-SY5Y cells should be studied to understand the type of PDI/PDT mechanism present and to develop more efficient derivatives.

5. CHAPTER V

REFERENCES

1. Valeur, B. & Berberan-Santos, M. N. *Molecular Fluorescence: Principles and Applications*, 2nd Edition. (Wiley-VCH Verlag GmbH & Co. KGaA, 2012). doi:10.1002/9783527650002.
2. Braslavsky, S. E. Glossary of terms used in photochemistry, 3rd edition (IUPAC Recommendations 2006). *Pure Appl. Chem.* **79**, 293–465 (2007).
3. Omary, M. A. & Patterson, H. H. Luminescence, Theory. in *Encyclopedia of Spectroscopy and Spectrometry*, 3rd Edition, 636–653 (Elsevier, 2017). doi:10.1016/B978-0-12-803224-4.00193-X.
4. Lakowicz, J. R. *Principles of Fluorescence Spectroscopy*, 3rd Edition (Springer US, 2006). doi:10.1007/978-0-387-46312-4.
5. Donnelly, J. & Hernandez, F. E. Two-photon absorption spectroscopy on curcumin in solution: A state-of-the-art physical chemistry experiment. *J. Chem. Educ.* **94**, 101–104 (2017). doi: 10.1021/acs.jchemed.6b00660
6. Jabłoński, A. Über den Mechanismus der Photolumineszenz von Farbstoffphosphoren. *Zeitschrift für Phys.* **94**, 38–46 (1935). doi: 10.1007/BF01330795
7. Ravotto, L. & Ceroni, P. Aggregation induced phosphorescence of metal complexes: From principles to applications. *Coord. Chem. Rev.* **346**, 62–76 (2017). doi: 10.1016/j.ccr.2017.01.006
8. Ye, C., Zhou, L., Wang, X. & Liang, Z. Photon upconversion: From two-photon absorption (TPA) to triplet-triplet annihilation (TTA). *Phys. Chem. Chem. Phys.* **18**, 10818–10835 (2016). doi: 10.1039/c5cp07296d
9. Jiang, F. L., Poon, C. T., Wong, W. K., Koon, H. K., Mak, N. K., Choi, C. Y. An amphiphilic bisporphyrin and its YbIII complex: Development of a bifunctional photodynamic therapeutic and near-infrared tumor-imaging agent. *ChemBioChem* **9**, 1034–1039 (2008). doi: 10.1002/cbic.200700767
10. Jameson, D. M. *Introduction to Fluorescence*. (CRC Press 2014).
11. Brouwer, A. M. Standards for photoluminescence quantum yield measurements in solution (IUPAC Technical Report). *Pure Appl. Chem.* **83**, 2213–2228 (2011). doi: 10.1351/PAC-REP-10-09-31

12. Cieplik, F. Deng, D., Crielaard, W., Buchalla, W. Hellwig, E. Al-Ahmad, A., Maisch, T. Antimicrobial photodynamic therapy – what we know and what we don't. *Crit. Rev. Microbiol.* **44**, 571–589 (2018). doi: 10.1080/1040841X.2018.1467876
13. Alves, E. Faustino, M. A. F. Neves, M. G. P. M. S., Cunha, A., Tome, J. Almeida, A. An insight on bacterial cellular targets of photodynamic inactivation. *Future Med. Chem.* **6**, 141–164 (2014). doi: 10.4155/fmc.13.211
14. Robertson, C. A., Evans, D. H. & Abrahamse, H. Photodynamic therapy (PDT): A short review on cellular mechanisms and cancer research applications for PDT. *J. Photochem. Photobiol. B Biol.* **96**, 1–8 (2009). doi: 10.1016/j.jphotobiol.2009.04.001
15. Lyon, J. P., Moreira, L. M., de Moraes, P. C. G., dos Santos, F. V. & de Resende, M. A. Photodynamic therapy for pathogenic fungi. *Mycoses* **54**, 265–271 (2011). doi: 10.1111/j.1439-0507.2010.01966.x
16. Abrahamse, H. & Hamblin, M. R. New photosensitizers for photodynamic therapy. *Biochem. J.* **473**, 347–364 (2016). doi: 10.1042/BJ20150942
17. Patra, D. & Barakat, C. Synchronous fluorescence spectroscopic study of solvatochromic curcumin dye. *Spectrochim. Acta - Part A Mol. Biomol. Spectrosc.* **79**, 1034–1041 (2011). doi: 10.1016/j.saa.2011.04.016
18. Vidal, M., Rezende, M. C., Pastene, C., Aliaga, C. & Domínguez, M. Solvatochromism of conjugated 4-*N*,*N*-dimethylaminophenyl-pyridinium donor–acceptor pairs. *New J. Chem.* **42**, 4223–4231 (2018). doi: 10.1039/C7NJ04992G
19. Reichardt, C. & Welton, T. Solvent Effects on the Absorption Spectra of Organic Compounds. in *Solvents and Solvent Effects in Organic Chemistry* 359–424 (Wiley-VCH Verlag GmbH & Co. KGaA, 2010). doi:10.1002/9783527632220.ch6.
20. Klymchenko, A. S. Solvatochromic and Fluorogenic Dyes as Environment-Sensitive Probes: Design and Biological Applications. *Acc. Chem. Res.* **50**, 366–375 (2017). doi: 10.1021/acs.accounts.6b00517
21. Lyu, H., Wang, D., Cai, L., Wang, D.-J. & Li, X.-M. Synthesis, photophysical and solvatochromic properties of diacetoxyboron complexes with curcumin derivatives. *Spectrochim. Acta Part A Mol. Biomol. Spectrosc.* **220**, 117126 (2019). 10.1016/j.saa.2019.05.031
22. Kucherak, O. A., Didier, P., Mèly, Y. & Klymchenko, A. S. Fluorene analogues of

prodan with superior fluorescence brightness and solvatochromism. *J. Phys. Chem. Lett.* **1**, 616–620 (2010). doi: 10.1021/jz9003685

23. Stock, R. I., Nandi, L. G., Nicoleti, C. R., Schramm, A. D. S., Meller, S. L., Heying, R. S., Coimbra, D. F., Andriani, K. F., Caramori, G. F., Bortoluzzi, A. J., Machado, V. G. Synthesis and Solvatochromism of Substituted 4-(Nitrostyryl)phenolate Dyes. *J. Org. Chem.* **80**, 7971–7983 (2015). doi: 10.1021/acs.joc.5b00983
24. Kim, E., Lee, Y., Lee, S. & Park, S. B. Discovery, Understanding, and Bioapplication of Organic Fluorophore: A Case Study with an Indolizine-Based Novel Fluorophore, Seoul-Fluor. *Acc. Chem. Res.* **48**, 538–547 (2015). doi: 10.1021/ar500370v
25. Kim, E., Koh, M., Lim, B. J. & Park, S. B. Emission wavelength prediction of a full-color-tunable fluorescent core skeleton, 9-aryl-1,2-dihydropyrrolo[3,4-b]indolizin-3-one. *J. Am. Chem. Soc.* **133**, 6642–6649 (2011). doi: 10.1021/ja110766a
26. Williams, R. T. & Bridges, J. W. Fluorescence of solutions: A review. *J. Clin. Pathol.* **17**, 371–394 (1964). doi: 10.1136/jcp.17.4.371
27. Hong, Y., Lam, J. W. Y. & Tang, B. Z. Aggregation-induced emission. *Chem. Soc. Rev.* **40**, 5361-5388 (2011). doi: 10.1039/c1cs15113d
28. Luo, J. Xie, Z., Lam, J. W. Y., Cheng, L., Tang, B. Z. Chen, H., Qiu, C., Kwok, H. S., Zhan, X., Liu, Y., Zhu, D. Aggregation-induced emission of 1-methyl-1,2,3,4,5-pentaphenylsilole. *Chem. Commun.* **381**, 1740–1741 (2001). 10.1039/b105159h
29. Leung, N. L. C., Xie, N., Yuan, W., Liu, Y., Wu, Q., Peng, Q., Miao, Q., Lam, J. W. Y., Tang, B. Z. Restriction of intramolecular motions: The general mechanism behind aggregation-induced emission. *Chem. - A Eur. J.* **20**, 15349–15353 (2014). doi: 10.1002/chem.201403811
30. La, D. D., Bhosale, S. V., Jones, L. A. & Bhosale, S. V. Tetraphenylethylene-Based AIE-Active Probes for Sensing Applications. *ACS Appl. Mater. Interfaces* **10**, 12189–12216 (2018). doi: 10.1021/acsami.7b12320
31. Chen, W. Zhang, C., Han, X., Liu, S. H., Tan, Y., Yin, J. Fluorophore-Labeling Tetraphenylethene Dyes Ranging from Visible to Near-Infrared Region: AIE Behavior, Performance in Solid State, and Bioimaging in Living Cells. *J. Org. Chem.* **84**, 14498–14507 (2019). doi: 10.1021/acs.joc.9b01976
32. Zhu, C., Kwok, R. T. K., Lam, J. W. Y. & Tang, B. Z. Aggregation-Induced

Emission: A Trailblazing Journey to the Field of Biomedicine. *ACS Appl. Bio Mater.* **1**, 1768–1786 (2018). doi: 10.1021/acsabm.8b00600

33. Hong, Y., Lam, J. W. Y. & Tang, B. Z. Aggregation-induced emission: Phenomenon, mechanism and applications. *Chem. Commun.* 4332–4353 (2009) doi:10.1039/b904665h.
34. Bhongale, C. J., Chang, C. W., Lee, C. S., Diau, E. W. G. & Hsu, C. S. Relaxation dynamics and structural characterization of organic nanoparticles with enhanced emission. *J. Phys. Chem. B* **109**, 13472–13482 (2005). doi: 10.1021/jp0502297
35. Hirano, K., Minakata, S., Komatsu, M. & Mizuguchi, J. Intense blue luminescence of 3,4,6-triphenyl-α-pyrone in the solid state and its electronic characterization. *J. Phys. Chem. A* **106**, 4868–4871 (2002). doi: 10.1021/jp013850p
36. Tang, W., Xiang, Y. & Tong, A. Salicylaldehyde Azines as Fluorophores of Aggregation-Induced Emission Enhancement Characteristics. *J. Org. Chem.* **74**, 2163–2166 (2009). doi: 10.1021/jo802631m
37. Bayda, M. Dumoulin, F., Hug, G. L., Koput, J., Gorniak, R., Wojcik, A. Fluorescent H-aggregates of an asymmetrically substituted mono-amino Zn(II) phthalocyanine. *Dalt. Trans.* **46**, 1914–1926 (2017). doi: 10.1039/C6DT02651F
38. Hestand, N. J., Spano, F. C. Expanded Theory of H- and J-Molecular Aggregates: The Effects of Vibronic Coupling and Intermolecular Charge Transfer. *Chem. Rev.* **118**, 7069–7163 (2018). doi: 10.1021/acs.chemrev.7b00581
39. Kasha, M., Rawls, H. R., El-Bayoumi, M. A. The exciton model in molecular spectroscopy. *Pure Appl. Chem.* **11**, 371–392 (1965). doi: 10.1351/pac196511030371
40. Royer, C. A. Fluorescence Spectroscopy. in *Protein Stability and Folding* vol. 40 65–90 (Humana Press, 1995). doi: 10.1385/0-89603-301-5:65
41. Wang, D. Lee, M. M. S., Shan, G., Kwok, R. T. K., Lam, J. W. Y., Su, H., Cai, Y., Tang, B. Z. Highly Efficient Photosensitizers with Far-Red/Near-Infrared Aggregation-Induced Emission for In Vitro and In Vivo Cancer Theranostics. *Adv. Mater.* **30**, 1802105 (2018). doi: 10.1002/adma.201802105
42. Sun, X. Zebibula, A., Dong, X., Li, G., Zhang, G., Zhang, D., Qian, J., He, S. Targeted and imaging-guided in vivo photodynamic therapy for tumors using dual-function, aggregation-induced emission nanoparticles. *Nano Res.* **11**, 2756–2770

(2018). doi: 10.1007/s12274-017-1906-7

43. Zhu, H., Fan, J., Du, J. Peng, X. Fluorescent Probes for Sensing and Imaging within Specific Cellular Organelles. *Acc. Chem. Res.* **49**, 2115–2126 (2016). doi: 10.1021/acs.accounts.6b00292
44. Escobedo, J. O., Rusin, O., Lim, S. Strongin, R. M. NIR dyes for bioimaging applications. *Curr. Opin. Chem. Biol.* **14**, 64–70 (2010). doi: 10.1016/j.cbpa.2009.10.022
45. Kurian, S. M., Di Pietro, A. Read, N. D. Live-cell imaging of conidial anastomosis tube fusion during colony initiation in *Fusarium oxysporum*. *PLoS One* **13**, e0195634 (2018). doi: 10.1371/journal.pone.0195634
46. Gonzalez, J. M., Hamm-Alvarez, S. Tan, J. C. H. Analyzing Live Cellularity in the Human Trabecular Meshwork. *Investig. Opthalmology Vis. Sci.* **54**, 1039 (2013). doi: 10.1167/iovs.12-10479
47. Singh, H. Bishen, K. A., Garg, D., Sukhija, H., Sharma, D., Tomar, U. Fixation and Fixatives: Roles and Functions—A Short Review. *Dent. J. Adv. Stud.* **07**, 51–55 (2019). doi: 10.1055/s-0039-1693098
48. Silva, R. N. Costa, C. C., Santos, M. J. G.,Alves, M. Q., Braga, S. S., Vieira, S. I., Rocha, J., Silva, A. M. S., Guieu, S. Fluorescent Light-up Probe for the Detection of Protein Aggregates. *Chem. – An Asian J.* **14**, 859–863 (2019). doi: 10.1002/asia.201801606
49. Jamur, M. C., Oliver, C. Permeabilization of Cell Membranes. in *Methods in molecular biology (Clifton, N.J.)* vol. 588 63–66 (2010). doi: 10.1007/978-1-59745-324-0_9
50. Hickey, P. C., Swift, S. R., Roca, M. G., Read, N. D. Live-cell Imaging of Filamentous Fungi Using Vital Fluorescent Dyes and Confocal Microscopy. in *Methods in Microbiology* , **34**, 63–87 (2005). doi: 10.1016/S0580-9517(04)34003-1
51. Gkerküçük, E. B., Tramier, M., Bertolin, G. Imaging mitochondrial functions: From fluorescent dyes to genetically-encoded sensors. *Genes (Basel).* **11**, (2020). doi: 10.3390/genes11020125
52. Gao, P., Pan, W., Li, N., Tang, B. Fluorescent probes for organelle-targeted bioactive species imaging. *Chem. Sci.* **10**, 6035–6071 (2019). doi: 10.1039/c9sc01652j

53. Tsien, R. Y., Ernst, L., Waggoner, A. Fluorophores for confocal microscopy: Photophysics and photochemistry. *Handb. Biol. Confocal Microsc.*, 3rd Edition. 338–352 (2006) doi:10.1007/978-0-387-45524-2_16.

54. Bucevičius, J., Lukinavičius, G. & Gerasimaitė, R. The Use of Hoechst Dyes for DNA Staining and beyond. *Chemosensors* **6**, (2018). doi: 10.3390/chemosensors6020018

55. Garcia-Rubio, R., de Oliveira, H. C., Rivera, J., Trevijano-Contador, N. The Fungal Cell Wall: *Candida*, *Cryptococcus*, and *Aspergillus* Species. *Front. Microbiol.* **10**, 1–13 (2020). doi: 10.3389/fmicb.2019.02993

56. Harrington, B. J., Hageage, G. J. Calcofluor White: A Review of its Uses and Applications in Clinical Mycology and Parasitology. *Lab. Med.* **34**, 361–367 (2003). doi: 10.1309/EPH2TDT8335GH0R3

57. Lavis, L. D., Raines, R. T. Bright Ideas for Chemical Biology. *ACS Chem. Biol.* **3**, 142–155 (2008). doi: 10.1021/cb700248m

58. Lee, W.-H. Loo, C.-Y., Bebawy, M., Luk, F., Mason, R., Rohanizadeh, R. Curcumin and its Derivatives: Their Application in Neuropharmacology and Neuroscience in the 21st Century. *Curr. Neuropharmacol.* **11**, 338–378 (2013). doi: 10.2174/1570159X11311040002

59. Zsila, F., Bikádi, Z., Simonyi, M. Unique, pH-dependent biphasic band shape of the visible circular dichroism of curcumin–serum albumin complex. *Biochem. Biophys. Res. Commun.* **301**, 776–782 (2003). doi: 10.1016/S0006-291X(03)00030-5

60. Chaicham, A., Kulchat, S., Tumcharern, G., Tuntulani, T., Tomapatanaget, B. Synthesis, photophysical properties, and cyanide detection in aqueous solution of BF_2-curcumin dyes. *Tetrahedron* **66**, 6217–6223 (2010). doi: 10.1016/j.tet.2010.05.088

61. Priyadarsini, K. I. Photophysics, photochemistry and photobiology of curcumin: Studies from organic solutions, bio-mimetics and living cells. *J. Photochem. Photobiol. C Photochem. Rev.* **10**, 81–95 (2009). doi: 10.1016/j.jphotochemrev.2009.05.001

62. D’Aléo, A. Felouat, A., Heresanu, V., Ranguis, A., Chaudanson, D., Karapetyan, A., Giorgi, M., Fages, F. Two-photon excited fluorescence of BF_2 complexes of curcumin analogues: Toward NIR-to-NIR fluorescent organic nanoparticles. *J.*

Mater. Chem. C **2**, 5208–5215 (2014). doi: 10.1039/c4tc00543k

63. Chignell, C. F. Bilskj, P., Reszka, K. J., Motten, A. G., Sik, R. H., Dahl, T. A. Spectral and photochemical properties of curcumin. *Photochem. Photobiol.* **59**, 295–302 (1994). doi: 10.1111/j.1751-1097.1994.tb05037.x
64. Li, M., Zhang, Z., Hill, D. L., Wang, H., Zhang, R. Curcumin, a dietary component, has anticancer, chemosensitization, and radiosensitization effects by down-regulating the *MDM2* oncogene through the PI3K/mTOR/ETS2 pathway. *Cancer Res.* **67**, 1988–1996 (2007). doi: 10.1158/0008-5472.CAN-06-3066
65. Carmello, J. C., Pavarina, A. C., Oliveira, R., Johansson, B. Genotoxic effect of photodynamic therapy mediated by curcumin on *Candida albicans*. *FEMS Yeast Res.* **15**, 1–9 (2015). doi: 10.1093/femsyr/fov018
66. Li, W., Suwanwela, N. C., Patumraj, S. Curcumin by down-regulating NF-kB and elevating Nrf2, reduces brain edema and neurological dysfunction after cerebral I/R. *Microvasc. Res.* **106**, 117–127 (2016). doi: 10.1016/j.mvr.2015.12.008
67. Sökmen, M., Akram Khan, M. The antioxidant activity of some curcuminoids and chalcones. *Inflammopharmacology* **24**, 81–86 (2016). doi: 10.1007/s10787-016-0264-5
68. Prasad, S., Tyagi, A. K., Aggarwal, B. B. Recent Developments in Delivery, Bioavailability, Absorption and Metabolism of Curcumin: the Golden Pigment from Golden Spice. *Cancer Res. Treat.* **46**, 2–18 (2014). doi: 10.4143/crt.2014.46.1.2
69. Schneider, C., Gordon, O. N., Edwards, R. L., Luis, P. B. Degradation of Curcumin: From Mechanism to Biological Implications. in *Journal of Agricultural and Food Chemistry* vol. 63 7606–7614 (2015). doi: 10.1021/acs.jafc.5b00244
70. Zhang, X., Ye, M., Li, R., Yin, J., Guo, D. A. Microbial transformation of curcumin by *Rhizopus chinensis*. *Biocatal. Biotransformation* **28**, 380–386 (2010). doi: 10.3109/10242422.2010.532870
71. Sato, T., Hotsumi, M., Makabe, K., Konno, H. Design, synthesis and evaluation of curcumin-based fluorescent probes to detect Aβ fibrils. *Bioorg. Med. Chem. Lett.* **28**, 3520–3525 (2018). doi: 10.1016/J.BMCL.2018.10.002
72. Devi, Y. S., DeVine, M., DeKuiper, J., Ferguson, S., Fazleabas, A. T. Inhibition of IL-6 signaling pathway by curcumin in uterine decidual cells. *PLoS One* **10**, 1–18 (2015). doi: 10.1371/journal.pone.0125627

73. Hong, J. Modulation of arachidonic acid metabolism by curcumin and related β-diketone derivatives: effects on cytosolic phospholipase A2, cyclooxygenases and 5-lipoxygenase. *Carcinogenesis* **25**, 1671–1679 (2004). doi: 10.1093/carcin/bgh165

74. Saidi, A. Kasabova, M., Vanderlynden, L., Wartenberg, M., Kara-Ali, G. H., Marc, D., Lecaille, F., Lalmanach, G. Curcumin inhibits the TGF-β1-dependent differentiation of lung fibroblasts via PPARγ-driven upregulation of cathepsins B and L. *Sci. Rep.* **9**, 491 (2019). doi: 10.1038/s41598-018-36858-3

75. Staderini, M., Martín, M. A., Bolognesi, M. L., Menéndez, J. C. Imaging of β-amyloid plaques by near infrared fluorescent tracers: A new frontier for chemical neuroscience. *Chem. Soc. Rev.* **44**, 1807–1819 (2015). doi: 10.1039/C4CS00337C

76. Garcia-Alloza, M., Borrelli, L. A., Rozkalne, A., Hyman, B. T., Bacskai, B. J. Curcumin labels amyloid pathology *in vivo*, disrupts existing plaques, and partially restores distorted neurites in an Alzheimer mouse model. *J. Neurochem.* **102**, 1095–1104 (2007). doi: 10.1111/j.1471-4159.2007.04613.x

77. Chongzhao, R. Xu, X., Raymond, S. B., Ferrara, B. J., Neal, K., Bacskai, B. J., Medarova, Z., Moore, A. Design, synthesis, and testing of difluoroboron-derivatized curcumins as near-infrared probes for in vivo detection of amyloid-β deposits. *J. Am. Chem. Soc.* **131**, 15257–15261 (2009). doi: 10.1021/ja9047043

78. Zhang, X. Tian, Y., Li, Z., Tian, X., Sun, H., Liu, H. Design and synthesis of curcumin analogues for *in vivo* fluorescence imaging and inhibiting copper-induced cross-linking of amyloid beta species in alzheimer's disease. *J. Am. Chem. Soc.* **135**, 16397–16409 (2013). doi: 10.1021/ja405239v

79. Yang, J. Cheng, R., Fu, H., Yang, J., Kumar, M., Lu, J., Xu, Y., Liang, S. H., Cui, M., Ran, C. Half-curcumin analogues as PET imaging probes for amyloid beta species. *Chem. Commun.* **55**, 3630–3633 (2019). doi: 10.1039/C8CC10166C

80. Lampe, V. Synthese von Curcumin. *Berichte der Dtsch. Chem. Gesellschaft* **51**, 1347–1355 (1918). doi: 10.1002/cber.19180510223

81. Dias, L. D., Blanco, K. C., Mfouo-Tynga, I. S., Inada, N. M., Bagnato, V. S. Curcumin as a photosensitizer: From molecular structure to recent advances in antimicrobial photodynamic therapy. *J. Photochem. Photobiol. C Photochem. Rev.* **45**, 100384 (2020). doi: 10.1016/j.jphotochemrev.2020.100384

82. Pabon, H. J. J. A synthesis of curcumin and related compounds. *Recl. des Trav.*

Chim. des Pays-Bas **83**, 379–386 (1964). doi: 10.1002/recl.19640830407

83. Bai, G. Yu, C., Cheng, C., Hao, E., Wei, Y., Mu, X., Jiao, L. Syntheses and photophysical properties of BF_2 complexes of curcumin analogues. *Org. Biomol. Chem.* **12**, 1618–1626 (2014). doi: 10.1039/C3OB42201A

84. Liu, K., Chen, J., Chojnacki, J., Zhang, S. $BF_3{\cdot}OEt_2$-promoted concise synthesis of difluoroboron-derivatized curcumins from aldehydes and 2,4-pentanedione. *Tetrahedron Lett.* **54**, 2070–2073 (2013). doi: 10.1016/j.tetlet.2013.02.015

85. Wichitnithad, W., Nimmannit, U., Wacharasindhu, S., Rojsitthisak, P. Synthesis, characterization and biological evaluation of succinate prodrugs of curcuminoids for colon cancer treatment. *Molecules* **16**, 1888–1900 (2011). doi: 10.3390/molecules16021888

86. Nichols, C. E., Youssef, D., Harris, R. G., Jha, A. Microwave-assisted synthesis of curcumin analogs. *Arkivoc* **2006**, 64–72 (2006).

87. Fedorenko, E. V., Mirochnik, A. G., Beloliptsev, A. Y., Isakov, V. V. (S2→S0) and (S1→S0) luminescence of dimethylaminostyryl-β-Diketonates of boron difluoride. *Dye. Pigment.* **109**, 181–188 (2014). doi: 10.1016/j.dyepig.2014.04.016

88. Bai, G. *et al.* Syntheses and photophysical properties of BF_2 complexes of curcumin analogues. *Org. Biomol. Chem.* **12**, 1618–1626 (2014). doi: 10.1039/C3OB42201A

89. Walker, G. M., White, N. A. Introduction to Fungal Physiology. in *Fungi* 1–34 (John Wiley & Sons, Ltd, 2005). doi:10.1002/0470015330.ch1.

90. Read, N. D. Fungal cell structure and organization. in *Oxford Textbook of Medical Mycology* (eds. Kibbler, C. C. et al.), **1**, 1–31 (Oxford University Press, 2017). doi: 10.1093/med/9780198755388.003.0004

91. Gow, N. A. R., Latge, J.-P., Munro, C. A. The Fungal Cell Wall: Structure, Biosynthesis, and Function. *The Fungal Kingdom* **5**, 267–292 (2017). doi: 10.1128/microbiolspec.FUNK-0035-2016

92. Madigan, M. T., Martinko, J. M., Bender, K. S., Buckley, D. H. & Stahl, D. A. *Brock Biology of Microorganisms*, 14th edition. (Pearson Education, 2015).

93. Money, N. P. Spore Production, Discharge, and Dispersal. in *The Fungi* 67–97 (Elsevier, 2016). doi:10.1016/B978-0-12-382034-1.00003-7.

94. Lyons, R. Stiller, J., Powell, J., Rusu, A., Manners, J. M., Kazan, K. *Fusarium oxysporum* triggers tissue-specific transcriptional reprogramming in *Arabidopsis*

thaliana. *PLoS One* **10**, 1–23 (2015). doi: 10.1371/journal.pone.0121902

95. Carter, M., Shieh, J. C. Cell Culture Techniques. in *Guide to Research Techniques in Neuroscience* (eds. Wilson, K. & Walker, J.), **12**, 281–296 (Elsevier, 2010). doi: 10.1016/B978-0-12-374849-2.00013-6
96. Ramage, G., Saville, S. P., Thomas, D. P., López-Ribot, J. L. *Candida* biofilms: An update. *Eukaryotic Cell*, **4**, 633–638 (2005). doi: 10.1128/EC.4.4.633-638.2005
97. Xie, H. R., Hu, L. Sen , Li, G. Y. SH-SY5Y human neuroblastoma cell line: *In vitro* cell model of dopaminergic neurons in Parkinson's disease. *Chinese Medical Journal*, **123**, 1086–1092 (2010). doi: 10.3760/cma.j.issn.0366-6999.2010.08.021
98. Biedler, J. L., Helson, L., Spengler, B. A. Morphology and Growth, Tumorigenicity, and Cytogenetics of Human Neuroblastoma Cells in Continuous Culture. *Cancer Res.* **33**, 2643–2652 (1973).
99. Kovalevich, J., Langford, D. Considerations for the Use of SH-SY5Y Neuroblastoma Cells in Neurobiology. in *Neuronal Cell Culture: Methods and Protocols* (eds. Amini, S. & White, M. K.), **1078**, 9–21 (Humana Press, 2013). doi: 10.1007/978-1-62703-640-5_2
100. Påhlman, S., Ruusala, A.-I., Abrahamsson, L., Mattsson, M. E. K., Esscher, T. Retinoic acid-induced differentiation of cultured human neuroblastoma cells: a comparison with phorbolester-induced differentiation. *Cell Differ.* **14**, 135–144 (1984). doi: 10.1016/0045-6039(84)90038-1
101. Biedler, J. L., Schachner, M. Multiple Neurotransmitter Synthesis by Human Neuroblastoma Cell Lines and Clones. *Cancer Res.* **38**, 3751–3757 (1978).
102. Aslantürk, Ö. S. *In Vitro* Cytotoxicity and Cell Viability Assays: Principles, Advantages, and Disadvantages. *Genotoxicity - A Predict. Risk to Our Actual World* 1–18 (2018) doi:10.5772/intechopen.71923.
103. OECD. List of viability testing methods (non-inclusive) of cell cultures. in *Guidance Document on Good In Vitro Method Practices (GIVIMP)* 181–186 (OECD Publishing, 2018). doi:10.1787/9789264304796-en
104. Strober, W. Trypan Blue Exclusion Test of Cell Viability. *Curr. Protoc. Immunol.* A3.B1-A3.B3 (2015) doi:10.1002/0471142735.ima03bs111.
105. Riss, T. L. Moravec, R. A., Niles, A. L., Duellman, S., Benink, H. A., Worzella, T. J., Minor, L. Cell Viability Assays. *Assay Guid. Man.* 1–25 (2004).

106. O’Brien, J., Wilson, I., Orton, T. Pognan, F. Investigation of the Alamar Blue (resazurin) fluorescent dye for the assessment of mammalian cell cytotoxicity. *Eur. J. Biochem.* **267**, 5421–5426 (2000). doi:10.1046/j.1432-1327.2000.01606.x

107. Hasan, Z. A. E., Mohd Zainudin, N. A. I., Aris, A., Ibrahim, M. H., Yusof, M. T. Biocontrol efficacy of *Trichoderma asperellum*-enriched coconut fibre against *Fusarium* wilts of cherry tomato. *J. Appl. Microbiol.* **129**, 991–1003 (2020). doi: 10.1111/jam.14674

108. Saad, M. M. G., Kandil, M.,Mohammed, Y. M. M. Isolation and Identification of Plant Growth-Promoting Bacteria Highly Effective in Suppressing Root Rot in Fava Beans. *Curr. Microbiol.* **77**, 2155–2165 (2020). doi: 10.1007/s00284-020-02015-1

109. Jinal, N. H., Amaresan, N. Evaluation of biocontrol *Bacillus* species on plant growth promotion and systemic-induced resistant potential against bacterial and fungal wilt-causing pathogens. *Arch. Microbiol.* **202**, 1785–1794 (2020). doi: 10.1007/s00203-020-01891-2

110. Mirochnik, A. G., Bukvetskii, B. V., Gukhman, E. V., Zhikhareva, P. A., Karasev, V. E. Crystal structure and luminescence of boron difluoride acetylacetonate. *Russ. J. Gen. Chem.* **72**, 737–740 (2002). doi: 10.1023/A:1019508318683

111. Da Rocha, J. F., Da Cruz E Silva, O. A. B., Vieira, S. I. Analysis of the amyloid precursor protein role in neuritogenesis reveals a biphasic SH-SY5Y neuronal cell differentiation model. *J. Neurochem.* **134**, 288–301 (2015). doi: 10.1111/jnc.13133

112. Pina, S. Vieira, S.I., Torres, P. M. C., Goetz-Neunhoeffer, F., Neubauer, J., da Cruz e Silva, O. A. B., da Cruz e Silva, E. F., Ferreira, J. M. F. *In vitro* performance assessment of new brushite-forming Zn- and ZnSr-substituted β-TCP bone cements. *J. Biomed. Mater. Res. Part B Appl. Biomater.* **94**, (2010). doi: 10.1002/jbm.b.31669

113. Rivoal, M., Zaborova, E., Canard, G., D’Aléo, A., Fages, F. Synthesis, electrochemical and photophysical studies of the borondifluoride complex of a meta-linked biscurcuminoid. *New J. Chem.* **40**, 1297–1305 (2016). doi:10.1039/c5nj00925a

114. Allen, F. H. Kennard, O., Watson, D. G., Brammer, L., Orpen, A. G., Taylor, R. Tables of bond lengths determined by x-ray and neutron diffraction. Part 1. Bond lengths in organic compounds. *J. Chem. Soc. Perkin Trans. 2* S1–S19 (1987) doi:10.1039/P298700000S1

115. Borra, R. C., Lotufo, M. A., Gagioti, S. M., Barros, F. de M., Andrade, P. M. A simple method to measure cell viability in proliferation and cytotoxicity assays. *Braz. Oral Res.* **23**, 255–262 (2009). doi:10.1590/S1806-83242009000300006

116. Rentería-Martínez, M. E., Guerra-Camacho, M. Á., Ochoa-Meza, A., Moreno-Salazar, S. F., Meza-Moller, A. D. C., Guzmán-Ortiz, J. M. Description and comparison among morphotypes of *Fusarium brachygibbosum*, *F. falciforme* and *F. oxysporum* pathogenic to watermelon in Sonora, Mexico. *Rev. Mex. Fitopatol. Mex. J. Phytopathol.* **37**, 16–34 (2018). doi: 10.18781/R.MEX.FIT.1808-1

117. Leica Microsystems Fluorescence Microscopy

118. Di Pietro, A., Garcia-Maceira, F. I., Meglecz, E., Roncero, M. I. G. A MAP kinase of the vascular wilt fungus *Fusarium oxysporum* is essential for root penetration and pathogenesis. *Mol. Microbiol.* **39**, 1140–1152 (2001). doi: 10.1046/j.1365-2958.2001.02307.x

119. Zdybicka-Barabas, A. Stączek, S., Mak, P., Piersiak, T., Skrzypiec, K., Cytryńska, M. The effect of *Galleria mellonella* apolipophorin III on yeasts and filamentous fungi. *J. Insect Physiol.* **58**, 164–177 (2012). doi: 10.1016/j.jinsphys.2011.11.003

120. Shahi, S., Beerens, B., Bosch, M., Linmans, J., Rep, M. Nuclear dynamics and genetic rearrangement in heterokaryotic colonies of *Fusarium oxysporum*. *Fungal Genet. Biol.* **91**, 20–31 (2016). doi: 10.1016/j.fgb.2016.03.003

121. Constantinescu, R., Constantinescu, A. T., Reichmann, H., Janetzky, B. Neuronal differentiation and long-term culture of the human neuroblastoma line SH-SY5Y. *J. Neural Transm. Suppl.* 17–28 (2007) doi:10.1007/978-3-211-73574-9-3.

122. Kazantzis, K. T. Koutsonikoli, K., Mavroidi, B., Zachariadis, M., Alexiou, P., Pelecanou, M., Politopoulos, K., Alexandratou, E., Sagnou, M. Curcumin derivatives as photosensitizers in photodynamic therapy: Photophysical properties and: In vitro studies with prostate cancer cells. *Photochem. Photobiol. Sci.* **19**, 193–206 (2020). doi: 10.1039/c9pp00375d

6. CHAPTER VI

COPYRIGHTS

COPYRIGHTS

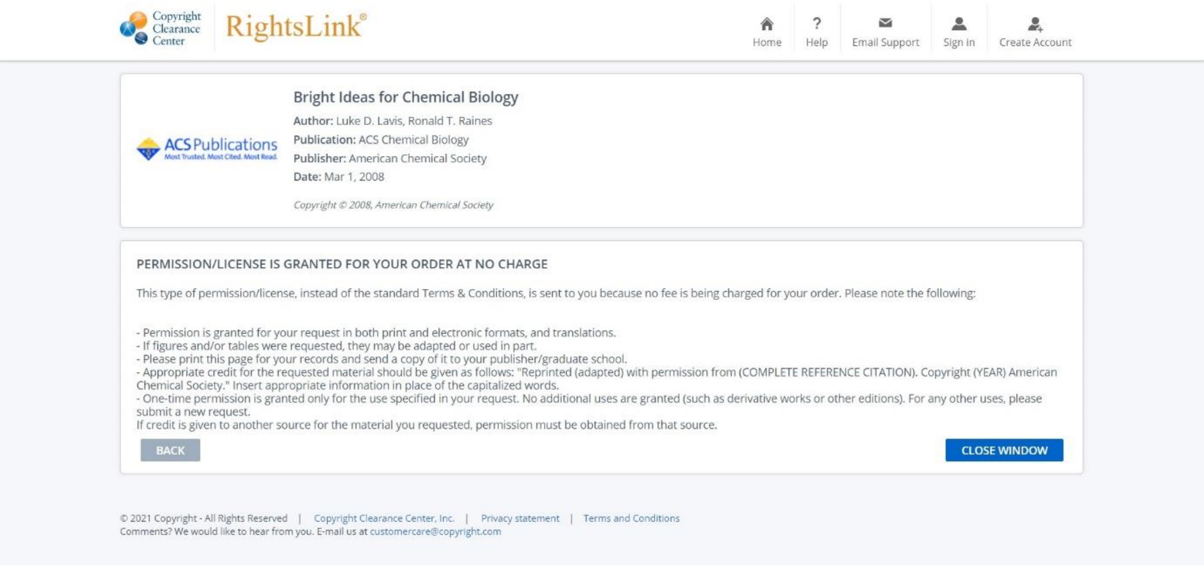

Bright Ideas for Chemical Biology

Author: Luke D. Lavis, Ronald T. Raines
Publication: ACS Chemical Biology
Publisher: American Chemical Society
Date: Mar 1, 2008

Copyright © 2008, American Chemical Society

PERMISSION/LICENSE IS GRANTED FOR YOUR ORDER AT NO CHARGE

This type of permission/license, instead of the standard Terms & Conditions, is sent to you because no fee is being charged for your order. Please note the following:

- Permission is granted for your request in both print and electronic formats, and translations.
- If figures and/or tables were requested, they may be adapted or used in part.
- Please print this page for your records and send a copy of it to your publisher/graduate school.
- Appropriate credit for the requested material should be given as follows: "Reprinted (adapted) with permission from (COMPLETE REFERENCE CITATION). Copyright (YEAR) American Chemical Society." Insert appropriate information in place of the capitalized words.
- One-time permission is granted only for the use specified in your request. No additional uses are granted (such as derivative works or other editions). For any other uses, please submit a new request.

If credit is given to another source for the material you requested, permission must be obtained from that source.

© 2021 Copyright - All Rights Reserved | Copyright Clearance Center, Inc. | Privacy statement | Terms and Conditions
Comments? We would like to hear from you. E-mail us at customercare@copyright.com

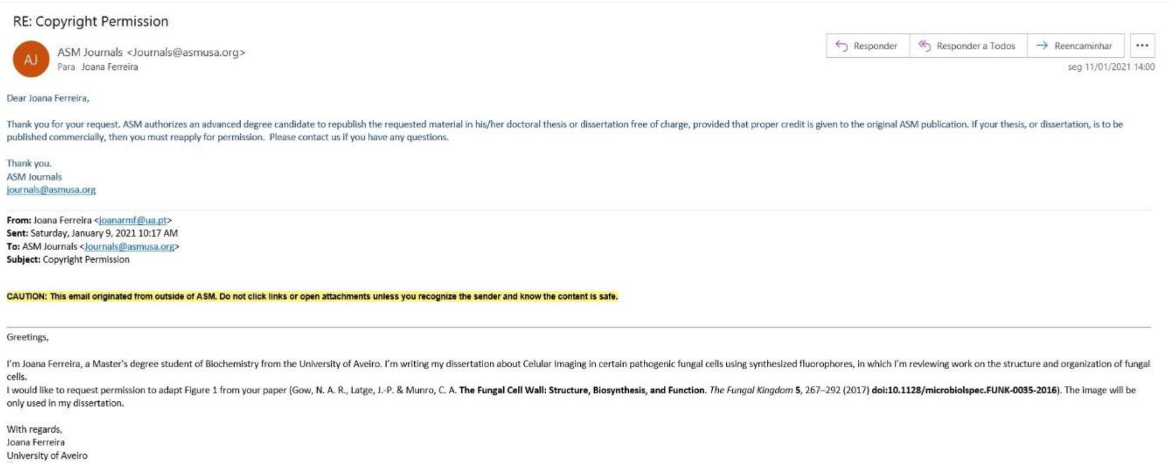

RE: Copyright Permission

ASM Journals <Journals@asmusa.org>
Para Joana Ferreira
seg 11/01/2021 14:00

Dear Joana Ferreira,

Thank you for your request. ASM authorizes an advanced degree candidate to republish the requested material in his/her doctoral thesis or dissertation free of charge, provided that proper credit is given to the original ASM publication. If your thesis, or dissertation, is to be published commercially, then you must reapply for permission. Please contact us if you have any questions.

Thank you.
ASM Journals
journals@asmusa.org

From: Joana Ferreira <joanarmf@ua.pt>
Sent: Saturday, January 9, 2021 10:17 AM
To: ASM Journals <Journals@asmusa.org>
Subject: Copyright Permission

CAUTION: This email originated from outside of ASM. Do not click links or open attachments unless you recognize the sender and know the content is safe.

Greetings,

I'm Joana Ferreira, a Master's degree student of Biochemistry from the University of Aveiro. I'm writing my dissertation about Celular Imaging in certain pathogenic fungal cells using synthesized fluorophores, in which I'm reviewing work on the structure and organization of fungal cells.
I would like to request permission to adapt Figure 1 from your paper (Gow, N. A. R., Latge, J.-P. & Munro, C. A. **The Fungal Cell Wall: Structure, Biosynthesis, and Function**. *The Fungal Kingdom* **5**, 267–292 (2017) **doi:10.1128/microbiolspec.FUNK-0035-2016**). The image will be only used in my dissertation.

With regards,
Joana Ferreira
University of Aveiro

7. CHAPTER VII

Attachments

7.1. Attachment A – NMR characterization (^{1}H, ^{19}F, ^{13}C, COSY, HSQC, HMBC) of derivatives 2a, 3a, 3c-e and 4

Derivative 2a

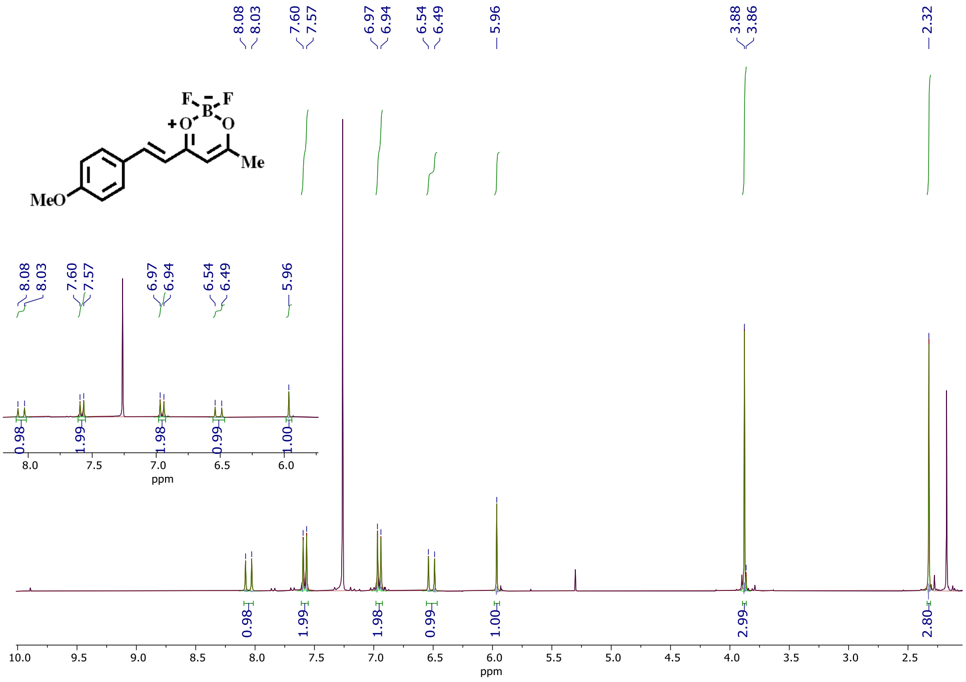

Figure 51: ^{1}H NMR spectrum of derivative **2a**, in $CDCl_3$.

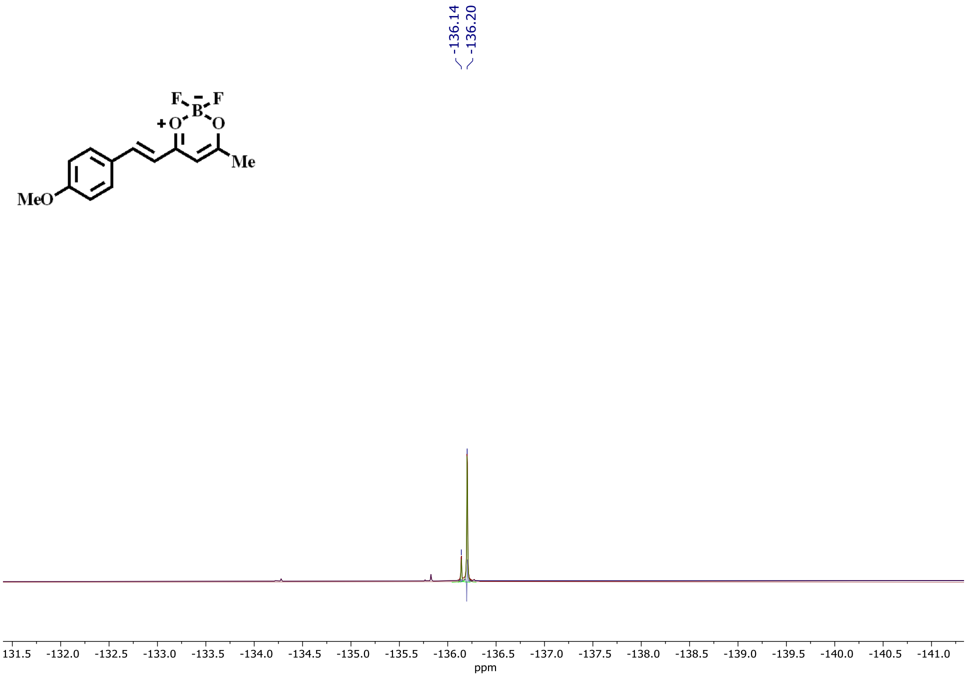

Figure 52: ^{19}F NMR spectrum of derivative **2a**, in $CDCl_3$.

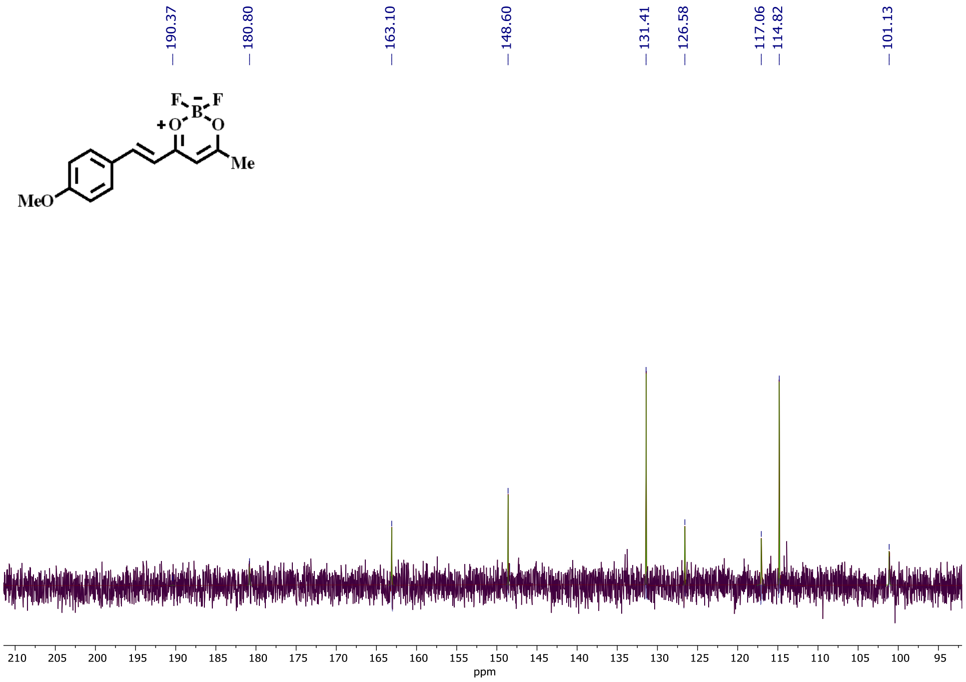

Figure 53: ^{13}C NMR spectrum of derivative **2a**, in $CDCl_3$.

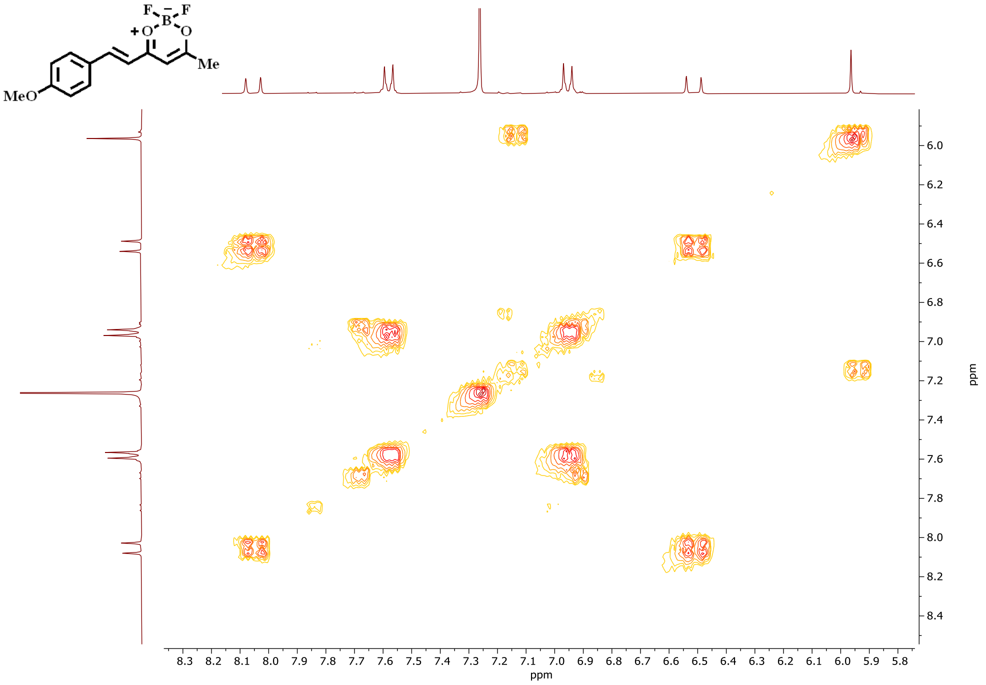

Figure 54: COSY NMR spectrum of derivative **2a**, in CDCl$_3$.

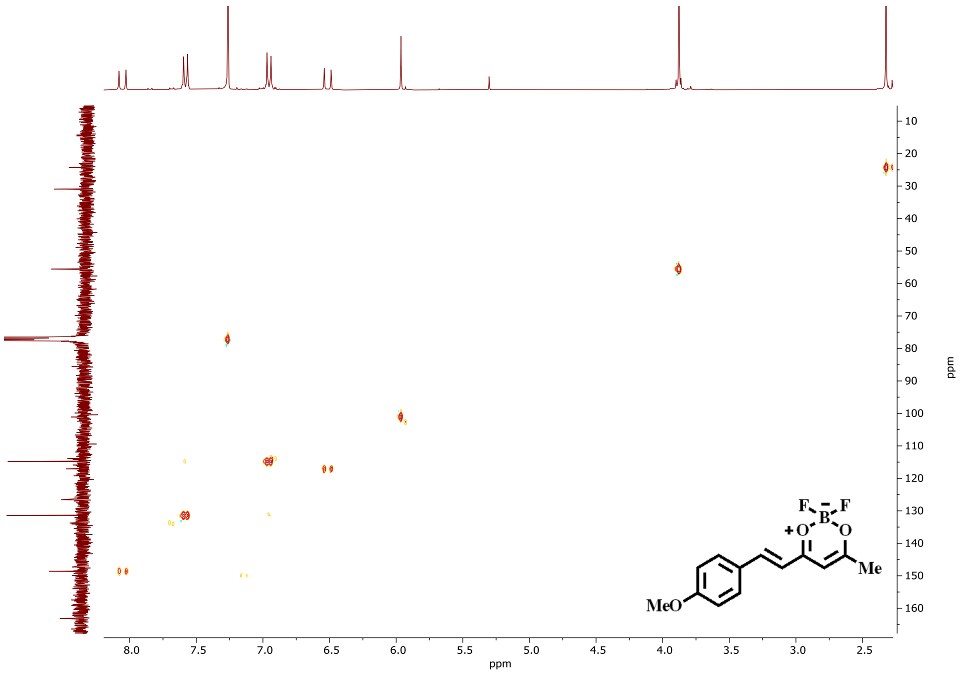

Figure 55: HSQC NMR spectrum of derivative **2a**, in CDCl$_3$.

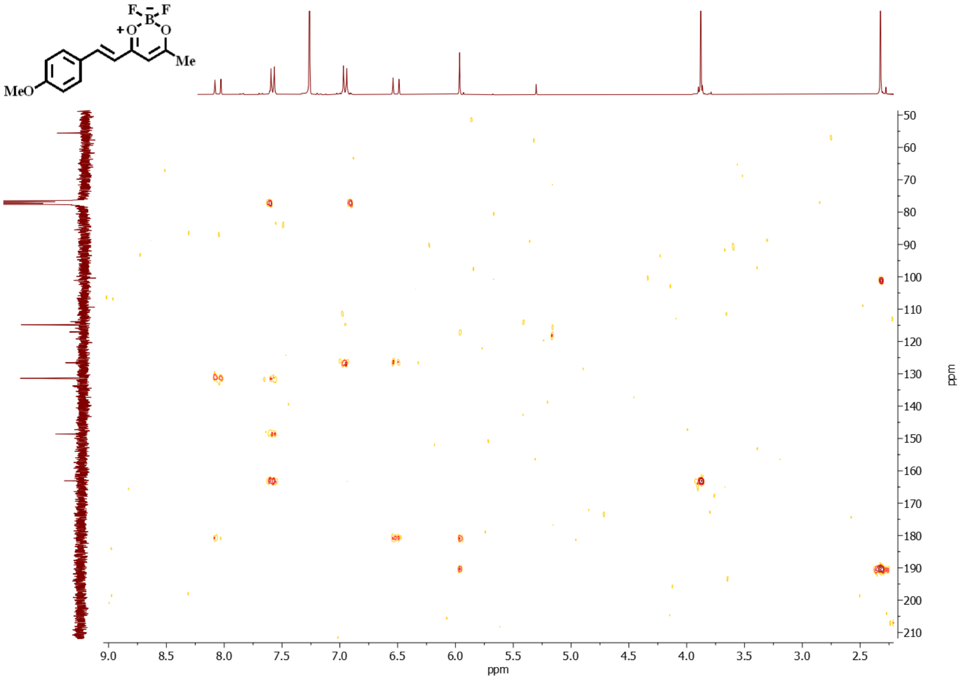

Figure 56: HMBC NMR spectrum of derivative **2a**, in $CDCl_3$.

Derivative 3a

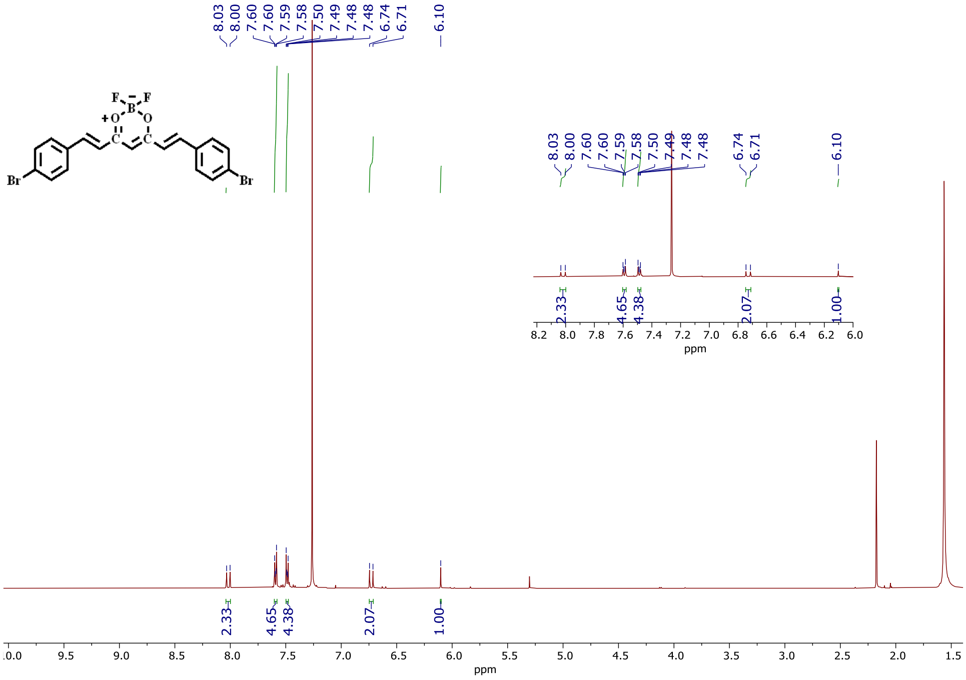

Figure 57: ^{1}H NMR spectrum of derivative **3a**, in $CDCl_3$.

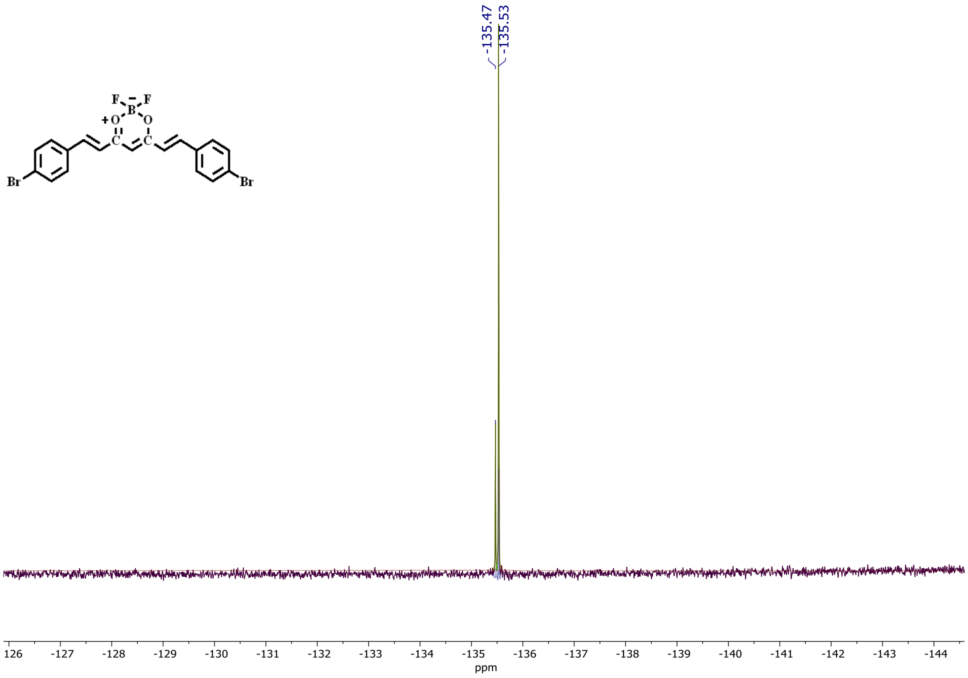

Figure 58: ^{19}F NMR spectrum of derivative **3a**, in $CDCl_3$.

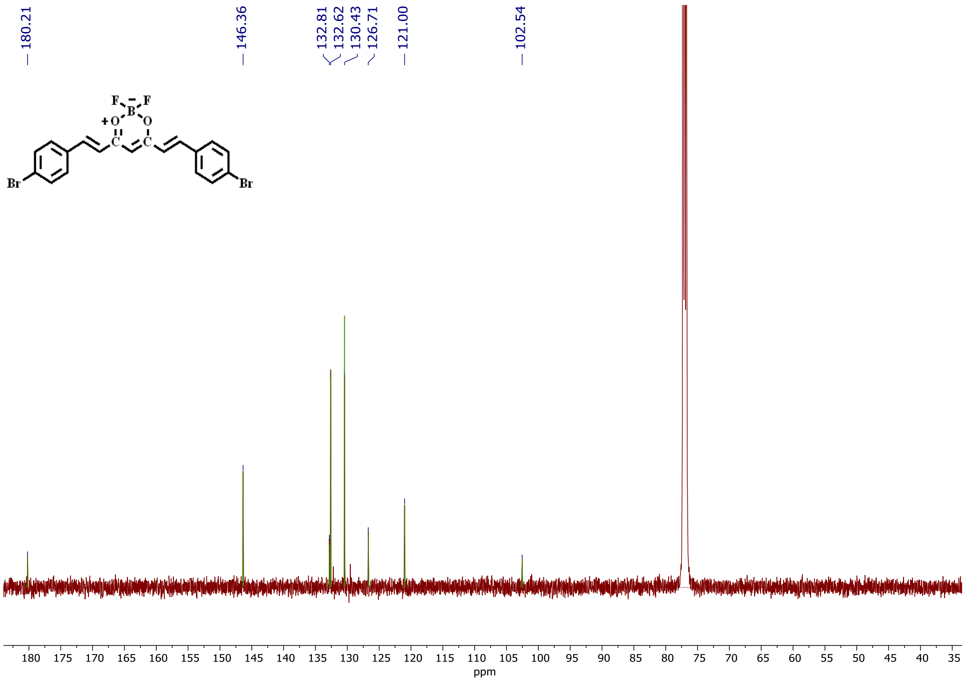

Figure 59: ^{13}C NMR spectrum of derivative **3a**, in $CDCl_3$.

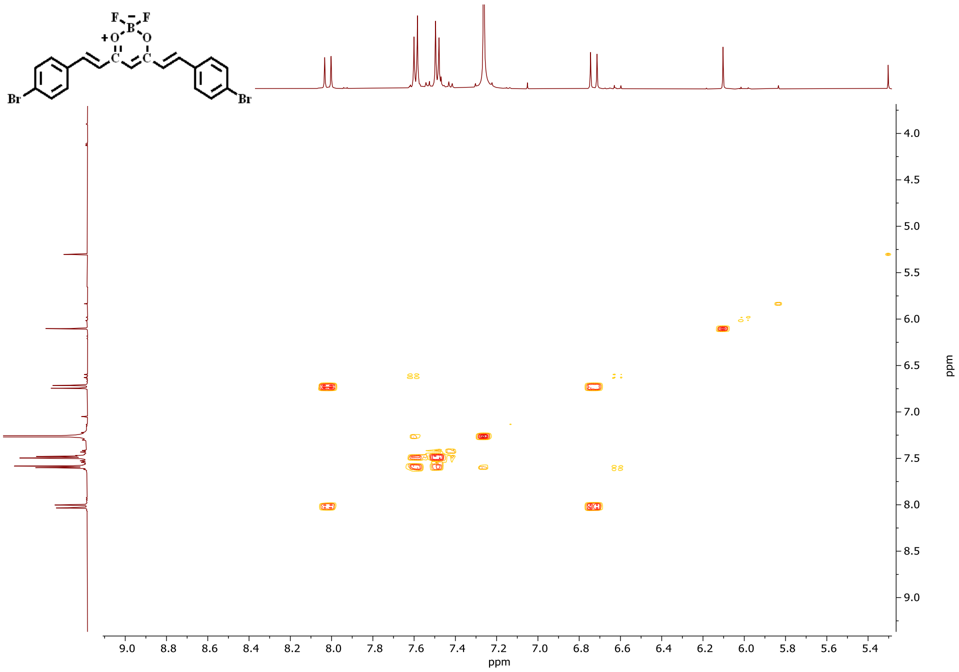

Figure 60: COSY NMR spectrum of derivative **3a**, in $CDCl_3$.

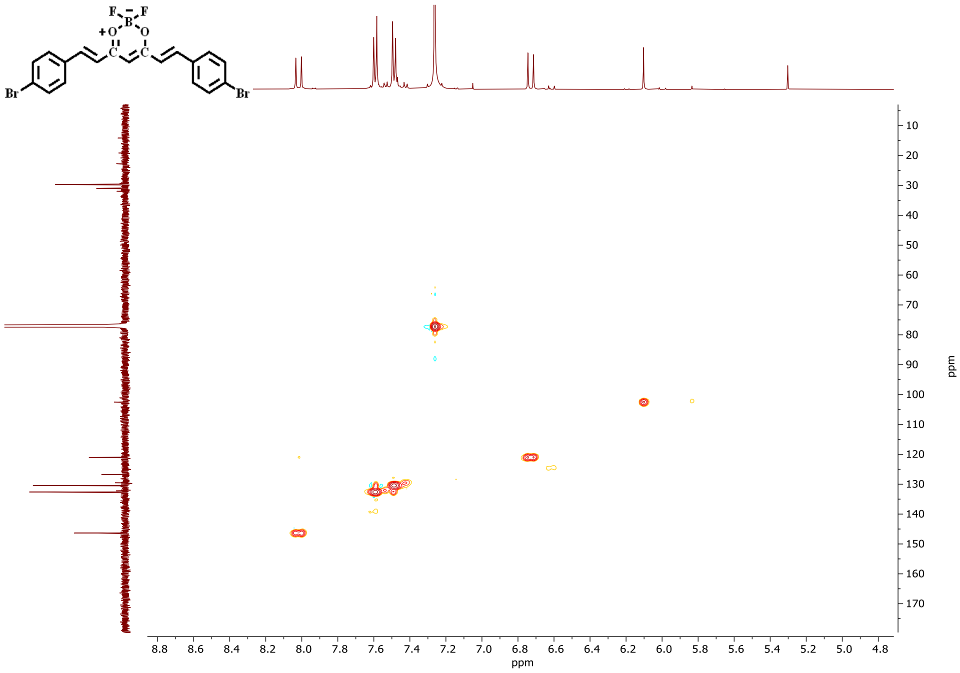

Figure 61: HSQC NMR spectrum of derivative **3a**, in $CDCl_3$.

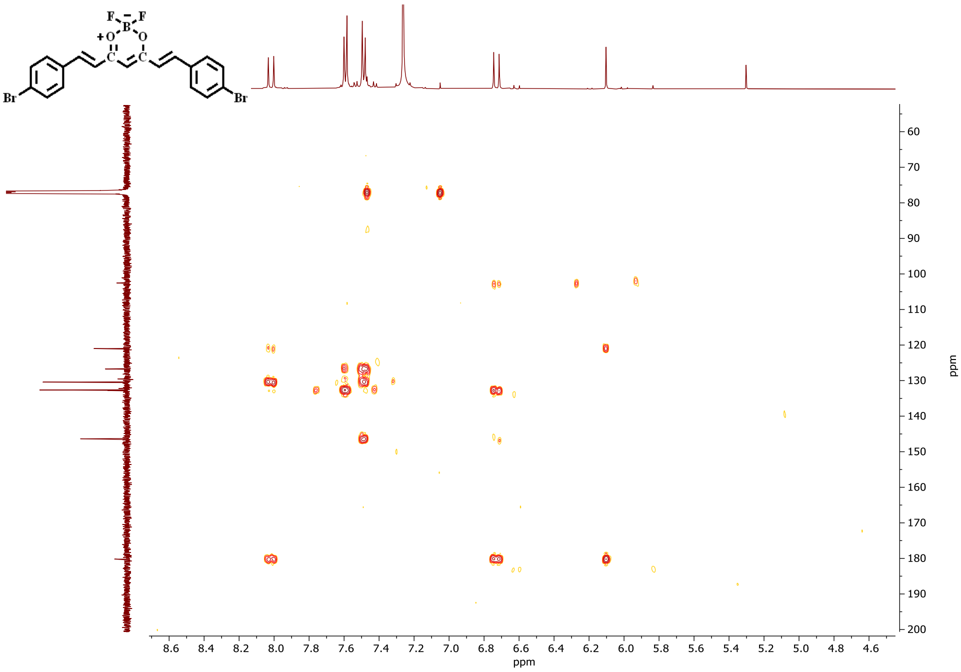

Figure 62: HMBC NMR spectrum of derivative **3a**, in $CDCl_3$.

Derivative 3c

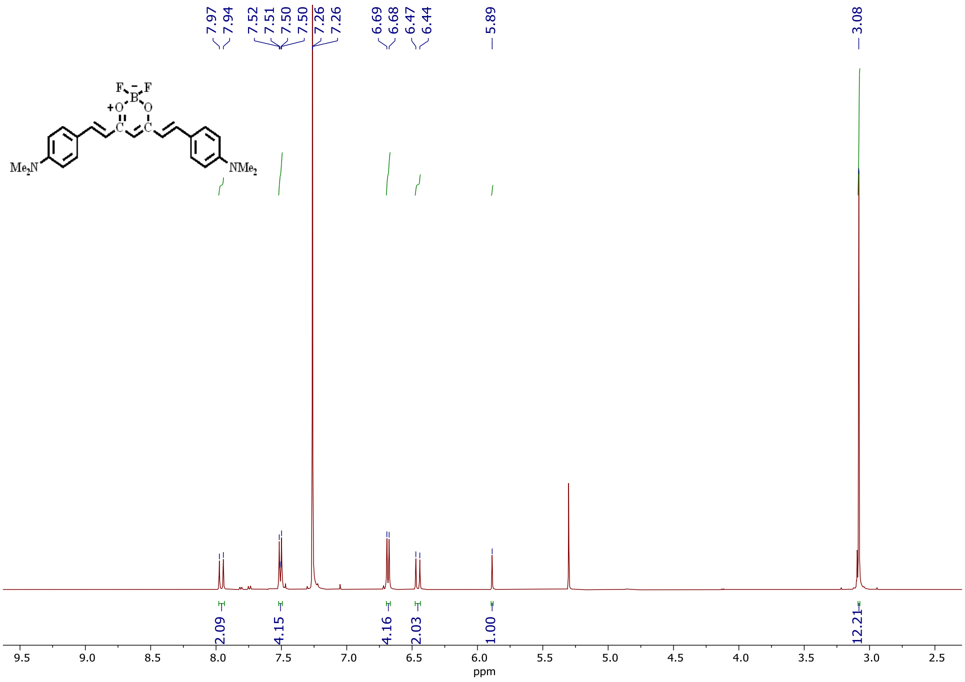

Figure 63: ^{1}H NMR spectrum of derivative **3c**, in $CDCl_3$.

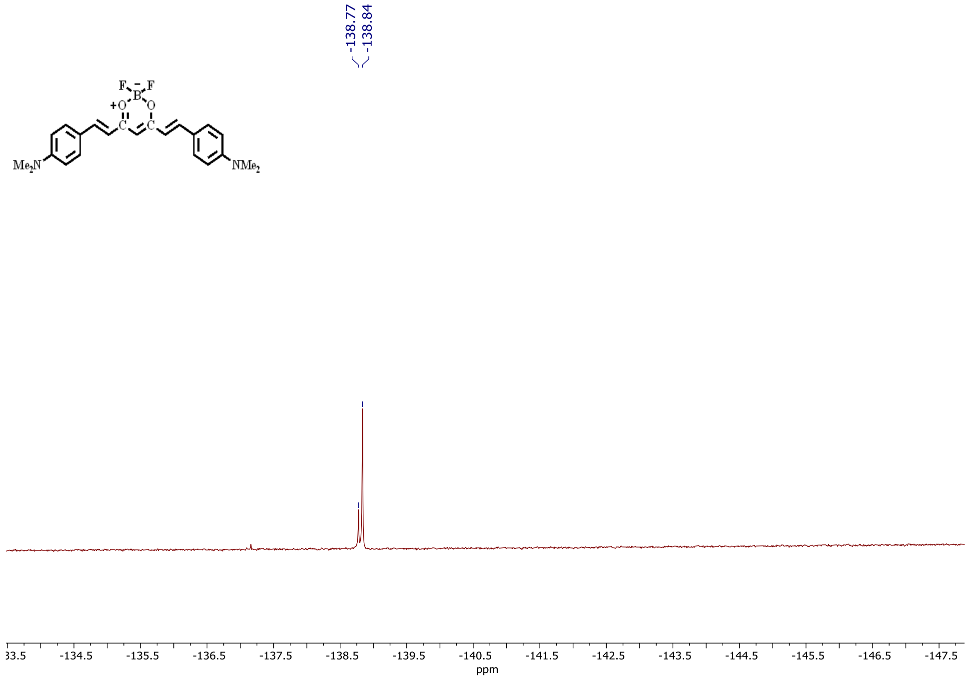

Figure 64: ^{19}F NMR spectrum of derivative **3c**, in CDCl$_3$.

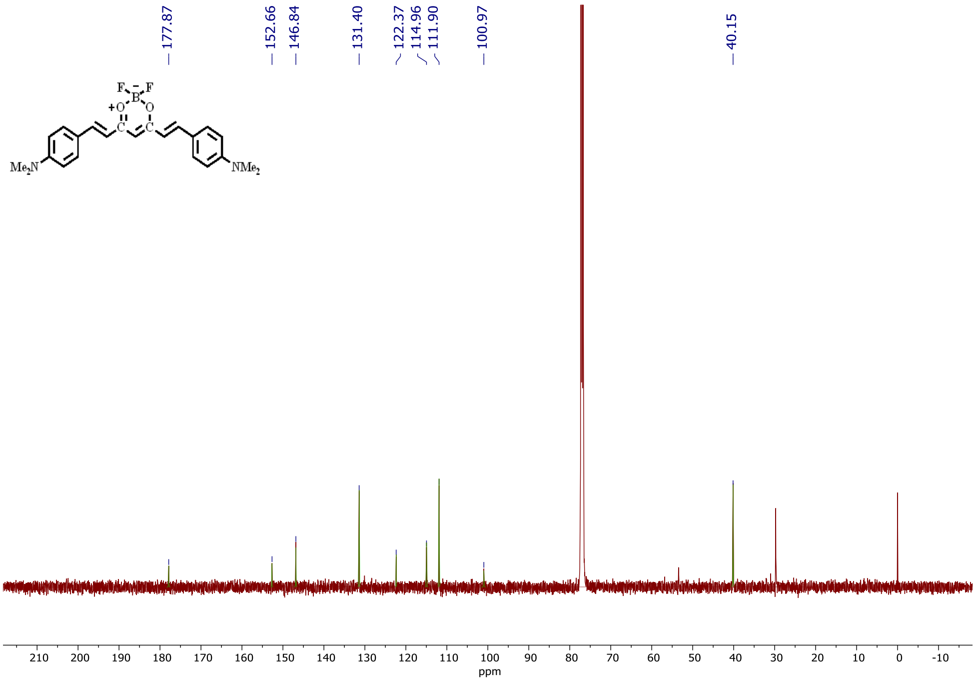

Figure 65: ^{13}C NMR spectrum of derivative **3c**, in CDCl$_3$.

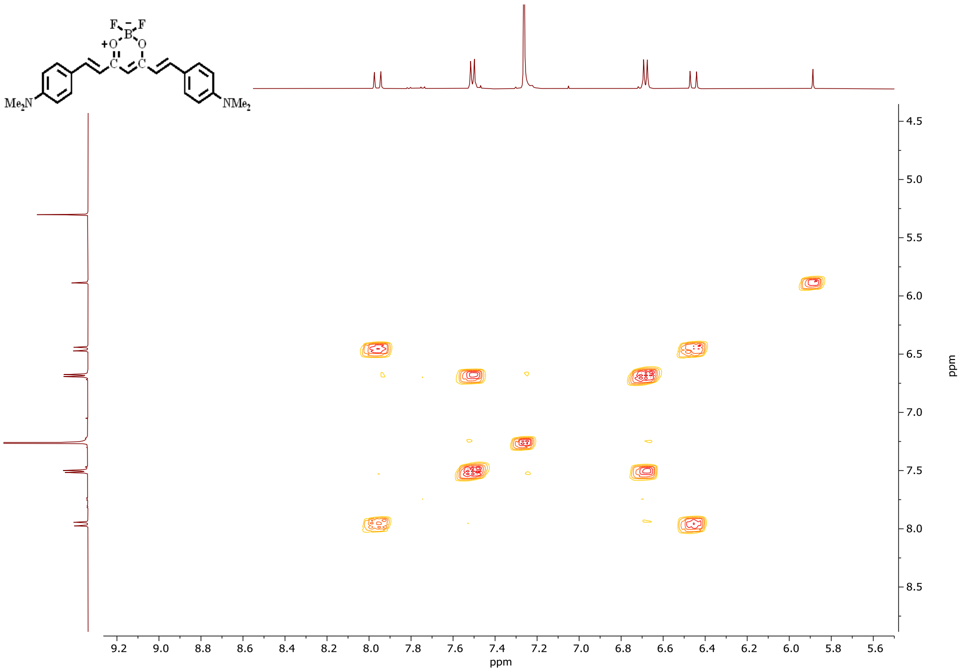

Figure 66: COSY NMR spectrum of derivative **3c**, in $CDCl_3$.

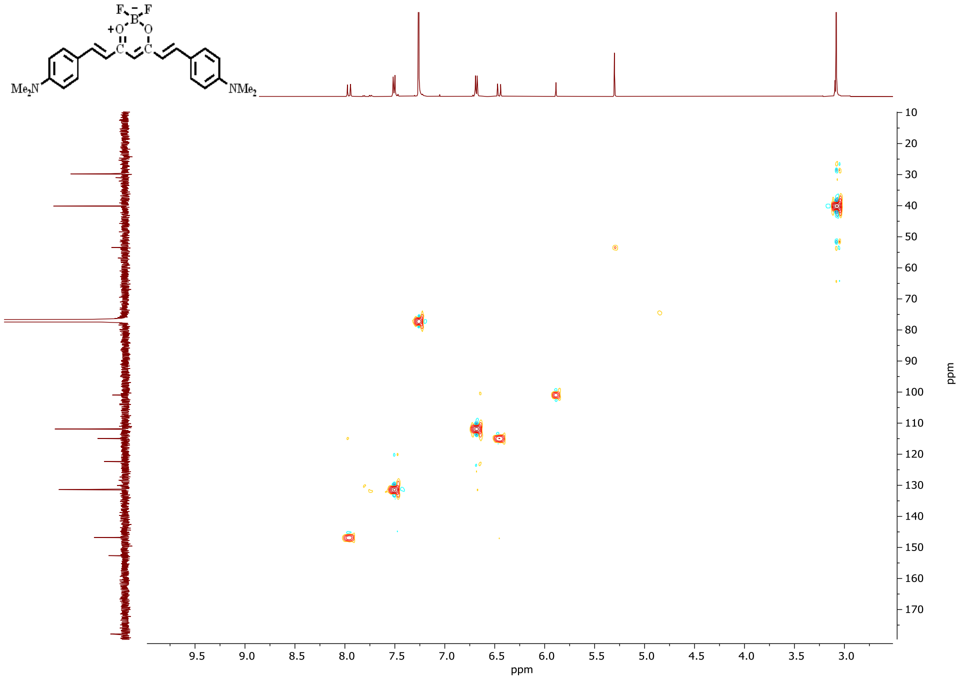

Figure 67: HSQC NMR spectrum of derivative **3c**, in $CDCl_3$.

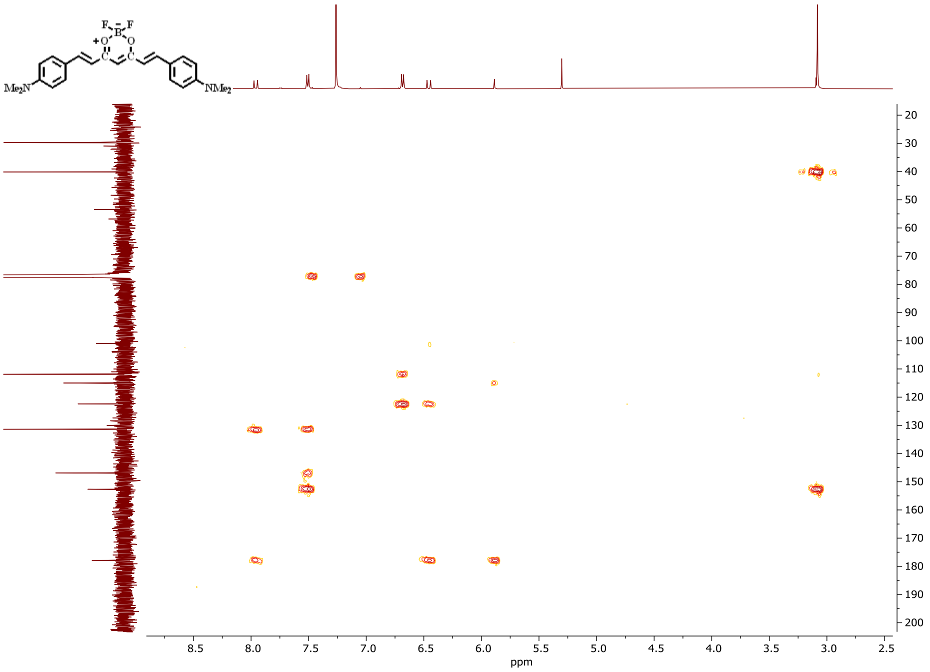

Figure 68: HMBC NMR spectrum of derivative **3c**, in $CDCl_3$.

Derivative 3d

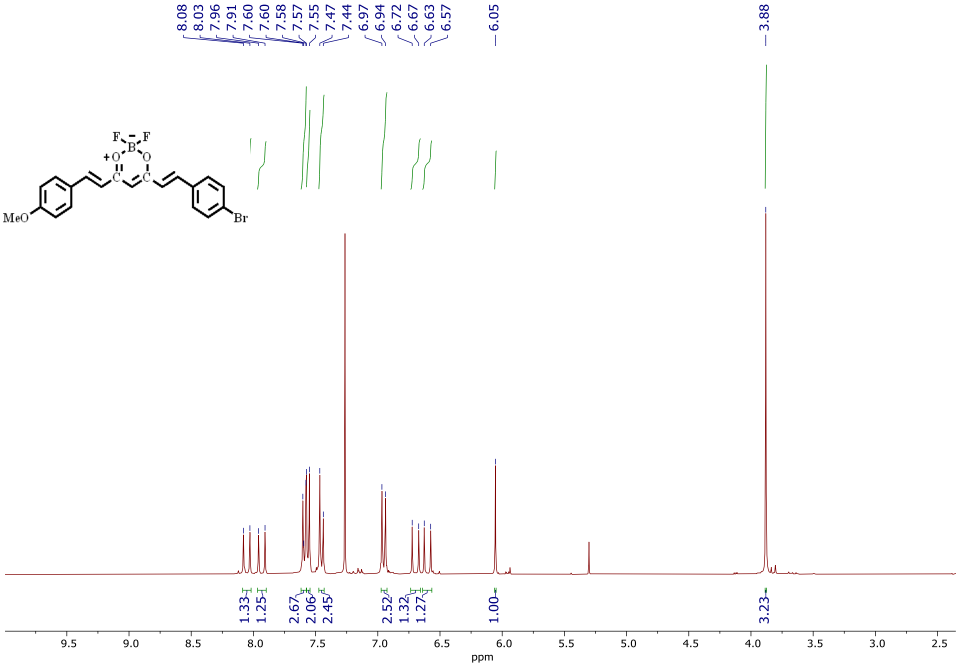

Figure 69: ^{1}H NMR spectrum of derivative **3d**, in $CDCl_3$.

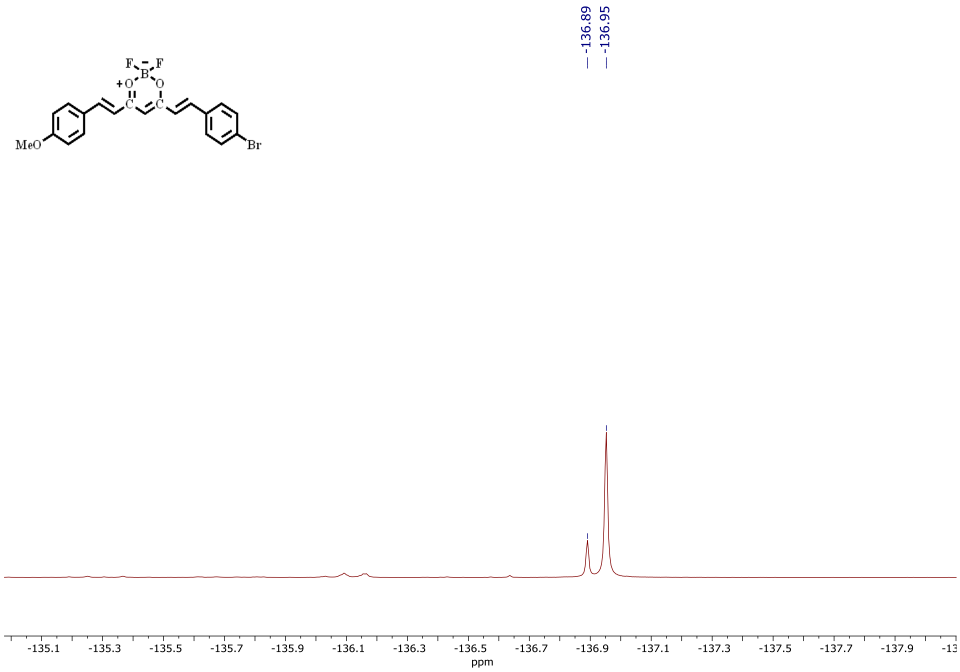

Figure 70: ^{19}F NMR spectrum of derivative **3d**, in $CDCl_3$.

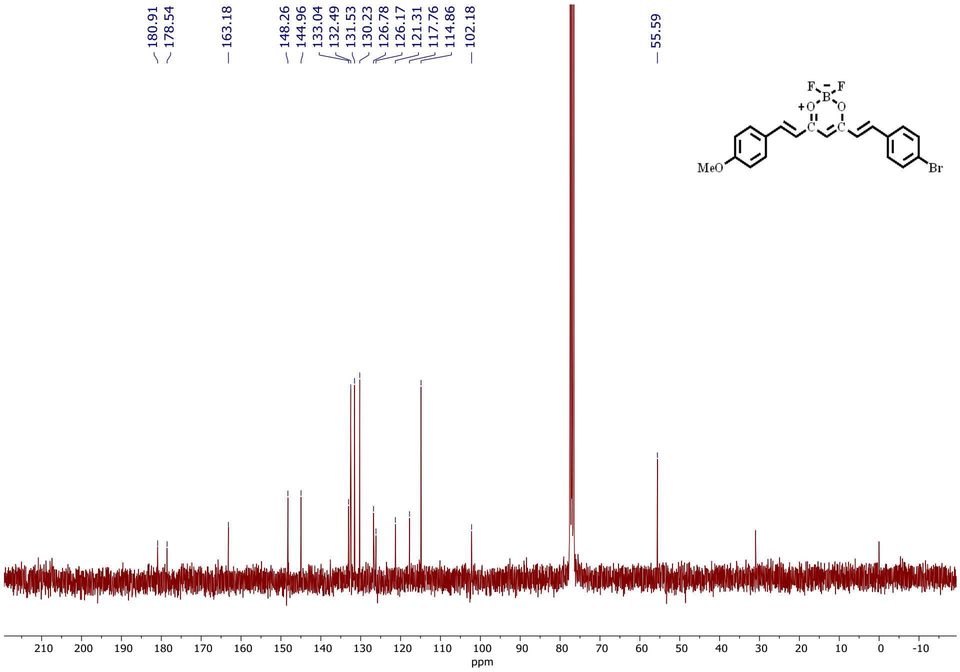

Figure 71: ^{13}C NMR spectrum of derivative **3d**, in $CDCl_3$.

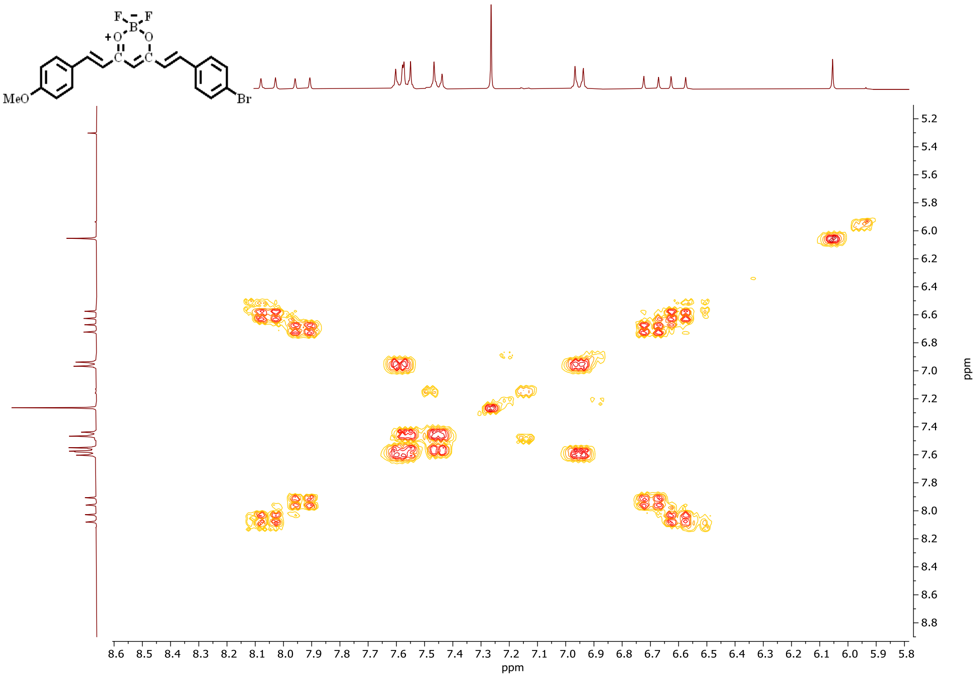

Figure 72: COSY NMR spectrum of derivative **3d**, in CDCl$_3$.

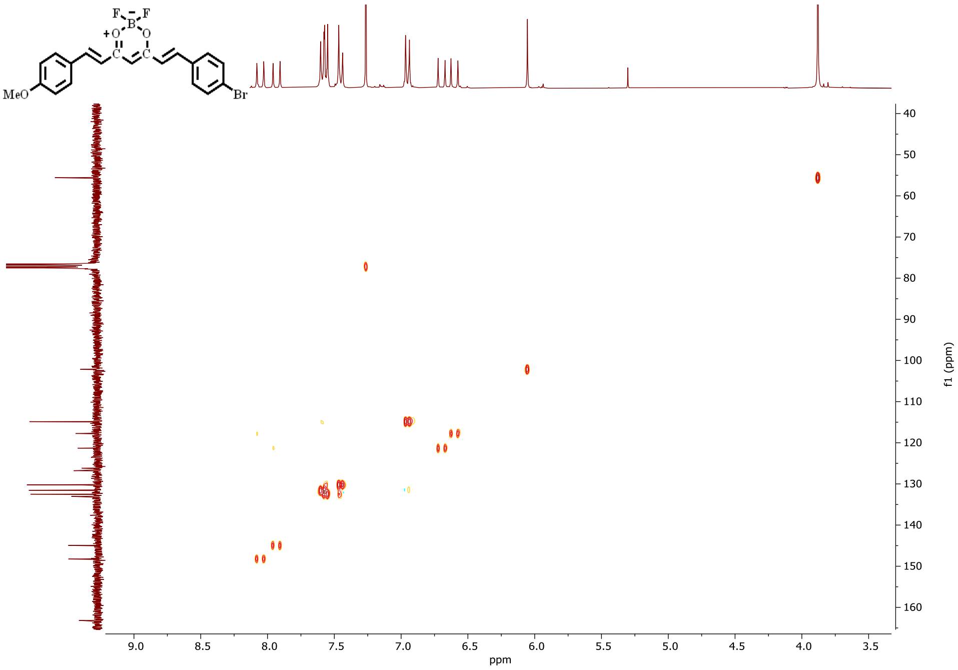

Figure 73: HSQC NMR spectrum of derivative **3d**, in CDCl$_3$.

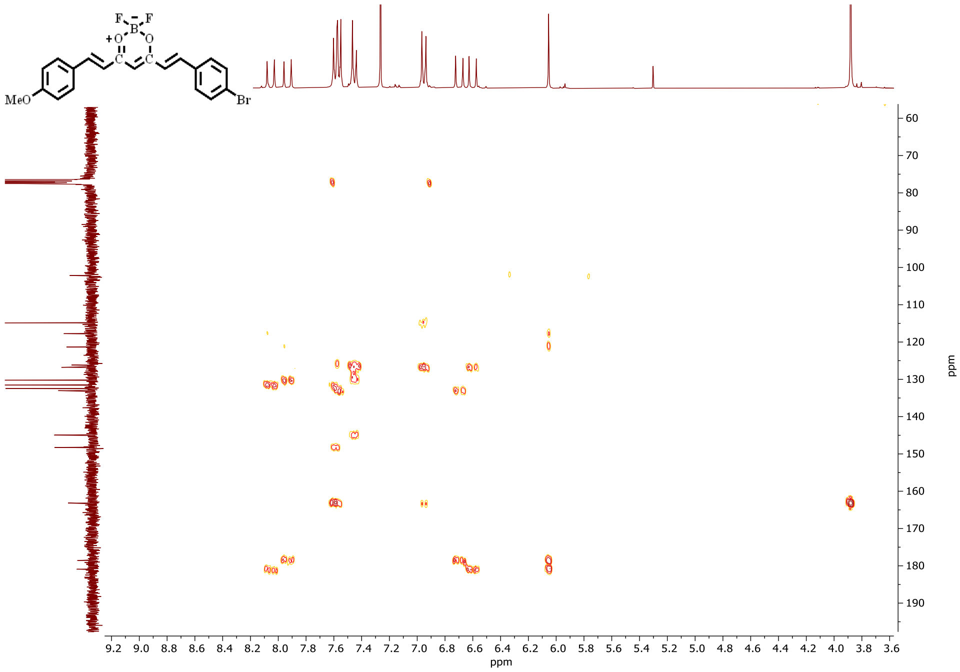

Figure 74: HMBC NMR spectrum of derivative **3d**, in CDCl3.

Derivative 3e

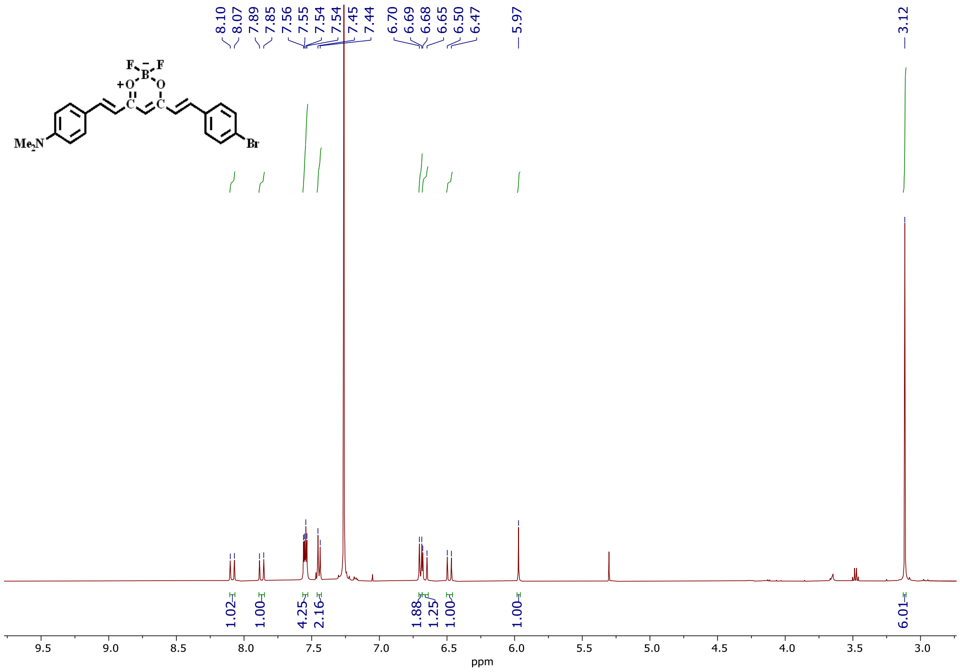

Figure 75: ^{1}H NMR spectrum of derivative **3e**, in CDCl3.

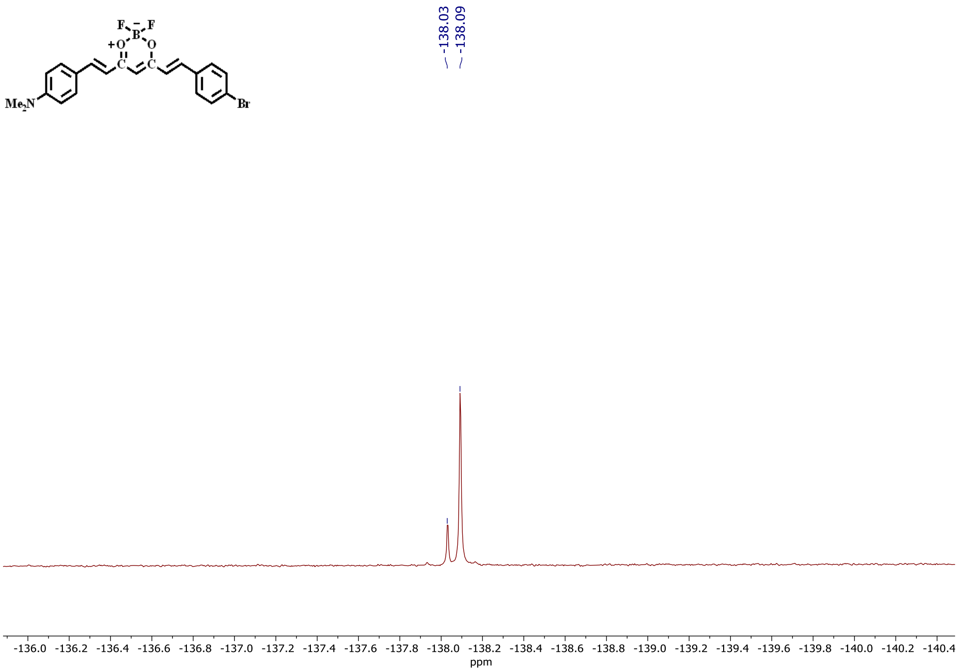

Figure 76: ^{19}F NMR spectrum of derivative **3e**, in $CDCl_3$.

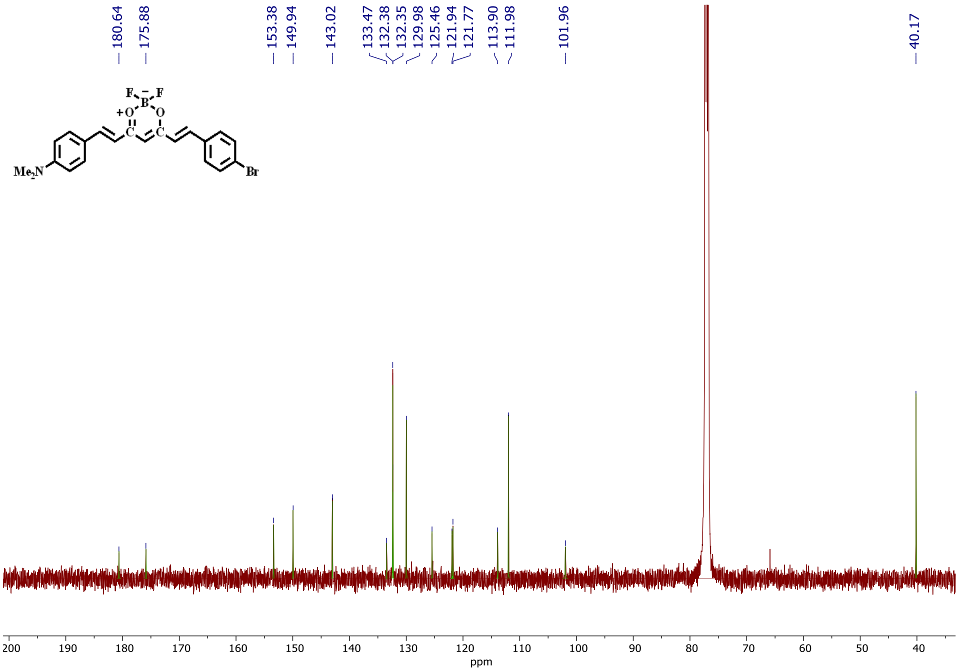

Figure 77: ^{13}C NMR spectrum of derivative **3e**, in $CDCl_3$.

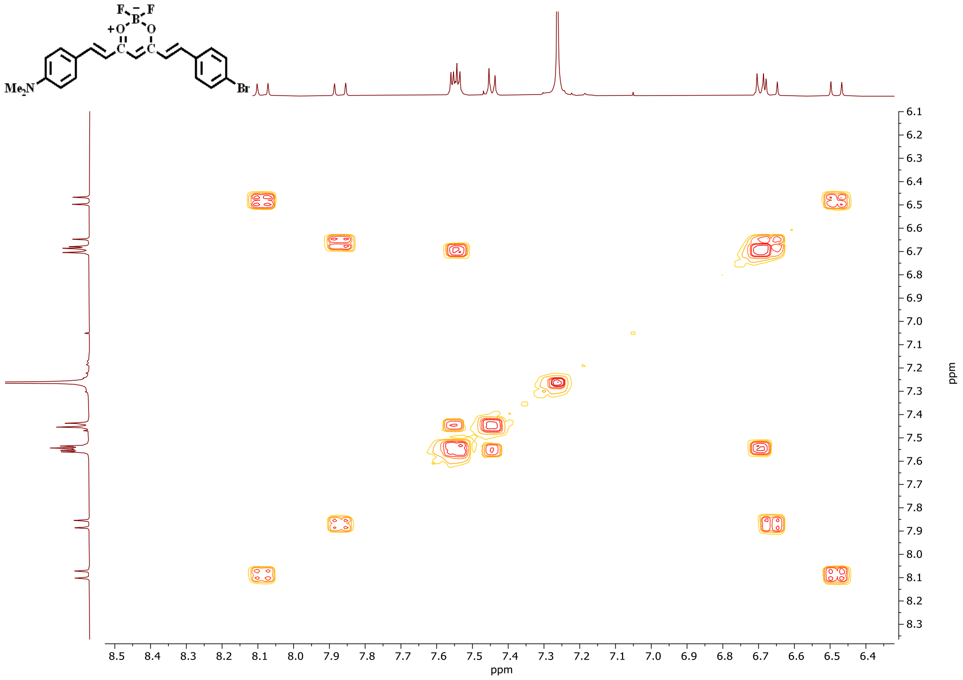

Figure 78: COSY NMR spectrum of derivative **3e**, in CDCl3.

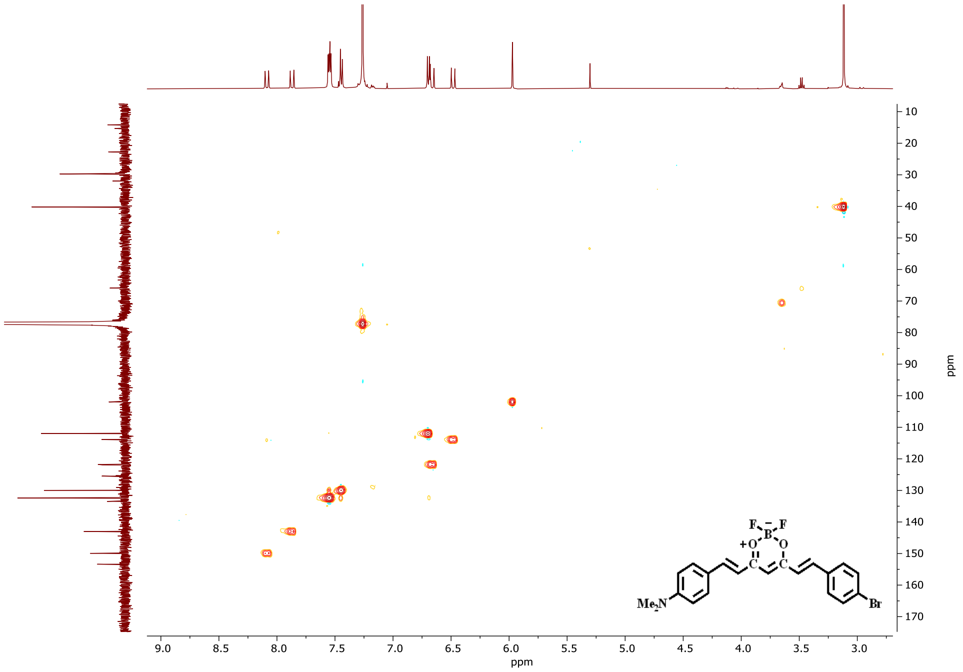

Figure 79: HSQC NMR spectrum of derivative **3e**, in CDCl3.

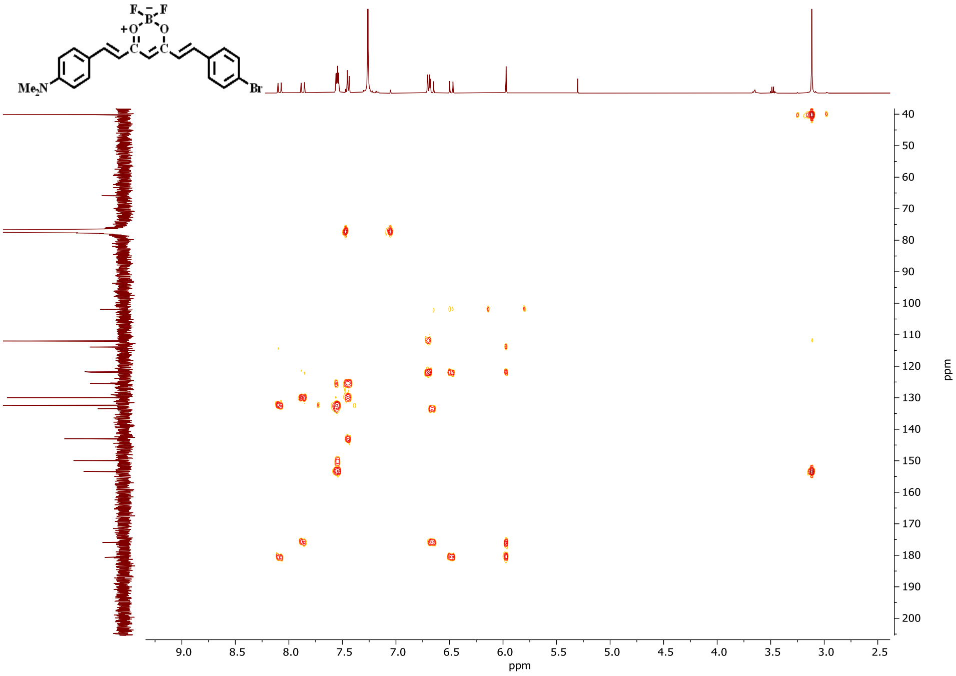

Figure 80: HMBC NMR spectrum of derivative **3e**, in $CDCl_3$.

Derivative 4

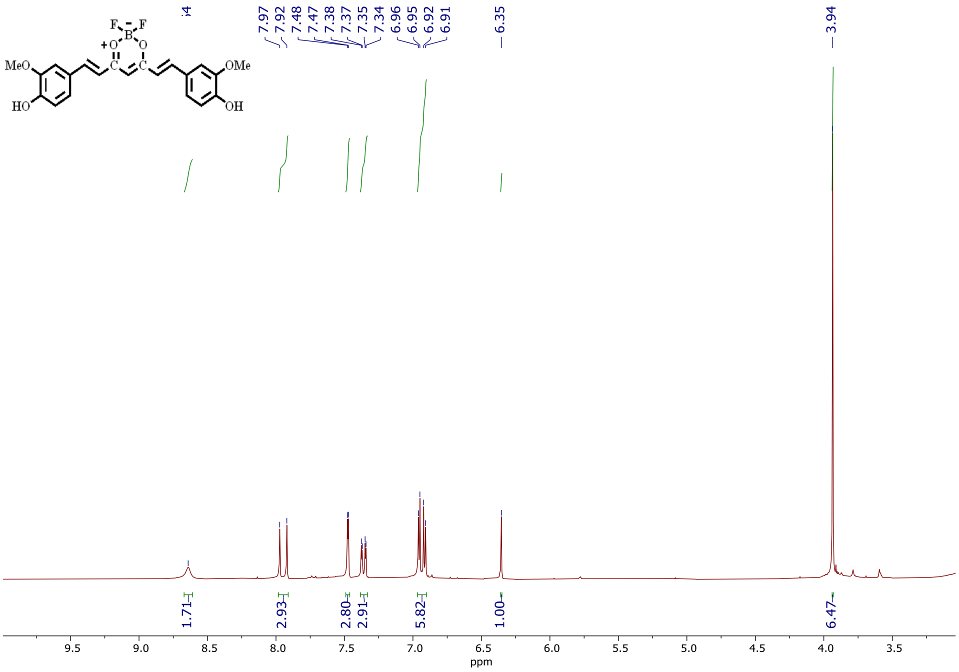

Figure 81: ^1H NMR spectrum of derivative **4**, in $CDCl_3$.

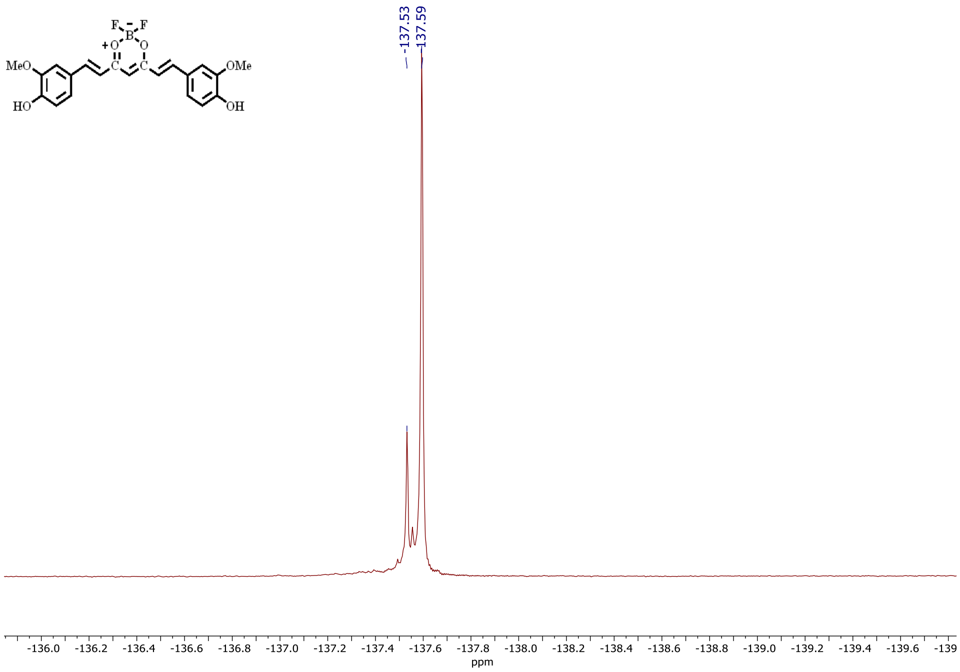

Figure 82: ^{19}F NMR spectrum of derivative **4**, in $CDCl_3$.

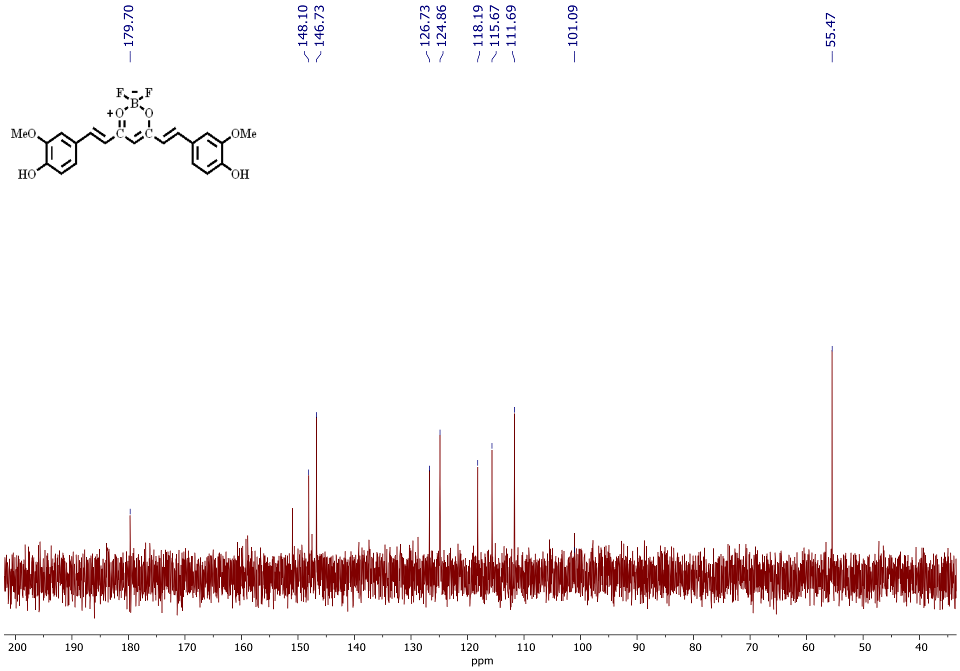

Figure 83: ^{13}C NMR spectrum of derivative **4**, in $CDCl_3$.

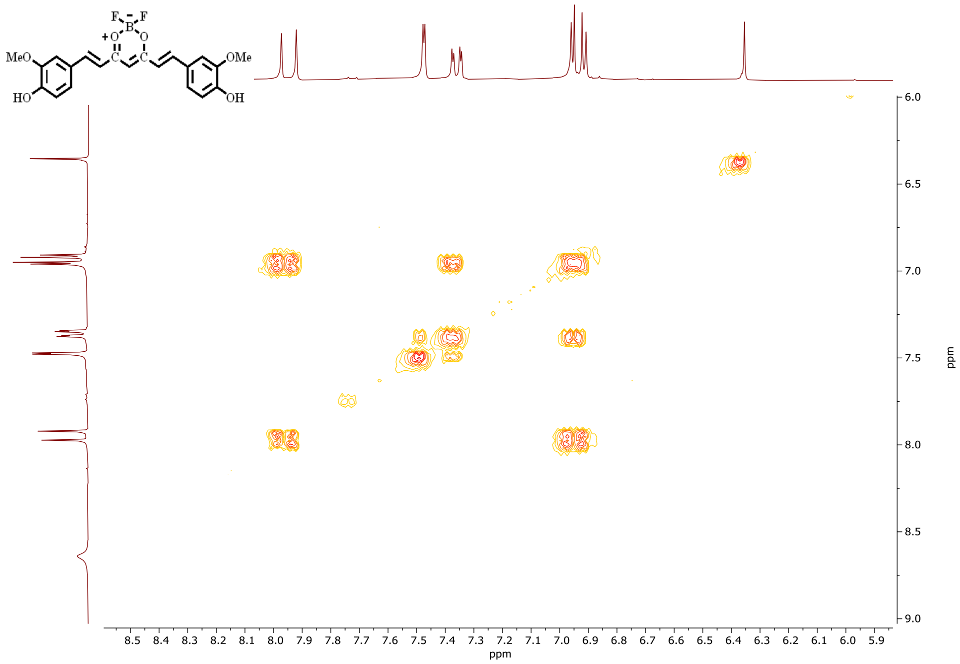

Figure 84: COSY NMR spectrum of derivative **4**, in $CDCl_3$.

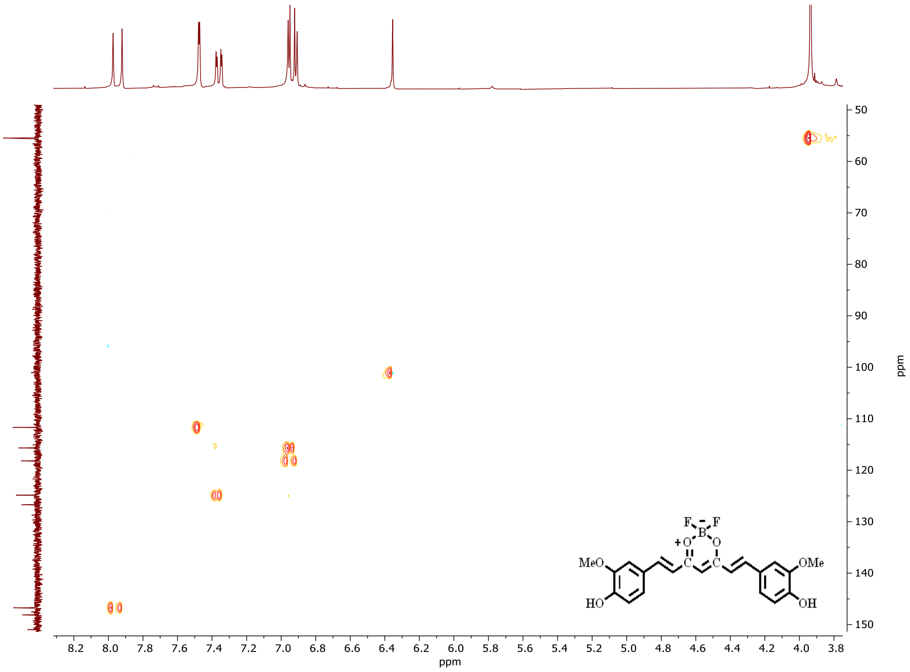

Figure 85: HSQC NMR spectrum of derivative **4**, in $CDCl_3$.

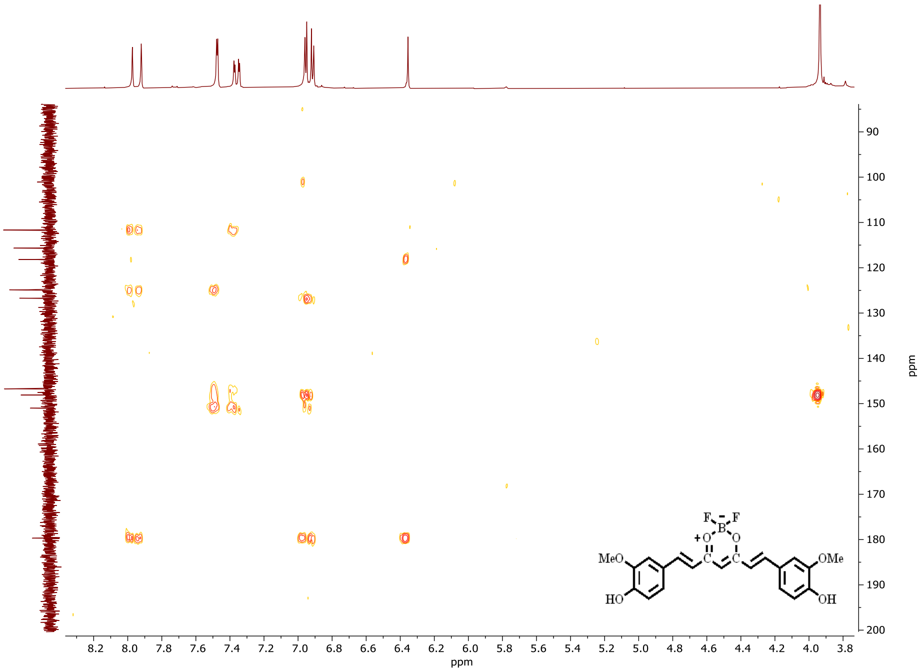

Figure 86: HMBC NMR spectrum of derivative **4**, in $CDCl_3$.

7.2. Attachment B – Absorption, emission, and excitation spectra of 2b, 3a-f, 4 and curcumin at different concentrations

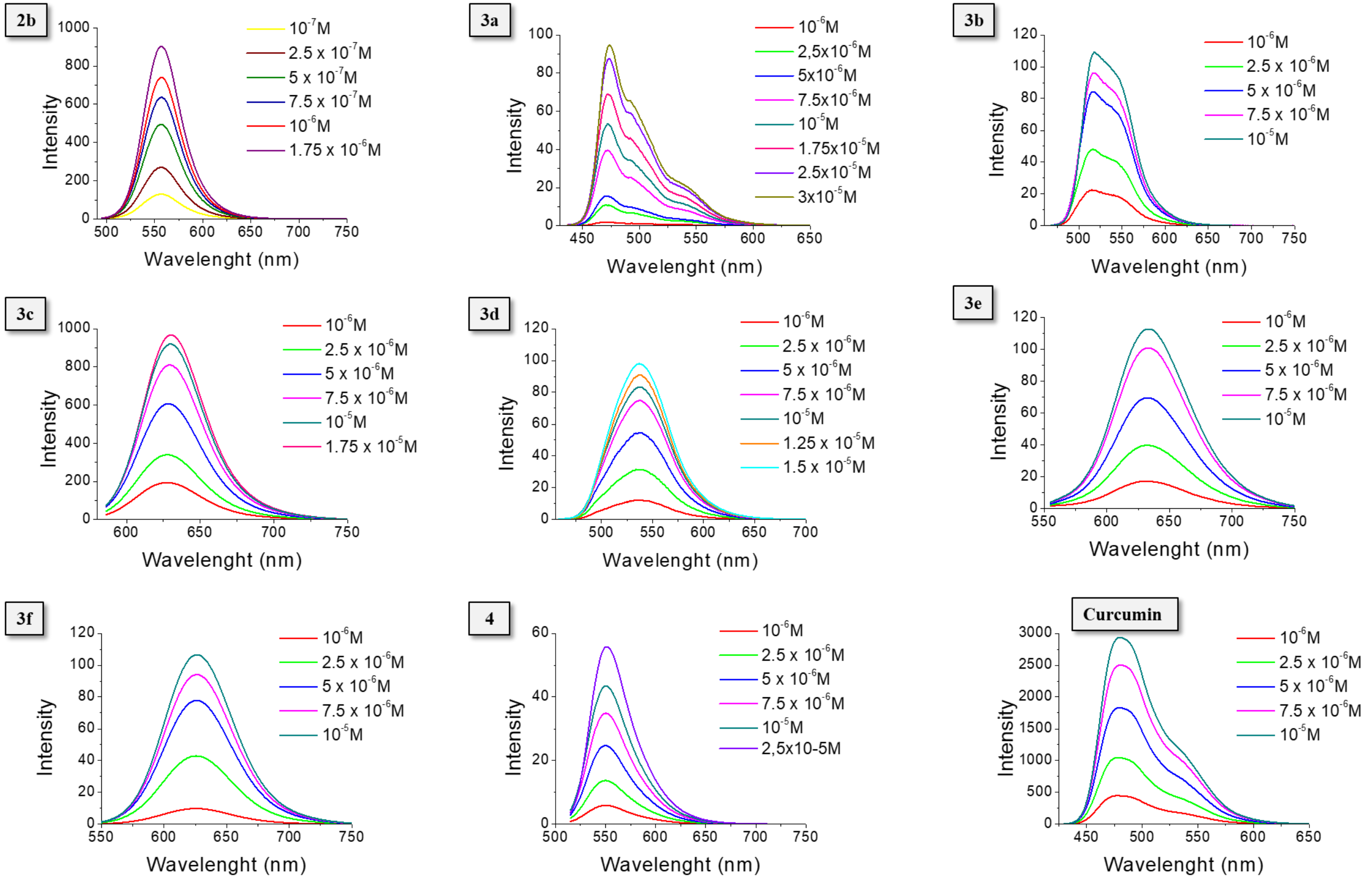

Figure 87: Absorption spectra of compounds **2b**, **3a-f**, **4** and curcumin at different concentrations.

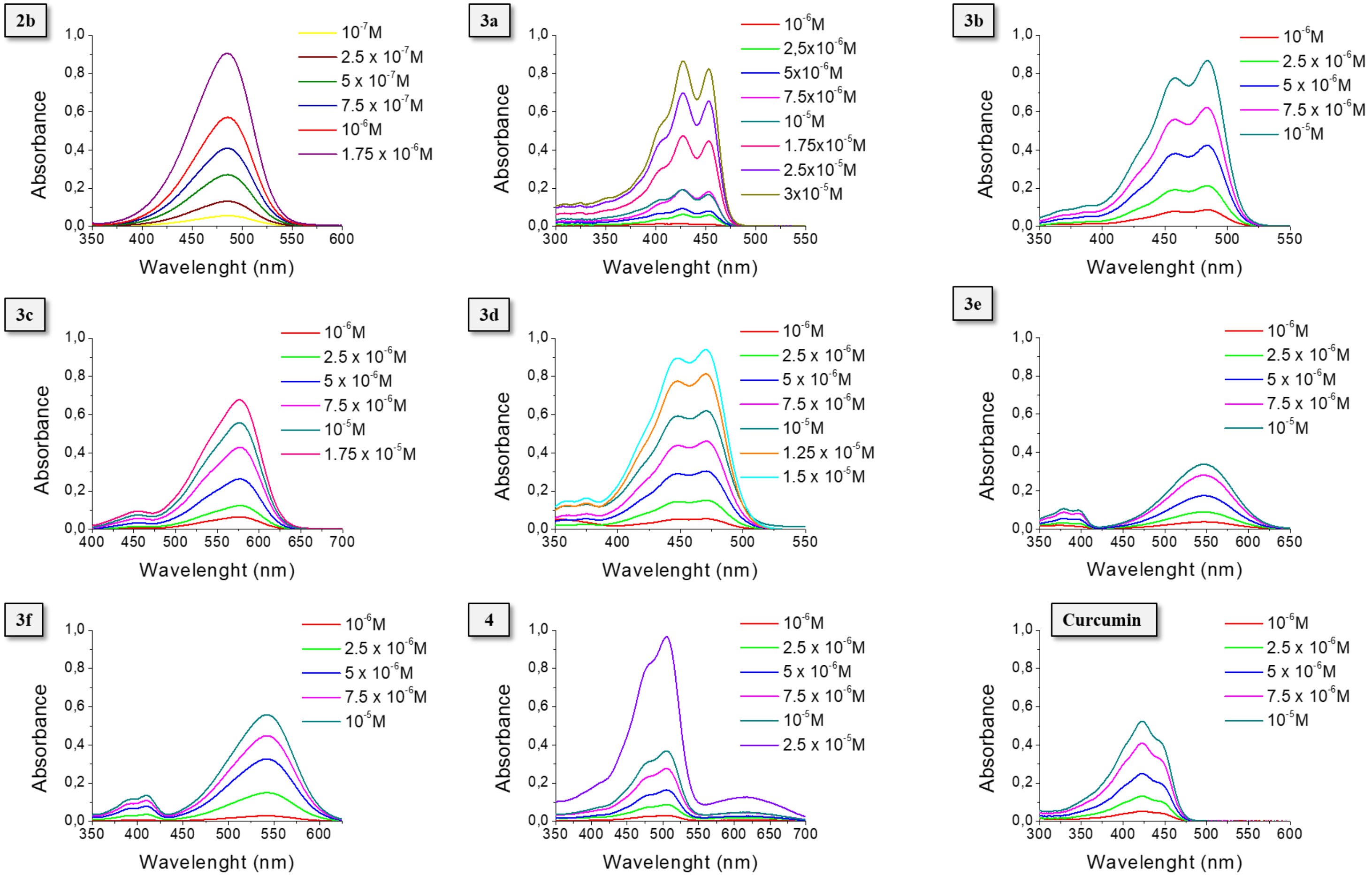

Figure 88: Fluorescence spectra of compounds **2b**, **3a-f**, **4**, and curcumin at different concentrations in THF. Excitation at 485 nm for **2b**, 427 nm for **3a**, 458 nm for **3b**, 576 nm for **3c**, 448 nm for **3d**, 545 nm for **3e**, 540 nm for **3f**, 505 nm for **4** and 420 nm for curcumin.

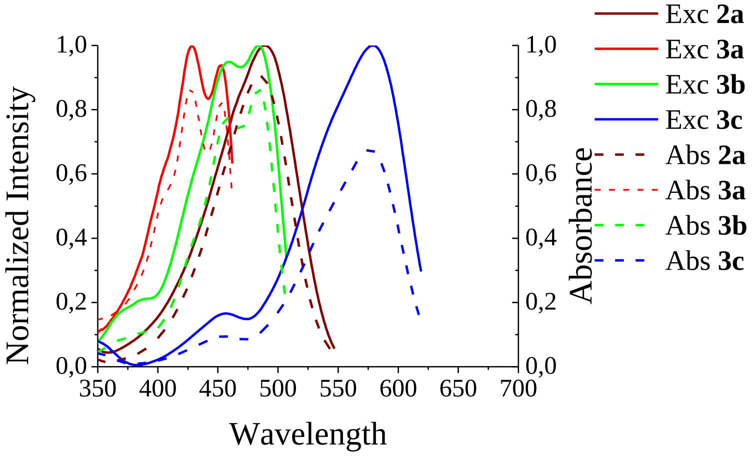

Figure 89: Absorption and excitation spectra of compounds **2b**, **3a-c** in THF.

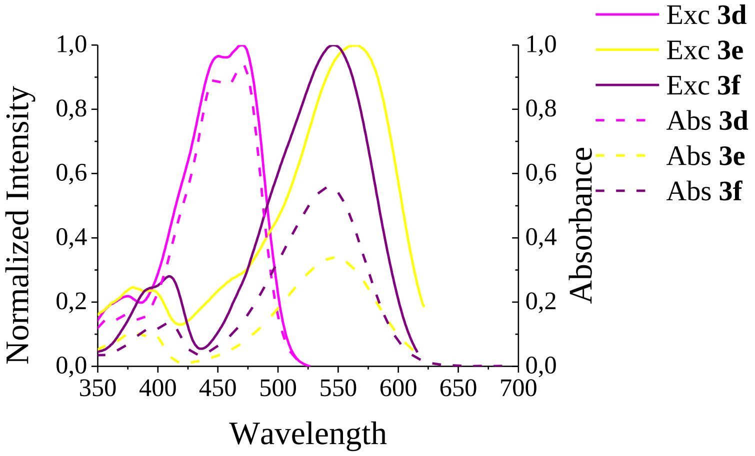

Figure 90: Absorption and excitation spectra of compounds **3d-f** in THF.

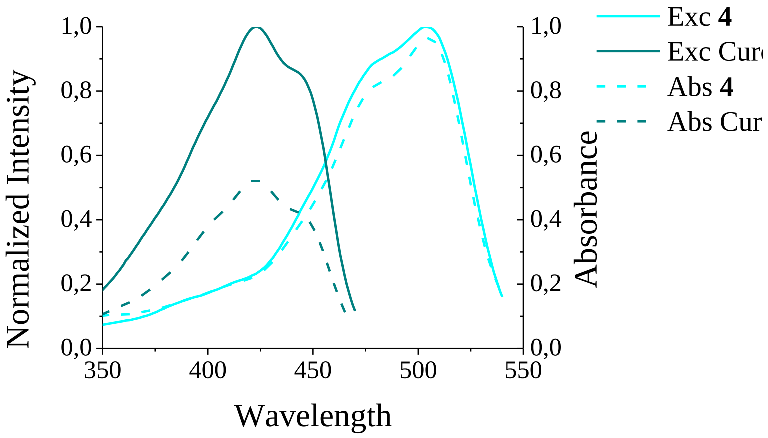

Figure 91: Absorption and excitation spectra of compounds **4** and curcumin in THF.

7.3. Attachment C – Mycelial growth of *Fusarium oxysporum* incubated in PDA with curcumin derivatives 2b, 3a-d, 3f, 4 and curcumin

Control

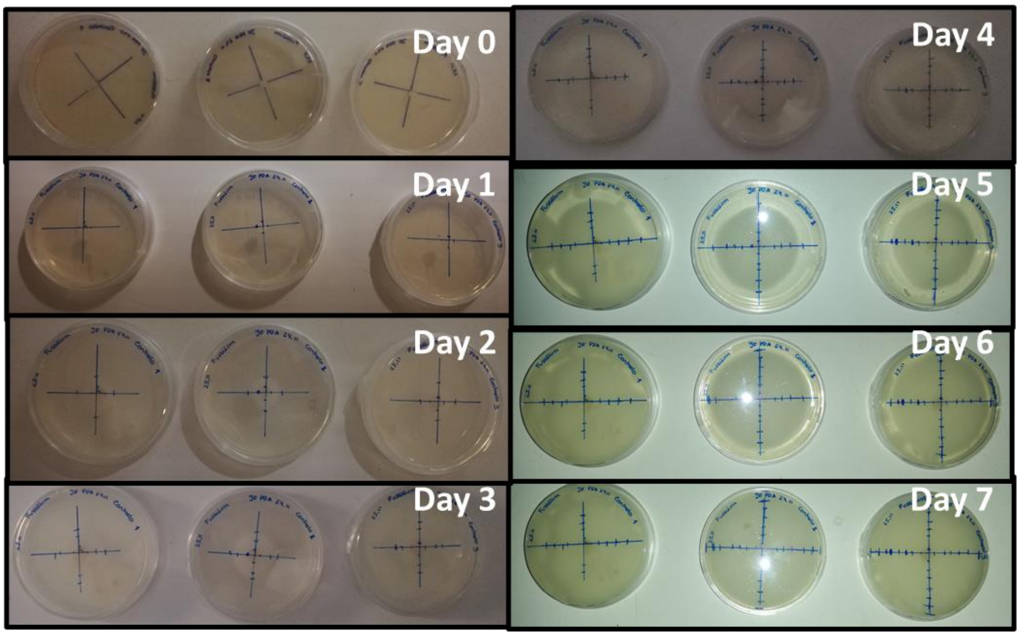

Figure 92: Mycelial growth of *Fusarium oxysporum* incubated in PDA of Control group at 25 ºC for 7 days.

Control+Acetone

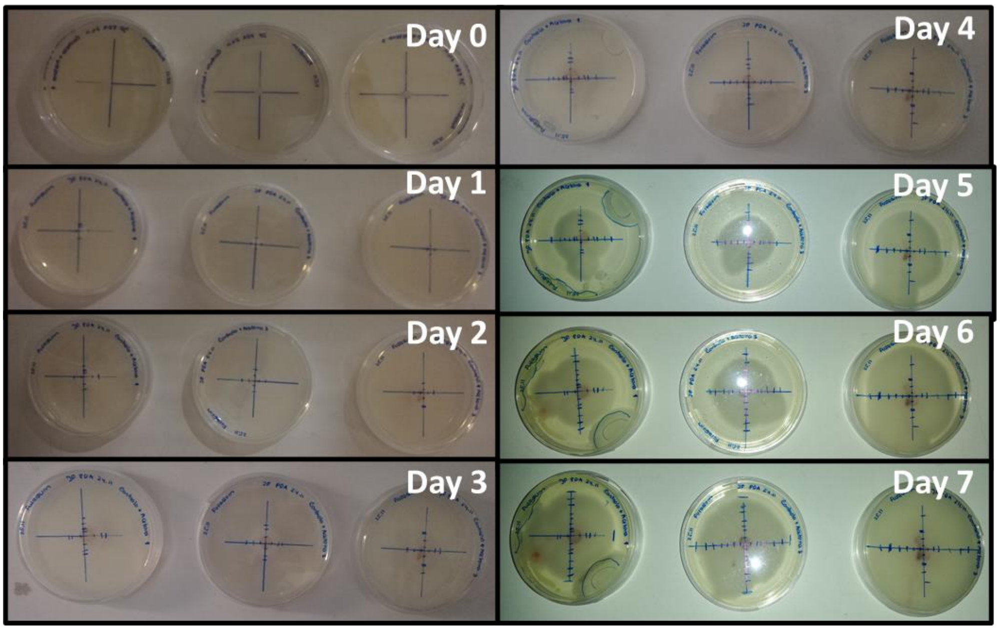

Figure 93: Mycelial growth of *Fusarium oxysporum* incubated in PDA of Control+Acetone group at 25 ºC for 7 days.

Derivative 2b

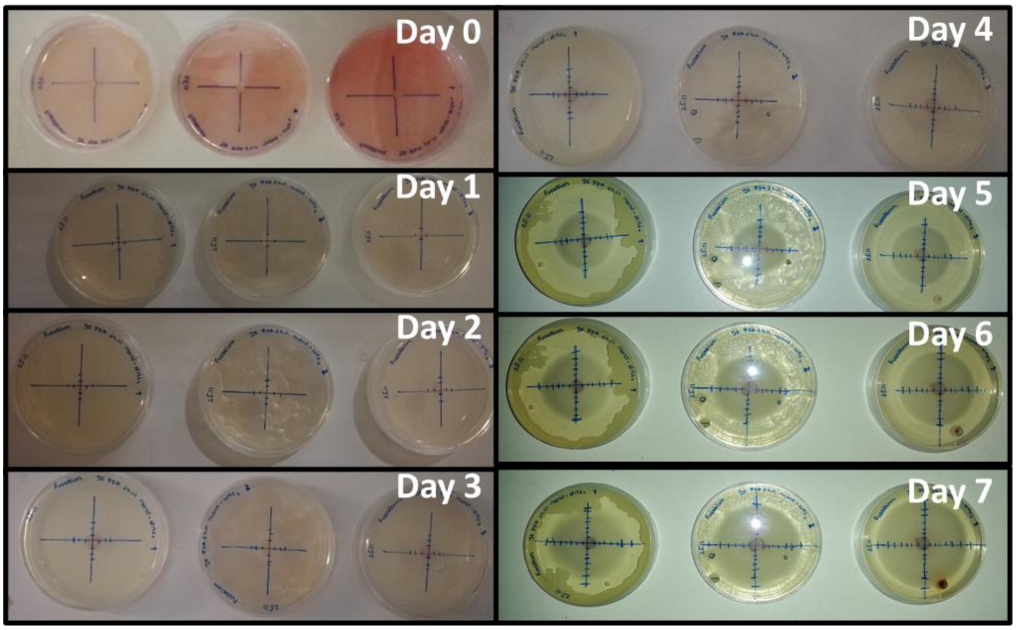

Figure 94: Mycelial growth of *Fusarium oxysporum* incubated in PDA with curcumin derivative **2b** at 25 ºC for 7 days.

Derivative 3a

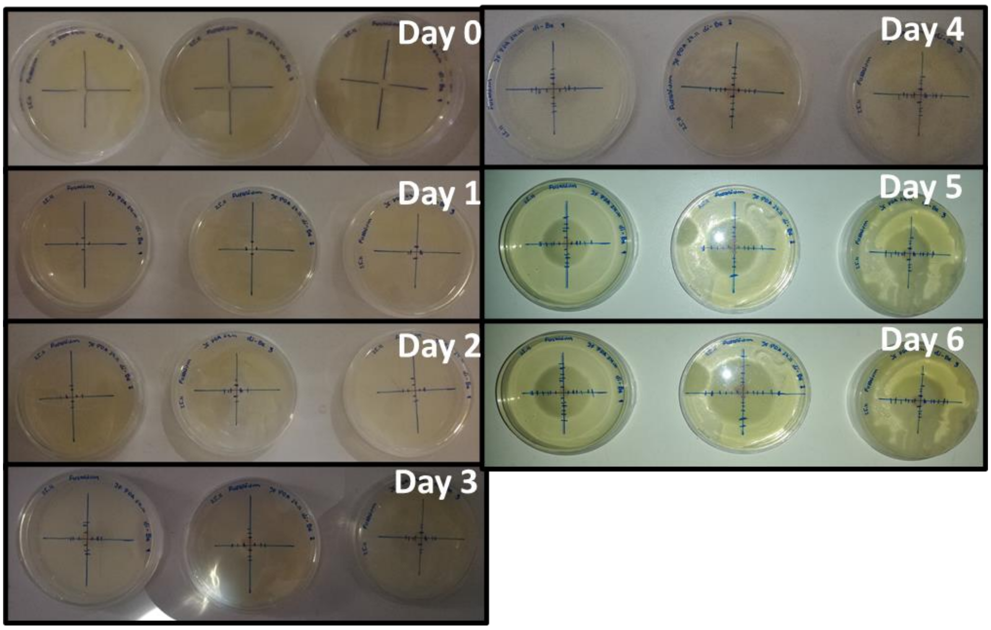

Figure 95: Mycelial growth of *Fusarium oxysporum* incubated in PDA with curcumin derivative **3a** at 25 ºC for 7 days.

Derivative 3b

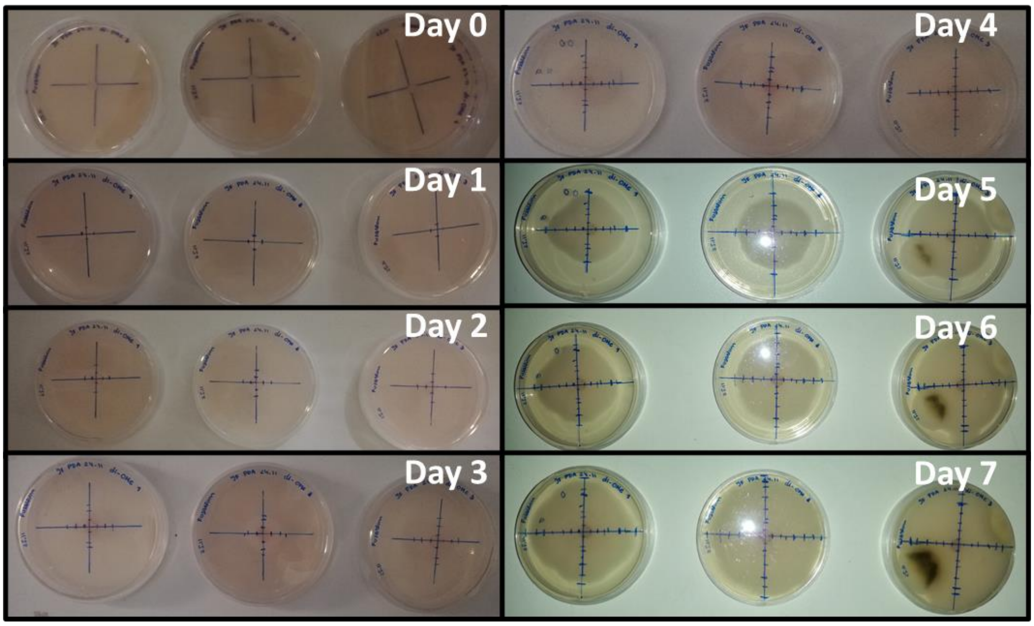

Figure 96: Mycelial growth of *Fusarium oxysporum* incubated in PDA with curcumin derivative **3b** at 25 ºC for 7 days.

Derivative 3c

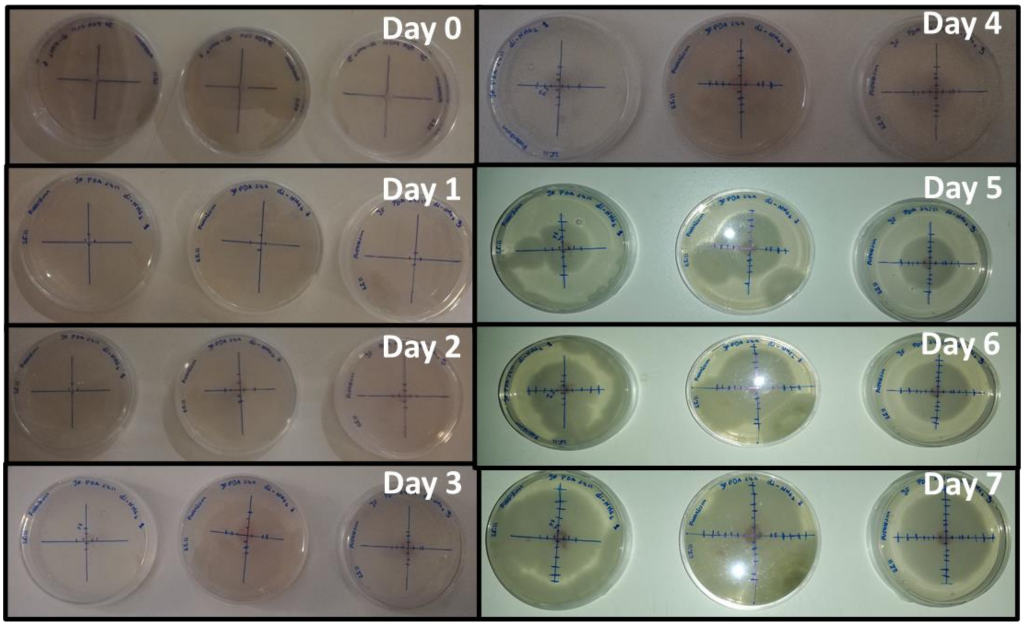

Figure 97: Mycelial growth of *Fusarium oxysporum* incubated in PDA with curcumin derivative **3c** at 25 ºC for 7 days.

Derivative 3d

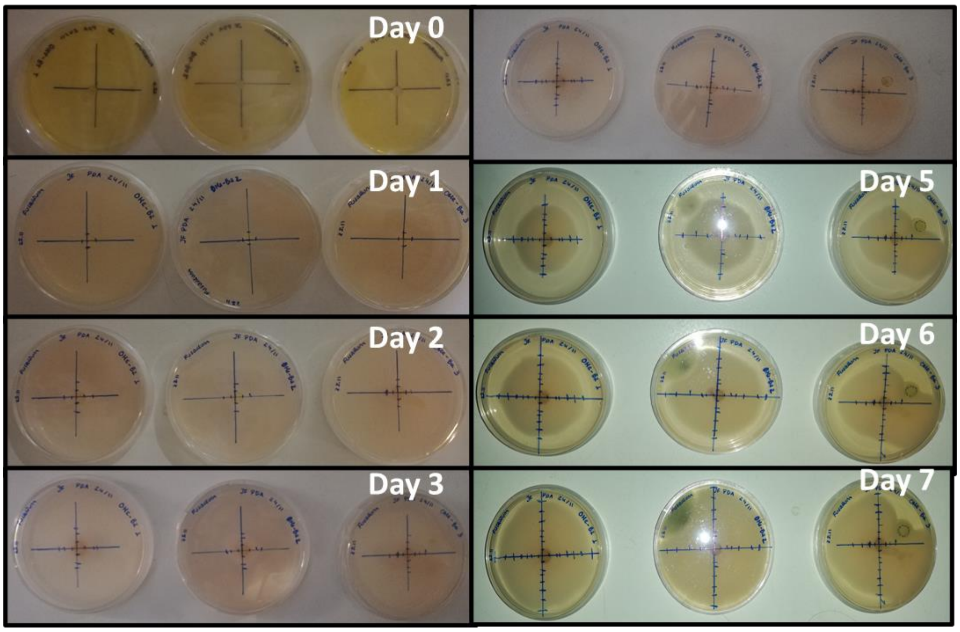

Figure 98: Mycelial growth of *Fusarium oxysporum* incubated in PDA with curcumin derivative **3d** at 25 ºC for 7 days.

Derivative 3f

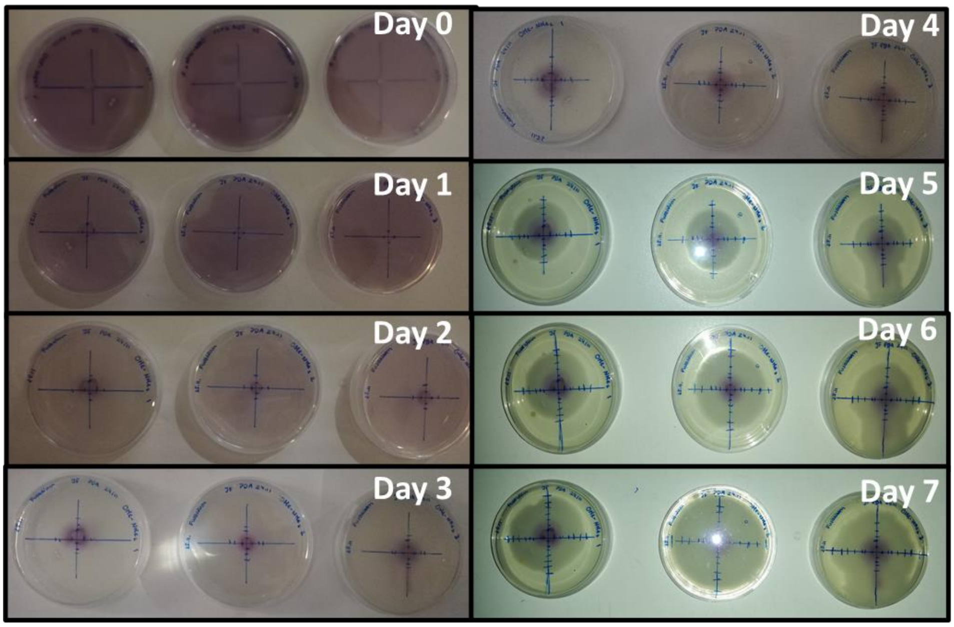

Figure 99: Mycelial growth of *Fusarium oxysporum* incubated in PDA with curcumin derivative **3f** at 25 ºC for 7 days.

Derivative 4

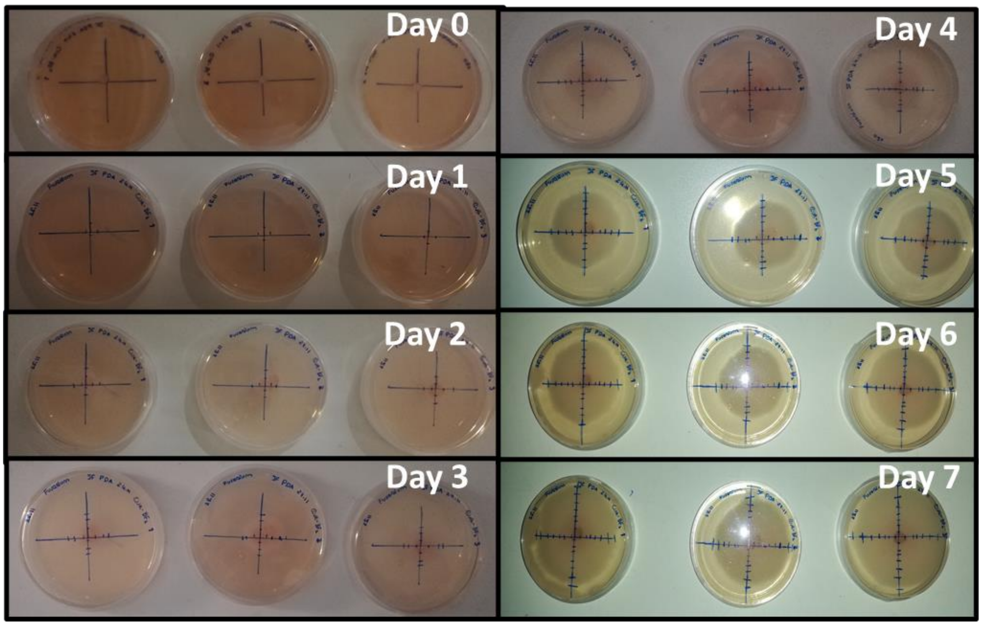

Figure 100: Mycelial growth of *Fusarium oxusporum* incubated in PDA with curcumin derivative **4** at 25 ºC for 7 days.

Curcumin

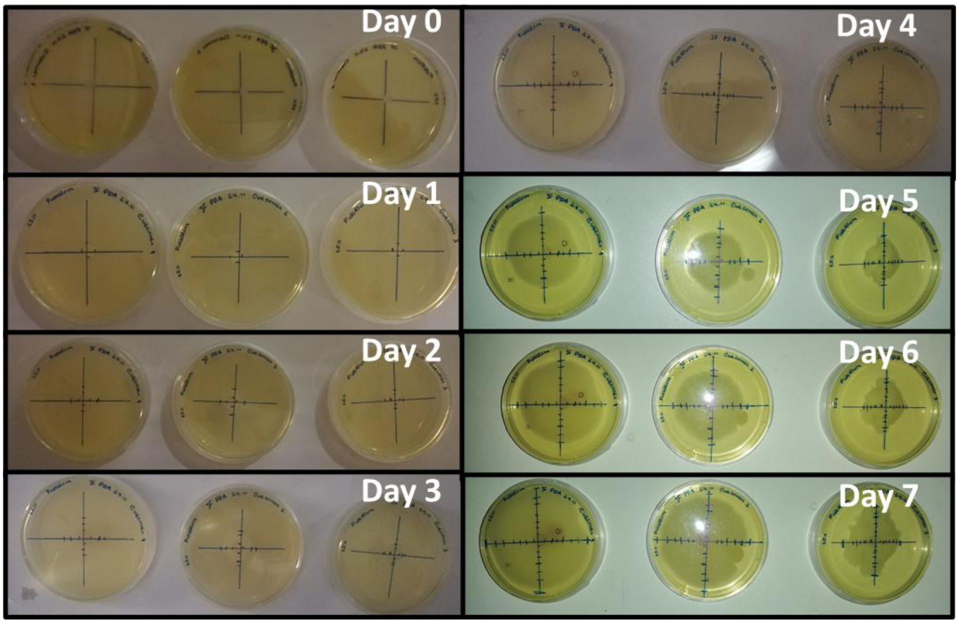

Figure 101: Mycelial growth of *Fusarium oxysporum* incubated in PDA with curcumin at 25 ºC for 7 days.